VIBRATION AND STABILITY OF HIGH-SPEED SPINNING CANTILEVERED BEAMS WITH SHEAR DEFORMATION EFFECTS AND AN ATTACHED RIGID BODY AT ITS TIP
and
NONLINEAR HYPERELASTIC BEHAVIOR OF CIRCULAR DIELECTRIC ELASTOMER MEMBRANES

by

SAM FALLAHPASAND

A dissertation submitted in partial fulfillment of the
requirements for the degree of

DOCTOR OF PHILOSOPHY IN MECHANICAL ENGINEERING

2025

Oakland University
Rochester, Michigan

Doctoral Advisory Committee:

Christopher G. Cooley, Ph.D., Chair
Zissimos P. Mourelatos, Ph.D.
Ryan J. Monroe, Ph.D.
Meir Shillor, Ph.D.

ACKNOWLEDGMENTS

I would like to express my sincere gratitude to my advisor, Prof. Christopher G. Cooley, for his insightful guidance and valuable feedback throughout my PhD studies. I also appreciate constructive comments and suggestions from my committee members, Prof. Zissimos P. Mourelatos, Prof. Meir Shillor, and Prof. Ryan J. Monroe. Finally, I am deeply grateful to my family for their support and encouragement,

SAM FALLAHPASAND

ABSTRACT

VIBRATION AND STABILITY OF HIGH-SPEED SPINNING CANTILEVERED BEAMS WITH SHEAR DEFORMATION EFFECTS AND AN ATTACHED RIGID BODY AT ITS TIP
and
NONLINEAR HYPERELASTIC BEHAVIOR OF CIRCULAR DIELECTRIC ELASTOMER MEMBRANES

by

SAM FALLAHPASAND

Adviser: Christopher G. Cooley, Ph.D.

Instability of components and systems causes large-amplitude deformations or vibrations that limit performance, increase fatigue, and cause overload failures. In spinning systems, gyroscopic effects drive instabilities at high speeds. Instability in soft actuators occurs due to nonlinear material behavior. This work examines the dynamic stability of spinning structures with shear deformation effects and static instability in dielectric elastomer actuators. The vibration behavior, critical speeds, and high-speed instabilities in thick beams, spinning about their longitudinal axis, that have a rigid body attached to their tip are analyzed analytically and using finite element models. The analytical beam model includes shear deformation effects, incorporated by assuming the beam's transverse displacements are independent of its cross-sectional rotations. A model is derived using Hamilton's principle. The equations are cast into extended operator form, which exemplifies the system's gyroscopic structure and facilitates Galerkin discretization for numerical solution. Numerical results are calculated for a system with identical inertia and stiffness properties in the two bending directions (called a symmetric system) and non-identical inertia and stiffness properties in the two bending directions (called an asymmetric system).

Both systems have forward- and backward-orbit vibrations in single-mode, free response. Symmetric systems have material points that move in circular orbits along the span. The material point orbits become elliptical for asymmetric systems. Symmetric systems have degenerate stationary-system natural frequencies that split and become distinct for non-zero speeds. All eigenvalues cross, without interaction, as the rotation speed varies. The symmetric system eigenvalues are purely imaginary except at high speeds where critical speeds occur. Asymmetric systems, due to the differing inertia and stiffness properties in the two bending directions, have distinct stationary-system eigenvalues that increase and decrease with increasing speed from vanishing speed. Because of shear deformation effects, eigenvalue veering occurs when any decreasing forward-orbit eigenvalue comes into close proximity with an increasing backward-orbit eigenvalue. Within veering regions the forward- and backward-orbit modes couple, creating a single-mode free response that has forward-orbit vibrations in some regions along the span and backward-orbit vibrations in others. Asymmetric beams have distinct critical speeds and regions of divergence instability. Shear deformation effects lead to flutter instability at high speeds. Parametric studies reveal atypical high-speed instability behavior, including immediate transitions from divergence to flutter instability as speed varies. The mathematical structure observed for symmetric beam-rigid body systems is leveraged for closed-form solutions for their vibration. Finite element analyses are used to confirm the speed-dependent natural frequencies and identify axially- and torsionally-dominated modes. The results from this work could improve the high-speed performance of resonator devices like MEMS gyroscopes.

The equilibria and stability of voltage-activated, pre-stretched circular dielectric elastomer membrane actuators under equilibrium conditions are studied using nonlinear analytical and coupled electro-mechanical finite elements simulations. The analytical model includes only the active region of the actuator; the passive region is replaced by a uniform

outer circumferential load intended to capture the membrane's initial pre-stretch. The model is derived in terms of a general strain energy density so that the voltage-stretch behavior of common hyperelastic material models can be examined. The Gent hyperelastic model is used as a baseline because of its ability to accurately predict the large-stretch mechanical behavior of a common acrylic elastomer used in dielectric elastomer transducers. The Gent model predicts one equilibrium at low voltages, three equilibria at moderate voltages, and one equilibrium at high voltages. The membrane experiences snap-through and snap-back bifurcations between small- and large-stretch equilibria. Moderate stretch models can capture the loss of stability, but snap-through to large-stretches are not possible. Hyperelastic models that include strain stiffening can capture large-stretch deformations, provided sufficient numbers of terms and material parameters are used. The finite element model includes both active and passive regions of the membrane actuator, inhomogeneity of deformations, the potential for material compressibility, and electric fringe fields at the boundaries of the electrodes. When the passive region is neglected, the finite element model predicts similar voltage-stretch behavior as the analytical model. When the passive region is included, the stretch meaningfully decreases, highlighting the potential importance of the passive region in actuators. Whereas the finite element model shows nearly homogeneous deformations within the active region, the deformations in the passive region are highly inhomogeneous. The finite element model is compared to available experiments.

TABLE OF CONTENTS

TABLE OF CONTENTS - Continued

LIST OF TABLES

LIST OF FIGURES

CHAPTER ONE

INTRODUCTION

1.1 Spinning beam

1.1.1 Motivation

High-speed rotating systems are the primary means of power transmission in machines and industries, including vehicles, turbines, centrifugal compressors, aerospace technologies, etc. A wide range of these devices are utilized in highly advanced, precise technologies. Figure 1.1 shows some notable examples of their applications.

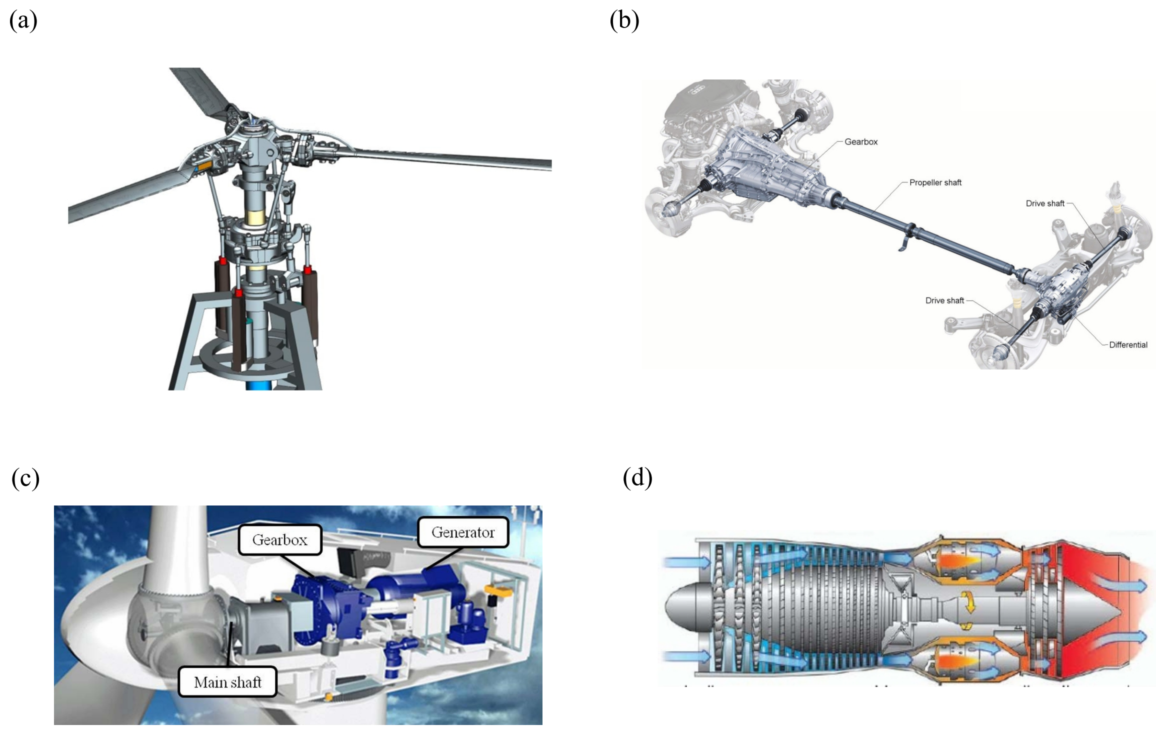

Figure 1.1: Notable examples of the applications of spinning systems. (a) Helicopter main rotor mast [1], (b) drivetrain propeller shaft (image downloaded from x-engineer.org on 01/30/2025), (c) wind turbine shaft [2], (d) jet engine rotor [3]

Operating under high-speed rotations, any uncontrolled vibrations or instabilities can cause catastrophic failures or seriously impair their functioning. High-speed spinning systems also serve as gyroscopic resonators, which integrate the gyroscopic effects and vibrations to fulfill various purposes, such as sensing, stabilization, and energy harvesting. A schematic of a vibratory micro-gyroscope resonator consisting of a cantilever beam with a tip mass. Studying vibrations in spinning systems and their dynamic behaviors helps not only control unwanted vibrations but also streamline their performance. Sophisticated designs for the products, which use the fundamentals developed through these studies, can improve their output efficiency and optimize the costs to a considerable extent.

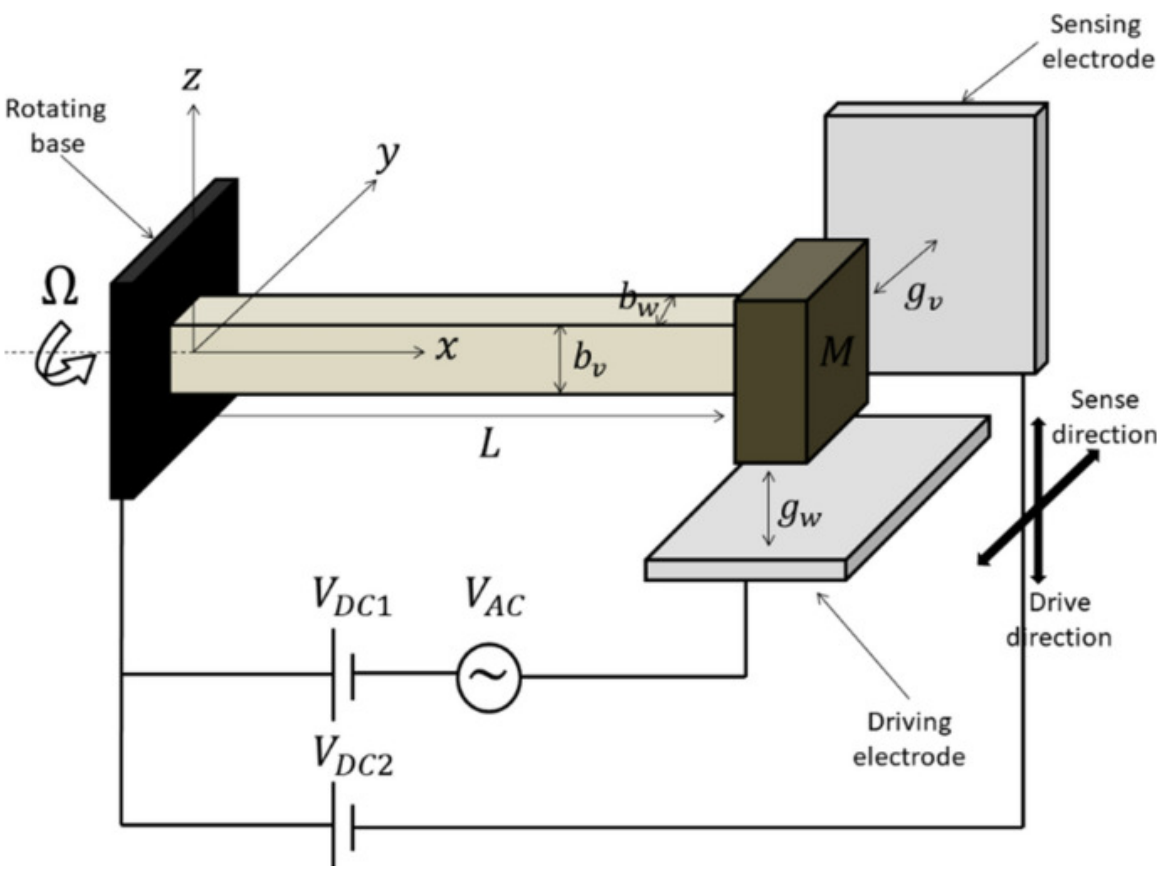

Figure 1.2: Schematic of a vibratory micro-gyroscope resonator consisting of a cantilever beam with a tip mass [4]

1.1.2 Literature review

Vibrations in spinning shafts rotating at a constant speed about its longitudinal axis were initially studied by some authors [5–8]. They showed that increasing the spinning speed causes the natural frequencies to be divided into two branches with forward and backward orbit modes. With increasing the rotation speed, the natural frequencies increase (decrease) for the backward (forward) modes. Bauer [5] obtained the analytical close-form solutions for the free and harmonically forced oscillations of a spinning uniform beam under common boundary conditions. Euler-Bernoulli beam theory was used in this study, assuming the beam to be slender so that the rotatory inertia and shear deformations are negligible. Gyroscopic effects and rotatory inertia are modeled in a wide range of studies using Rayleigh beam theory [9–12].

The ratio of shear strains to bending strains is higher for thicker cross-sectional areas, reducing the accuracy of the solutions derived by the Euler-Bernoulli and Rayleigh Beam theories. To include shear deformations in the dynamic modeling, a wide range of studies have been conducted based on the Timoshenko beam theory [13–18]. Han and Zu [14] solved the governing equations of Timoshenko beam analytically for six classical boundary conditions by modeling 2-dimensional oscillations with complex-valued solutions.

Rigid bodies are an indispensable part of many rotating systems, whose Mass Moments of Inertia (MOIs) can substantially impact the dynamic behavior of the whole system. The effects of rigid bodies on the transverse vibrations of non-rotating beams have been studied in numerous research works. Laura et al. [19] presented a closed-form solution for the natural frequencies and mode shapes of a stationary clamped-free beam with a lumped mass attached to its end using the Euler-Bernoulli beam theory. Rossi et al [20] took the effects of the Mass Moments of Inertia (MOIs) of the rigid body into account in its modeling. Followed by other studies [21, 22] similar problems with spring-mass connections in their boundary conditions are investigated. The effects of larger tip mass were investigated in Refs. [23, 24]. Transverse vibrations of the free-free Timoshenko beam with equal and unequal rigid bodies attached at both endpoints are studied for equal tip mass [25] and unequal tip masses [26]. Wu [27] extended their studies to the free-free Timoshenko beam carrying multiple rigid bodies. Bhat and Wagner [28] studied the effects of eccentric mounting of the mass on the vibrations of a uniform cantilever beam.

Subsequent research explored the impacts of rigid bodies on rotating systems, including rotors and spinning beams. Eshleman and Eubanks [29] analytically investigated the first four forward and backward orbit modes of a shaft carrying a rigid disk over the spinning speed, in which the effects of transverse shear were included in the modeling. A range of analytical and numerical studies [30, 31] were carried out on free vibrations in spinning Timoshenko shafts carrying several concentrated masses or rigid disks. Some studies also investigated the effects of multiple concentrated masses and their positions on the vibration characteristics of a Timoshenko beam [30, 31]. Further studies have also been conducted to develop the modeling of vibrations in a spinning shaft carrying a number of rigid disks in Refs. [32–34].

Khader [35] and Oh et al [36] studied the stability of asymmetric Timoshenko rotors carrying disks was studied with the help of the Finite Element Method (FEM). The Finite Element Method was also employed by Chen et al [37] to perform stability analysis on a cantilever Timoshenko shaft-disk system subjected to axial periodic forces varying with time.

Bauer [5] discovered points where eigenvalues vanish for specific values of higher rotation speeds when studying a spinning slender beam with symmetric cross-sectional geometry. These points, called critical speeds, do not have oscillatory characteristics with no rotation orbits. Excited by static forces, they may lead to large-amplitude unstable responses.

Spinning systems owning asymmetric cross-sections (e.g., rectangular cross-sections), including mass or stiffness, are likely to experience divergence instabilities at higher rotation speeds [38]. Divergence instabilities refer to a type of dynamic response whose amplitude increases exponentially over time. The boundaries of divergence instabilities are typically determined by the critical speeds on both sides. Aouadi and Lakrad [39] investigated the stability of a double-hinged spinning beam using Rayleigh beam theory. Instabilities arise from asymmetry in the spinning systems studied numerically with the help of the finite element method [36, 40, 41] and Perturbation methods [42–44]. Genta and other researchers employed Floquet's theory to perform stability analysis on the results. Khader and Magableh [45] investigated the stability of the Asymmetric spinning Timoshenko beam carrying an asymmetric rigid disk, supported by anisotropic flexible bearings subject to harmonic follower force. They utilized the Lagrangian approach combined with the assumed modes method to derive the governing equations of motion and Floquet's theory to examine the system stability.

Another phenomenon resulting from the geometrical asymmetry in rotating systems is the veering of natural frequencies. Jei and Lee [46] performed modal analysis on the asymmetric spinning rotor using complex modal displacements. They show that some curve veering arises in the eigenvalue results over the spinning speed, in which abrupt but continuous changes occur in the mode shapes. Khader [35] also studied the stability of an asymmetric rotor with an asymmetric flexible disk supported by two identical flexible bearings on both sides by employing the combined Lagrangian approach with the Rayleigh-Ritz method. It demonstrated that asymmetry in the rotor leads to the veering behavior in the frequency results along with flutter and divergences instabilities.

1.1.3 Scope and aims

This research employed the Timoshenko beam theory to study the vibrational behavior of a spinning cantilever beam with a rigid body attached at its free end for both symmetric and asymmetric cross-sectional geometries. This modeling integrates rotary inertia, shear deformations, as well as gyroscopic effects. The governing equations of motions are derived in the form of the hybrid discrete-continuous system model. These equations are redefined in extended operator formulation to facilitate discretization by the Galerkin method and also incorporate the gyroscopic nature. A sufficient number of orthogonal polynomial basis functions are used to numerically compute the multiple modes with satisfactory precision.

Vibration characteristics and stability of the dynamic system are investigated for both symmetric and asymmetric systems for a wide range of rotation speeds. In this study, symmetry constitutes identical geometries aligned with two perpendicular cross-section axes, and it is considered asymmetric when this condition is not met. Modal coupling and veering interactions are analyzed for asymmetric spinning systems in detail. The impacts of variations in the parameters of the beam and the rigid body on instability and critical speeds are investigated for a wide range of rotation speeds. Furthermore, unusual interactions between high-speed instabilities are identified and analyzed thoroughly.

An analytical closed-form solution is derived for the spinning symmetric system comprising a cantilever beam and a rigid tip body using the complex-valued format. The analytical closed-form solution is advantageous for evaluating the accuracy of numerical solutions, especially for higher modes. It can also be employed as a basis function for further numerical analysis of similar complex systems. ANSYS simulation using the finite element method is also utilized to evaluate the validity of the results obtained by the mathematical modeling presented in this study. Variations in the natural frequencies, modal characteristics, and instabilities of both symmetric and asymmetric systems are simulated by ANSYS software for a range of rotation speeds. The results from this simulation are then compared with the ones obtained by the presented analytical modeling for further analysis.

1.2 Dielectric elastomer membrane actuator

1.2.1 Motivation

Dielectric elastomers are a class of soft electroactive materials that have been used for soft robots [47–54], actuators [55–61], energy generators [62–68], and sensors [69–73]. Dielectric elastomers are soft, highly deformable elastomeric materials with sufficiently-low conductivity that the material behaves as an insulator. Dielectric elastomers have been shown to experience large deformations with greater than 100 percent, have a high energy density greater than 3.4 $\mathrm{MJ/m^3}$, exhibit fast response times on the order of milliseconds, are lightweight, can be easily manufactured into complex shapes, and have low overall costs.

In applications, a thin dielectric elastomer membrane is coated on its upper and lower surfaces using a compliant electrode, like carbon powder or a layer of carbon-filled grease. Because of the insulating property of the material, the application of a voltage through its thickness forces like charges on the upper and lower electrodes. These charges attract, generating a Maxwell stress within the material. This loading results in deformation that reduces the material thickness and increases its area. In applications, dielectric elastomers have been used with circular, rectangular, and spherical geometries. A schematic of a circular dielectric elastomer membrane is shown in Fig. 1.3.

1.2.2 Literature review

Because the elastomeric materials experience large deformations, their mechanical behavior must be captured using hyperelastic material models. A large number of

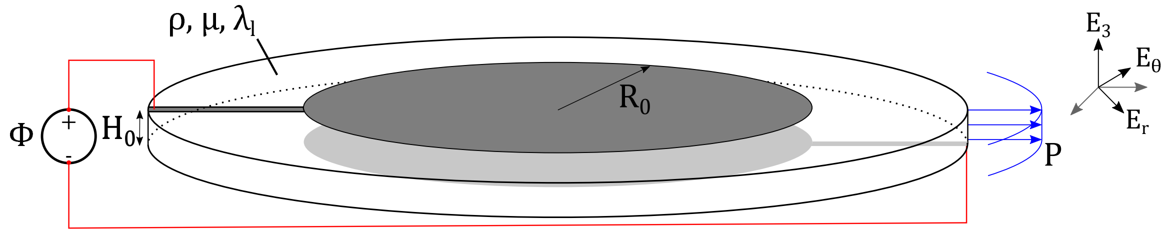

Figure 1.3: Schematic of a circular dielectric elastomer membrane

hyperelastic models are available for materials that experience large deformations. Early hyperelastic models include the Neo-Hookean [74] and Mooney-Rivlin [75, 76] models. These models are restricted to moderate stretches because instabilities may result from their use at larger stretches. Since those models were proposed, several other models have appeared that include the material's strain stiffening behavior at large stretches. These include the Arruda-Boyce [77], Ogden [78], Gent [79], and Lopez-Pamias [80] models. Many of these models have been used for analyzing the static and dynamic behavior of dielectric elastomer membranes and structures.

The acrylic elastomer VHB manufactured by 3M is a common material used for dielectric elastomer transducer applications. This elastomer is an extremely soft material, with a low shear modulus that is capable of huge stretches [81]. Uniaxial stretches of this material have been in the hundreds of percent. Its maximum stretch possible exceeds 800 percent. Because it is so soft, voltage-induced deformations over 2000 percent areal strains have been demonstrated in tubular membranes [82]. VHB is commonly modeled using the Gent hyperelastic material model because of its excellent ability to replicate the material stress-stretch behavior in standard material testing [83].

Pelrine et al. [84] experimentally measured large actuation stretches in acrylic elastomers under applied electric fields. This data inspired the later studies to perform constitutive model fitting to capture nonlinear mechanical behavior under coupled electro-mechanical effects. Wissler et al. [81] conducted finite element simulations to capture nonlinear electro- mechanical behaviors of acrylic elastomers and evaluate experimental observations. Zhao et al. developed a theoretical model fitted to experimental data to predict the softening behavior, electromechanical instability, and failure of dielectric elastomers. Ogden et al. [85] compared the ability of some hyperelastic formulations, such as Mooney–Rivlin, Ogden, and Gent-Gent models, to capture strain-stiffening behavior of an elastomeric material by fitting them to equibiaxial and biaxial data. Horgan [86] demonstrates that hyperelastic models like Gent that incorporate limiting chain extensibility in their formulations are able to predict strain-stiffening effects. Lopez-Pamies [80] proposed an I_1 based hyperelastic model with high flexibility that can accurately fit large stretches of rubber elastic materials using only a few terms. Chen et al. [83] characterized soft rubber-like materials for dielectric elastomer applications. The mechanical behavioir of these materials were not accurately predicted using the Gent model. An enhanced Gent model was able to accurately capture the stress-stretch behavior. Silicone rubbers, which are known for their low elastic modulus and high stretchability, are attractive candidates for dielectric elastomer applications. Several studies have extended hyperelastic models of dielectric elastomers by incorporating the viscoelastic effects to capture time-dependent behaviors [87–90].

Recently, the use of dielectric elastomers as actuators has been the subject of many studies due to their ability to generate large, reversible deformations under electrical stimulation [84, 91]. Pelrin et al. indicate that the application of planar pre-stretch improves the performance of dielectric elastomer actuators, which enhances electrical breakdown strength and enables the elastomer membrane to actuate primarily in the softer, low-prestrain planar direction and in thickness. Wissler et al. [92] demonstrate that both in-plane and out-of-plane Maxwell stress contribute to actuation, and the relative permittivity of acrylic elastomers like VHB materials decreases with increasing pre-stretch ratio. Wissler et al. [93]

derive an analytical solution for the instantaneous response of a pre-stretched circular actuator and studied the time-dependent behavior using finite element simulation. In this study, the hyperelastic models of Yeoh, Ogden, and Mooney-Rivlin are used. They also compared their results with experimental observations. Liang et al. [94] proposed an inverse lumped parameter model to analyze the non-uniform deformation of pre-stretched circular dielectric elastomer actuators.

Nonlinear behaviors are quite common in the deformations and vibrations of dielectric elastomers due to factors such as large deformations, material properties, and electro-mechanical coupling. Hence, developing a practical model that accurately captures their nonlinearities is crucial to effective dynamic analysis. The nonlinear dynamics of dielectric elastomer membranes have been studied in a wide range of research for various elastomer geometries, including spherical [95–98], rectangular [99–101], and circular elastomers [102–104]. They determined the frequency-amplitude diagram illustrating the oscillations with super-harmonic and sub-harmonic periods apart from the typical harmonic response.

The spherical thick-walled dielectric elastomer is investigated by Yong et al [97]. Alibakhshi and Heidari [105] presented an approximate analytical solution for the nonlinear vibrations of a dielectric Neo-Hookean spherical shell employing the multiple-scale method. Tang et al. [106] investigate the stability and nonlinear behaviors of a dielectric Neo-Hookean spherical shell with the help of the Newton–harmonic balance method.

Although several analytical studies [103, 107] have been conducted on the nonlinear dynamics and equilibrium responses of a pre-stretched circular dielectric membrane, numerical finite element simulations alongside experimental testing provide a robust validation benchmark. In these studies, the nonlinear characteristics of the frequency response, including the primary and secondary resonances, are investigated. Zhu et al. [96]

studied the nonlinear vibrations of spherical membranes under harmonic voltage excitations using the neo-Hookean strain energy function. Many studies incorporate the axial inertia in the nonlinear formulations to analyze the dynamic response of dielectric elastomers [101, 108–111]. Cooley and Lowe [103] numerically calculate the frequency response of the large-stretch in-plane nonlinear vibration of circular dielectric elastomer membranes at a nominal voltage below where snap-through instabilities are possible. The impacts of the transitions from the softening to hardening nonlinear behavior on the frequency response were also investigated by Cooley and Lowe [104].

1.2.3 Scope and aims

This work studies equilibrium hyperelastic deformations of pre-stretched circular dielectric elastomer membranes subjected to varying electric potentials. Two models of dielectric actuators are considered, where the membranes are pre-stretched either under a constant load or a constant stretch. Two observations from the mechanical behavior of dielectric elastomer materials are considered in this research. First, more than one hyperelastic model has been shown to accurately capture the mechanical behavior of an elastomeric material. Second, different elastomeric materials require different material models to capture their mechanical behavior. The impact of these effects on the behaviors of dielectric elastomer actuators has not been fully investigated. Numerical simulations are performed using the finite element method to validate the analytical analysis. The results are also compared with the experimental data reported by a separate research group. Variations in stretches throughout the whole body of the membrane are investigated over a wide range of applied electric potential using finite element simulations. This will increase the performance of soft material technologies in actuation, sensing, and energy harvesting, for example.

CHAPTER TWO

ANALYZING THE VIBRATIONS AND STABILITY OF THE SPINNING SYSTEM USING NUMERICAL METHODS

2.1 Introduction

Cantilevered beams with bodies attached to their tip that spin about their longitudinal axis are common structural elements used in resonator devices like MEMS gyroscopes [4, 112–125]. In these devices, the beam provides stiffness, the body at the tip provides inertia, gyroscopic effects couple the deformations, and the vibration produced is used for sensing. Tuning the structural resonances is of primary importance to the proper design of these devices. Furthermore, controlling their stability is essential to avoid failures in high-speed applications. It is the high-speed vibration and stability that motivates the present work.

A number of fundamental investigations on the vibration of spinning cantilevered beams have appeared in the literature. The vibration of spinning elastic beams with classical boundary conditions was investigated by Bauer [5]. It was assumed the beam was slender so that rotary inertia and shear deformation effects were neglected (i.e., Euler-Bernoulli beam theory was used). The vibration of spinning beams that include rotary inertia (i.e., Rayleigh beam theory) was studied by Lee and Jei [10] and Sheu and Yang [12]. The vibration of spinning beams including rotary inertia and shear deformations (i.e., Timoshenko beam theory) was investigated analytically by Zu and Han [18]. These fundamental studies led to modal analysis formulations [10, 13, 14, 126], analyses of natural frequency veering [127], and examination of the response due to moving forces [10, 14, 15], to name a few.

Spinning beams, unlike their stationary counterparts, have the potential to experience divergence and flutter instabilities at high rotation speeds. Divergence instability is characterized by an exponential growth of the resulting deformations. The boundaries of divergence instability are typically marked by critical speeds (defined as speeds where an eigenvalue vanishes). The critical speeds themselves are important for stability because static forces cause large-amplitude unstable responses. Exponentially-increasing oscillatory deformations occur for flutter instability. Bauer [5] identified critical speeds for slender, spinning beams analytically and numerically from natural frequency-speed diagrams. Only beams with identical cross-sectional geometry were considered. Divergence instability occurs for beams with non-identical cross-sections (e.g., rectangular cross-sections) [38]. The impact of rotary inertia on high-speed spinning beams was investigated by Aouadi and Lakrad [39]. An apparent under-explored area of research in spinning cantilevered beams is the effect that shear deformations have on high-speed stability behavior.

The vibration of stationary (i.e., non-spinning) cantilevered elastic beams with attached rigid bodies has been of longstanding interest to engineers. Laura et al. [19] analyzed the vibration of clamped-free beams with a mass attached to their end using an Euler-Bernoulli beam model. The specific case that the tip mass is large was analyzed in Refs. [23, 24]. The effect of eccentric mounting of the mass was investigated by Bhat and Wagner [28]. Analyses on the impact of fixed-end compliance [21, 128], non-uniform cross sections [129], base excitation [130], and damping [131] followed. The vibration of cantilevered Timoshenko beams with attached rigid bodies at their free end was investigated in Refs. [20, 132].

Shear deformation effects are commonly included in rotordynamic studies, where shafts are often short and thick. Finite element formulations have been developed in Refs. [133–136]. The vibration of multi-step rotors has been investigated in Refs. [137–139]. Eshleman and Eubanks [29] analytically investigated the vibration of spinning shafts, including shear deformation effects, with an attached rigid disk. The vibration of spinning shear deformable shafts with multiple attached masses was investigated in Refs. [31]. Mirtalaie and Hajabasi [140] analyzed the vibration of spinning Timoshenko beams using the total rotation angles of the beam cross-section, which led to time-dependent coefficients in the governing equations. Chen and Ku [37] analyzed the stability of cantilevered Timoshenko shafts with a disk at their end and periodic axial forces. The stability of asymmetric rotors has been investigated in Refs. [35, 36], for example. Jahangiri et al. [141] analyzed torsional coupling resulting from gyroscopic effects in small-scale rotors.

In this work, the vibration of spinning cantilevered beams with a rigid body attached at its free end is investigated accounting for shear deformation and rotary inertia in the beam. The resulting hybrid discrete-continuous system model is written in extended operator form to exemplify its gyroscopic system features and permit discretization using Galerkin's method. Example numerical results are determined for beams with identical and non-identical cross-sectional geometries and rigid body moments of inertia, which demonstrate the impact of symmetry on the high-speed dynamic behavior. The vibration characteristics are examined in terms of the forward and backward orbit modal properties. Veering interactions are analyzed in terms of the strength of modal coupling. The critical speeds and high-speed stability are investigated for wide ranges of beam and rigid body parameters. Unusual stability behaviors observed in parametric studies are identified and discussed.

2.2 Modelling

A schematic of a cantilevered beam with a rigid body attached at its end is shown in Fig. 2.1. The system rotates about its longitudinal axis at a constant speed Ω. The beam has length L and cross-sectional area A. The cross-section is assumed to have two planes of symmetry so that bending in one direction does not generate bending in the other direction.

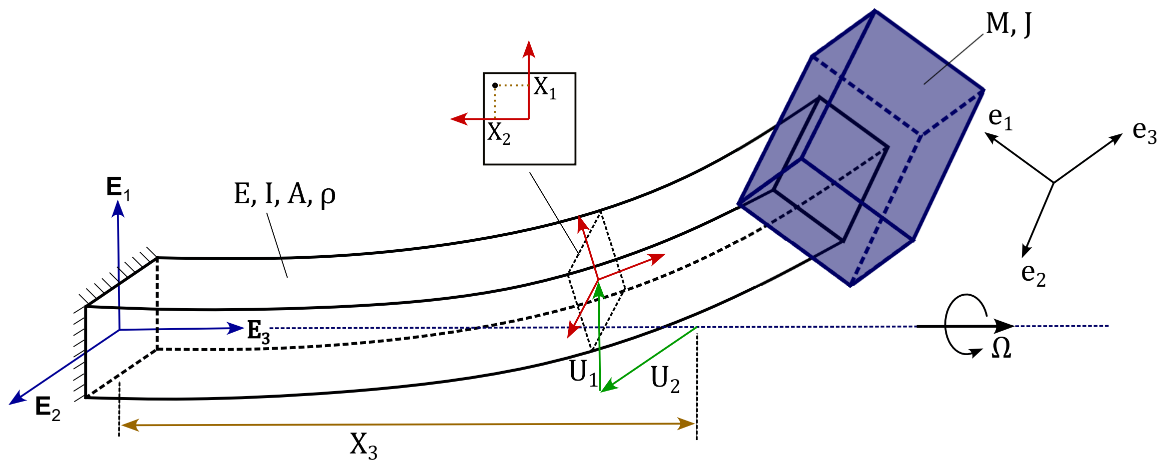

Figure 2.1: Schematic of a spinning cantilevered beam with a rigid body attached to its free end. The beam spins at a constant speed about its longitudinal axis.

The beam is made of an isotropic elastic material with density ρ, elastic modulus E, and shear modulus G.

We define a fixed, inertial basis as $\{\mathbf{i},\mathbf{j},\mathbf{k}\}$ (not shown). The basis $\{\mathbf{E}_1,\mathbf{E}_2,\mathbf{E}_3\}$ is defined from the inertial basis by a rotation of ΩT about $\mathbf{E}_3 = \mathbf{k}$ at time T. The neutral axis of the beam coincides with $\mathbf{E}_3$ in the reference configuration before deformation. The base vectors $\mathbf{E}_1$ and $\mathbf{E}_2$ are oriented along the principle axes of the cross-section. Locations along the beam span are defined by the coordinate X_3 with $0 < X_3 < L$ defining the domain. Positions on the beam cross-section are defined by the coordinates X_1 and X_2.

In resonator devices, the structural resonances of the beam are controlled using a small element at the beam tip $X_3 = L$. We model this element as a rigid body. Before deformation, the mass center of the rigid body is located along the $\mathbf{E}_3$ axis but offset from the beam tip by a distance of d. The basis $\{\mathbf{e}_1,\mathbf{e}_2,\mathbf{e}_3\}$ is a body-fixed basis attached to the rigid body at its mass center. The relationship between it and $\{\mathbf{E}_1,\mathbf{E}_2,\mathbf{E}_3\}$ will be determined from the beam bending deformations at its endpoint. The rigid body has mass M and mass moment of inertia $\mathbf{J} = J_{11}\mathbf{e}_1\otimes\mathbf{e}_1 + J_{22}\mathbf{e}_2\otimes\mathbf{e}_2 + J_{33}\mathbf{e}_3\otimes\mathbf{e}_3$ about its mass center.

The tensor formed by vectors $\mathbf{a}$ and $\mathbf{b}$ is denoted $\mathbf{a} \otimes \mathbf{b}$. It is defined by its action on vector $\mathbf{c}$ as $(\mathbf{a} \otimes \mathbf{b})\mathbf{c} = (\mathbf{b} \cdot \mathbf{c})\mathbf{a}$, where $\mathbf{b} \cdot \mathbf{c}$ denotes the dot product of $\mathbf{b}$ and $\mathbf{c}$.

We assume that cross-sections in the plane remain planar after deformation. Warping of the cross-section during deformation is neglected. We focus on the beam's bending deformations so axial and torsional deformations are omitted. In vibration analyses where strains remain infinitesimal, these motions do not couple with the bending deformations. For larger vibrations with finite strains, coupling between bending and torsion or extension occurs [142, 143]. The position of a material particle on the beam before deformation is $\mathbf{r}_{b0} = X_1\mathbf{E}_1 + X_2\mathbf{E}_2 + X_3\mathbf{E}_3$. After an assumed bending deformation, the position of this material particle at time T is

$$\begin{aligned}
\mathbf{r}_b = {} & [X_1 \cos\theta_2(X_3,T) + U_1(X_3,T) + X_2 \sin\theta_1(X_3,T)\sin\theta_2(X_3,T)]\mathbf{E}_1 \\
& + [X_2 \cos\theta_1(X_3,T) + U_2(X_3,T)]\,\mathbf{E}_2 \\
& + [X_3 - X_1 \sin\theta_2(X_3,T) + X_2 \sin\theta_1(X_3,T)\cos\theta_2(X_3,T)]\,\mathbf{E}_3,
\end{aligned} \tag{2.1}$$

where $U_1(X_3,T)$ and $U_2(X_3,T)$ are bending displacements along $\mathbf{E_1}$ and $\mathbf{E_2}$, respectively. The rotational deformations $\theta_1(X_3,T)$ and $\theta_2(X_3,T)$ are about $\mathbf{E}_1$ and $\mathbf{E}_2$. These are also associated with beam bending. They are not determined from the bending displacements, however. We take them as independent of the bending displacements to allow for shearing of small differential elements within the beam span. We retain the full nonlinear form of the position in Eq. (2.1). This is to capture all quadratic terms that will be produced in the kinetic energy equation. The use of only linear terms for infinitesimal strains would result in the omission of centripetal acceleration terms in the final equations of motion for the beam.

Before deformation, the position of the mass center of the rigid body is $\mathbf{r}_{M0} = \mathbf{r}_{b0}|_{X_3=L} + d\mathbf{E}_3$. The position after deformation is

$$\mathbf{r}_M = \mathbf{r}_b\big|_{X_3=L} + d\mathbf{e}_3 = U_{1c}\,\mathbf{E}_1 + U_{2c}\,\mathbf{E}_2 + (L + d\cos\Theta_1\cos\Theta_2)\,\mathbf{E}_3, \tag{2.2a}$$

$$U_{1c}(T) = U_1(L,T) + d\cos\Theta_1\sin\Theta_2, \quad U_{2c}(T) = U_2(L,T) - d\sin\Theta_1, \tag{2.2b}$$

$$\Theta_1(T) = \theta_1(L,T), \quad \Theta_2(T) = \theta_2(L,T) \tag{2.2c}$$

U_{1c} and U_{2c} are the displacements of the rigid body's mass center along $\mathbf{E}_1$ and $\mathbf{E}_2$, respectively. Θ_2 is the rotation of the rigid body about $\mathbf{E}_2$. The rotation Θ_1 is about $\mathbf{E}_1$. The rotation of $\{\mathbf{i},\mathbf{j},\mathbf{k}\}$ to $\{\mathbf{e}_1,\mathbf{e}_2,\mathbf{e}_3\}$ is defined as a 3-2-1 Euler rotation sequence using the angles ΩT, Θ_2, and Θ_1. The angular velocity of the rigid body is

$$\omega_M = (\dot{\Theta}_1 - \Omega\sin\Theta_2)\mathbf{e}_1 + (\dot{\Theta}_2 + \Omega\cos\Theta_2\sin\Theta_1)\mathbf{e}_2 + (\Omega\cos\Theta_2\cos\Theta_1 - \dot{\Theta}_2\sin\Theta_1)\mathbf{e}_3 \tag{2.3}$$

Equation (2.3) retains all nonlinear terms in the rotations so that all linear terms are captured in the kinetic energy expression determined later.

The deformation at any material point on the beam is $\mathbf{v} = \mathbf{r}_b - \mathbf{r}_{b0}$. Motivated by the small vibrations that will be analyzed, we calculate the strains from the infinitesimal strain tensor $\varepsilon_{ij} = (v_{i,j} + v_{j,i})/2$, where $(\cdot)_{,i} = \partial(\cdot)/\partial X_i$ and the indices $i,j = 1,2,3$. Use of the linearized form of the deformation $\mathbf{v}$ gives the infinitesimal strains as

$$\varepsilon_{13} = \frac{U_{1,3} - \theta_2}{2}, \quad \varepsilon_{23} = \frac{U_{2,3} + \theta_1}{2}, \quad \varepsilon_{33} = -X_1\theta_{2,3} + X_2\theta_{1,3} \tag{2.4}$$

The assumed kinematics of deformation result in constant shear strains through the thickness of the beam, as seen by the absence of X_1 and X_2 in ε_{13} and ε_{23}. The variation in these strains throughout the cross section will be accounted for using shear correction factors that depend on the cross-section geometry.

The beam is made from a material that is linear, elastic, and isotropic (i.e., the material is Hookean). The stress-strain relationships are $\sigma_{33} = E\varepsilon_{33}$, $\sigma_{13} = 2k_{13}G\varepsilon_{13}$, and $\sigma_{23} = 2k_{23}G\varepsilon_{23}$. k_{13} and k_{23} are shear correction factors that, in general, depend on the cross-section's geometry and the material's Poisson's ratio [144, 145]. The strain energy of the beam is $S = 1/2 \int_0^L \int_A \sigma_{ij}\varepsilon_{ij} \mathrm{d}A\mathrm{d}X_3$. Use of Eq. (2.4) and the material constitutive behavior gives the strain energy as

$$S = \frac{1}{2}\int_0^L \left[k_{13}GA(U_{1,3} - \theta_2)^2 + k_{23}GA(U_{2,3} + \theta_1)^2 + EI_{22}\theta_{1,3}^2 + EI_{11}\theta_{2,3}^2\right] \mathrm{d}X_3 \quad (2.5)$$

where the cross-sectional area $A = \int_A \mathrm{d}A$. The cross-sectional area moments of inertia are $I_{11} = \int_A X_1^2 \mathrm{d}A$ and $I_{22} = \int_A X_2^2 \mathrm{d}A$. In Eq. (2.5) the product of inertia $I_{12} = \int_A X_1 X_2 \mathrm{d}A$ vanishes because the beam cross-section is assumed to have two planes of symmetry.

The kinetic energy of the beam is $K_b = 1/2 \int_0^L \rho A \dot{\mathbf{r}}_b \cdot \dot{\mathbf{r}}_b \mathrm{d}X_3$, where the overdot $\dot{()} = \partial/\partial T$ denotes time differentiation. Substitution of the time derivative of Eq. (2.1) into the kinetic energy expression gives

$$\begin{aligned} K_b = \frac{1}{2}\int_0^L \Big[&\rho A(\dot{U}_1 - \Omega U_2)^2 + \rho A(\dot{U}_2 + \Omega U_1)^2 + \rho I_{11}\dot{\theta}_2^2 + \rho I_{22}\dot{\theta}_1^2 \\ &+ \Omega^2 \rho I_{11}(1 - \theta_2^2) + \Omega^2 \rho I_{22}(1 - \theta_1^2) - 2\Omega\rho I_{22}\left(\dot{\theta}_1\theta_2 + \theta_1\dot{\theta}_2\right)\Big] \mathrm{d}X_3 \quad (2.6) \end{aligned}$$

where cubic and higher terms have been omitted because they do not produce terms in the linear equations of motion.

The kinetic energy of the rigid body is $K_M = (1/2)M\dot{\mathbf{r}}_M \cdot \dot{\mathbf{r}}_M + (1/2)\omega_c \cdot (\mathbf{J}_M\omega_c)$. After use of the time derivative of Eqs. (2.2) and (2.3), the rigid body kinetic energy becomes

$$\begin{aligned} K_M = &\frac{1}{2}M[(\dot{U}_{1c} - \Omega\, U_{c2})^2 + (\dot{U}_{2c} + \Omega U_{c1})^2] + \frac{1}{2}J_{11}(\dot{\Theta}_1 - \Omega\Theta_2)^2 \\ &+ \frac{1}{2}J_{22}(\dot{\Theta}_2 + \Omega\Theta_1)^2 + \frac{1}{2}J_{33}\left[\Omega^2 - 2\Omega\dot{\Theta}_2\Theta_1 - \Omega^2(\Theta_1^2 + \Theta_2^2)\right] \quad (2.7) \end{aligned}$$

The total kinetic energy for the beam-mass system is $K = K_b + K_M$.

The governing equations are derived from Hamilton's principle $\int_{t_1}^{t_2}(\delta K - \delta S)\mathrm{d}t = 0$. The variation in the kinetic energy δK is calculated from the total kinetic energy with the use of Eqs. (2.6) and (2.7). δS is calculated from Eq. (2.5). The geometric boundary conditions at the fixed end are $U_1(0,T) = 0$, $U_2(0,T) = 0$, $\theta_1(0,T) = 0$, and $\theta_2(0,T) = 0$. The resulting equations of motion and natural boundary conditions are

$$\rho A\ddot{U}_1 - 2\Omega\rho A\dot{U}_2 - k_{13}GA(U_{1,33} - \theta_{2,3}) - \Omega^2\rho AU_1 = 0 \tag{2.8a}$$

$$\rho A\ddot{U}_2 + 2\Omega\rho A\dot{U}_1 - k_{23}GA(U_{2,33} + \theta_{1,3}) - \Omega^2\rho AU_2 = 0 \tag{2.8b}$$

$$\rho I_{22}\ddot{\theta}_1 + k_{23}GA(U_{2,3} + \theta_1) - EI_{22}\theta_{1,33} + \Omega^2\rho I_{22}\theta_1 = 0 \tag{2.8c}$$

$$\rho I_{11}\ddot{\theta}_2 - k_{13}GA(U_{1,3} - \theta_2) - EI_{11}\theta_{2,33} + \Omega^2\rho I_{11}\theta_2 = 0, \quad 0 < X_3 < L \tag{2.8d}$$

$$M\ddot{U}_{1c} - 2\Omega M\dot{U}_{2c} + k_{13}GA(U_{1,3} - \theta_2)\big|_L - \Omega^2 MU_{1c} = 0 \tag{2.9a}$$

$$M\ddot{U}_{2c} + 2\Omega M\dot{U}_{1c} + k_{23}GA(U_{2,3} + \theta_1)\big|_L - \Omega^2 MU_{2c} = 0 \tag{2.9b}$$

$$J_{11}\ddot{\Theta}_1 - \Omega(J_{11} + J_{22} - J_{33})\dot{\Theta}_2 + EI_{22}\theta_{1,3}\big|_L + dk_{23}GA(U_{2,3} + \theta_1)\big|_L - \Omega^2(J_{22} - J_{33})\Theta_1 = 0 \tag{2.9c}$$

$$J_{22}\ddot{\Theta}_2 + \Omega(J_{11} + J_{22} - J_{33})\dot{\Theta}_1 + EI_{11}\theta_{2,3}\big|_L - dk_{13}GA(U_{1,3} - \theta_2)\big|_L - \Omega^2(J_{11} - J_{33})\Theta_2 = 0 \tag{2.9d}$$

Equations (2.8) and (2.9) are a set of partial differential equations for the beam that are coupled to a set of ordinary differential equations for the rigid body. Gyroscopic terms, which are proportional to the rotation speed Ω, appear in the equations for the translational deformations in Eqs. (2.8a) and (2.8b). There are no gyroscopic terms in Eqs. (2.8c) and (2.8d) for the rotational deformations. Gyroscopic terms appear in all equations for the rigid body, as seen in Eqs. (2.9). All equations for the beam (Eqs. (2.8)) and rigid body (Eqs. (2.9)) contain centripetal terms proportional to Ω^2.

Equations (2.8) agree with those derived in Ref. [14] for the case that the beam is symmetric and there is no rigid body at its tip. Equations (2.8) and (2.9) reduce to those in Ref. [39] for the special case that there is no rigid body and shear deformations are negligible with $\kappa \to \infty$. Further neglecting rotary inertia, Eqs. (2.8) and (2.9) reduce to those in Ref. [5]. Equations (2.8a), (2.8d), (2.9a), and (2.9d) (and similarly Eqs. (2.8b), (2.8c), (2.9b), and (2.9c)) agree with those derived in Ref. [20] for vanishing rotation speed after algebraic manipulations.

2.2.1 Nondimensionalization

Equations (2.8) and (2.9) are nondimensionalized using the nondimensional variables

$$x_i = \frac{X_i}{L}, \quad t = \frac{1}{L^2}\sqrt{\frac{EI_{11}}{\rho A}}T, \quad u_{1,2} = \frac{U_{1,2}}{L}, \quad \hat{d} = \frac{d}{L}, \quad \kappa = \frac{GAL^2}{EI_{11}}, \quad \mu = \frac{I_{11}}{AL^2},$$
$$\alpha = \frac{I_{22}}{I_{11}}, \quad \eta = \frac{M}{\rho AL}, \quad \hat{\Omega} = \sqrt{\frac{\rho AL^4}{EI_{11}}}\Omega, \quad \nu_{11} = \frac{J_{11}}{\rho AL^3}, \quad \nu_{22} = \frac{J_{22}}{\rho AL^3}, \quad \nu_{33} = \frac{J_{33}}{\rho AL^3} \tag{2.10}$$

The variables above lead to the differentiation relationships $\partial()/\partial X_3 = (1/L)\partial()/\partial x_3$ and $\partial()/\partial T = \sqrt{EI_{11}/\rho AL^4}\partial()/\partial t$. Substitution of the nondimensional parameters in Eq. (2.10) into Eqs. (2.8) and (2.9) gives the nondimensional equations of motion and natural boundary conditions

$$\ddot{u}_1 - 2\hat{\Omega}\dot{u}_2 - k_{13}\kappa(u_{1,33} - \theta_{2,3}) - \hat{\Omega}^2 u_1 = 0 \tag{2.11a}$$

$$\ddot{u}_2 + 2\hat{\Omega}\dot{u}_1 - k_{23}\kappa(u_{2,33} + \theta_{1,3}) - \hat{\Omega}^2 u_2 = 0 \tag{2.11b}$$

$$\alpha\mu\ddot{\theta}_1 + k_{23}\,\kappa\,(u_{2,3} + \theta_1) - \alpha\theta_{1,33} + \hat{\Omega}^2\alpha\mu\theta_1 = 0 \tag{2.11c}$$

$$\mu\ddot{\theta}_2 - k_{13}\kappa(u_{1,3}-\theta_2) - \theta_{2,33} + \hat{\Omega}^2\mu\theta_2 = 0 \tag{2.11d}$$

$$\eta\ddot{u}_{1c} - 2\hat{\Omega}\eta\dot{u}_{2c} + k_{13}\kappa(u_{1,3}-\theta_2)\big|_1 - \hat{\Omega}^2\eta u_{1c} = 0 \tag{2.12a}$$

$$\eta\ddot{u}_{2c} + 2\hat{\Omega}\eta\dot{u}_{1c} + k_{23}\kappa(u_{2,3}+\theta_1)\big|_1 - \hat{\Omega}^2\eta u_{2c} = 0 \tag{2.12b}$$

$$\nu_{11}\ddot{\Theta}_1 - \hat{\Omega}(\nu_{11}+\nu_{22}-\nu_{33})\dot{\Theta}_2 + \alpha\theta_{1,3}\big|_1 + \hat{d}k_{23}\kappa(u_{2,3}+\theta_1)\big|_1 - \hat{\Omega}^2(\nu_{22}-\nu_{33})\Theta_1 = 0 \tag{2.12c}$$

$$\nu_{22}\ddot{\Theta}_2 + \hat{\Omega}(\nu_{11}+\nu_{22}-\nu_{33})\dot{\Theta}_1 + \theta_{2,3}\big|_1 - \hat{d}k_{13}\kappa(u_{1,3}-\theta_2)\big|_1 - \hat{\Omega}^2(\nu_{11}-\nu_{33})\Theta_2 = 0 \tag{2.12d}$$

The nondimensional boundary conditions at the fixed end constrain the displacements to $u_1(0,t) = 0$ and $u_2(0,t) = 0$. The rotational deformations $\theta_1(0,t) = 0$ and $\theta_2(0,t) = 0$ are also constrained.

2.2.2 Extended operator formulation

Equations (2.11) and (2.12) represent a set of coupled partial and ordinary differential equations. As given, they lack the mathematical operator structure identifying their gyroscopic system nature and facilitating their later discretization for numerical solution. We resolve that deficiency using the extended operator formulation [146, 147]. In the extended operator form, the system of equations in Eqs. (2.11) and (2.12) will have the expected operator adjointness properties of conservative gyroscopic systems. We will also leverage the extended operator formulation to discretize the equations using Galerkin's method. Extended operators have previously been used to analyze the vibration of spinning disk systems [148–150], belt-pulley systems [151, 152], planetary gears [153, 154], and beams with attached masses or rigid bodies [155, 156].

The extended variable is defined as

$$\mathbf{h} = [u_1(x_3,t),\ u_2(x_3,t),\ \theta_1(x_3,t),\ \theta_2(x_3,t),\ u_{1c}(t),\ u_{2c}(t),\ \Theta_1(t),\ \Theta_2(t)]^T \tag{2.13}$$

$\mathbf{h}$ is an element of the Hilbert space $\mathscr{H}$, which consists of complex-valued vectors with components h_{1-4} as square-integrable functions continuous over the beam span and h_{5-8} as scalars. The elements h_{1-4} must have vanishing displacements at $x_3 = 0$ to satisfy the necessary clamped conditions at the fixed end. The elements of $\mathbf{h}$ are related because of geometric compatibility at the interface between the beam tip and rigid body. Specifically, translational compatibility yields $h_5 = h_1(1) + \hat{d}h_4(1)$ and $h_6 = h_2(1) - \hat{d}h_3(1)$. From compatibility of rotations $h_7 = h_3(1)$ and $h_8 = h_4(1)$.

The extended operators are determined from Eqs. (2.11) and (2.12) using the extended variable in Eq. (2.13). The mass, gyroscopic, stiffness, and centripetal operators are

$$\mathbf{M}\ddot{\mathbf{h}} = \begin{bmatrix} \ddot{u}_1 \\ \ddot{u}_2 \\ \alpha\mu\ddot{\theta}_1 \\ \mu\ddot{\theta}_2 \\ \eta\ddot{u}_{1c} \\ \eta\ddot{u}_{2c} \\ \nu_{11}\ddot{\Theta}_1 \\ \nu_{22}\ddot{\Theta}_2 \end{bmatrix} \tag{2.14a}$$

$$\Omega\mathbf{G}\dot{\mathbf{h}} = \begin{bmatrix} -2\hat{\Omega}\dot{u}_2 \\ 2\hat{\Omega}\dot{u}_1 \\ 0 \\ 0 \\ -2\hat{\Omega}\eta\,\dot{u}_{2c} \\ 2\hat{\Omega}\eta\,\dot{u}_{1c} \\ -\hat{\Omega}(\nu_{11}+\nu_{22}-\nu_{33})\dot{\Theta}_2 \\ \hat{\Omega}(\nu_{11}+\nu_{22}-\nu_{33})\dot{\Theta}_1 \end{bmatrix} \tag{2.14b}$$

$$\mathbf{K}\mathbf{h} = \begin{bmatrix} -k_{13}\kappa(u_{1,33}-\theta_{2,3}) \\ -k_{23}\kappa(u_{2,33}+\theta_{1,3}) \\ k_{23}\kappa(u_{2,3}+\theta_1)-\alpha\theta_{1,33} \\ -k_{13}\kappa(u_{1,3}-\theta_2)-\theta_{2,33} \\ k_{13}\kappa(u_{1,3}-\theta_2)\big|_1 \\ k_{23}\kappa(u_{2,3}+\theta_1)\big|_1 \\ \alpha\theta_{1,3}\big|_1+\hat{d}k_{23}\kappa(u_{2,3}+\theta_1)\big|_1 \\ \theta_{2,3}\big|_1-\hat{d}k_{13}\kappa(u_{1,3}-\theta_2)\big|_1 \end{bmatrix} \tag{2.14c}$$

$$-\Omega^2\mathbf{C}\mathbf{h} = \begin{bmatrix} -\hat{\Omega}^2\,u_1 \\ -\hat{\Omega}^2\,u_2 \\ \hat{\Omega}^2\,\alpha\,\mu\,\theta_1 \\ \hat{\Omega}^2\,\mu\,\theta_2 \\ -\hat{\Omega}^2\,\eta\,u_{1c} \\ -\hat{\Omega}^2\,\eta\,u_{2c} \\ -\hat{\Omega}^2\,(\nu_{22}-\nu_{33})\,\Theta_1 \\ -\hat{\Omega}^2\,(\nu_{11}-\nu_{33})\,\Theta_2 \end{bmatrix} \tag{2.14d}$$

The use of the extended variable in Eq. (2.13) and the extended operators in Eq. (2.14) give the equation of motion in standard conservative gyroscopic system form as

$$\mathbf{M}\ddot{\mathbf{h}} + \hat{\Omega}\mathbf{G}\dot{\mathbf{h}} + \left(\mathbf{K} - \hat{\Omega}^2\mathbf{C}\right)\mathbf{h} = \mathbf{0} \tag{2.15}$$

Substitution of the separable solution $\mathbf{h}(t) \to \mathbf{h}e^{\lambda t}$ into Eq. (2.15) gives the eigenvalue problem

$$\lambda^2\mathbf{M}\mathbf{h} + \lambda\hat{\Omega}\mathbf{G}\mathbf{h} + \left(\mathbf{K} - \hat{\Omega}^2\mathbf{C}\right)\mathbf{h} = \mathbf{0} \tag{2.16}$$

The inner product on $\mathscr{H}$ is defined as

$$\langle \mathbf{u}, \mathbf{v} \rangle = \int_0^1 (\bar{u}_1 v_1 + \bar{u}_2 v_2 + \bar{u}_3 v_3 + \bar{u}_4 v_4)\, \mathrm{d}x_3 + \bar{u}_5 v_5 + \bar{u}_6 v_6 + \bar{u}_7 v_7 + \bar{u}_8 v_8 \tag{2.17}$$

where $\mathbf{u}$ and $\mathbf{v}$ are elements of $\mathscr{H}$. The mass ($\langle \mathbf{u}, \mathbf{M}\mathbf{v} \rangle = \langle \mathbf{M}\mathbf{u}, \mathbf{v} \rangle$), stiffness ($\langle \mathbf{u}, \mathbf{K}\mathbf{v} \rangle = \langle \mathbf{K}\mathbf{u}, \mathbf{v} \rangle$), and centripetal operators ($\langle \mathbf{u}, \mathbf{C}\mathbf{v} \rangle = \langle \mathbf{C}\mathbf{u}, \mathbf{v} \rangle$) are self-adjoint. The gyroscopic operator ($\langle \mathbf{u}, \mathbf{G}\mathbf{v} \rangle = -\langle \mathbf{G}\mathbf{u}, \mathbf{v} \rangle$) is skew-self-adjoint. The mass and stiffness operators are positive definite, that is, $\langle \mathbf{u}, \mathbf{M}\mathbf{u} \rangle \geq 0$ and $\langle \mathbf{u}, \mathbf{K}\mathbf{u} \rangle \geq 0$. The equality only holds when $\mathbf{u} = \mathbf{0}$. With these operator adjointness and definiteness properties, the system is guaranteed to have purely imaginary eigenvalues below the first critical speed [157–159]. Furthermore, the eigenvalues and corresponding eigenvectors occur in complex conjugate pairs.

2.2.3 Discretization

Analytical solutions of Eq. (2.16) are difficult. We seek approximate solutions using Galerkin discretization. A benefit of the extended operator structure defined in Eqs. (2.13) and (2.14) is the straightforward application of approximate techniques like Galerkin's method. The approximate extended vector $\mathbf{h}_a$ is expanded as

$$\mathbf{h}_a = \sum_{k=1}^{N_1} a_{1k}\mathbf{h}_k^{(1)} + \sum_{l=1}^{N_2} a_{2l}\mathbf{h}_l^{(2)} + \sum_{m=1}^{M_1} b_{1m}\mathbf{h}_m^{(3)} + \sum_{n=1}^{M_2} b_{2n}\mathbf{h}_n^{(4)} \tag{2.18a}$$

$$\mathbf{h}_k^{(1)} = [\phi_{1k}(x_3), 0, 0, 0, \phi_{1k}(1), 0, 0, 0]^T \tag{2.18b}$$

$$\mathbf{h}_l^{(2)} = [0, \phi_{2l}(x), 0, 0, 0, \phi_{2l}(1), 0, 0]^T \tag{2.18c}$$

$$\mathbf{h}_m^{(3)} = [0, 0, \psi_{1m}(x), 0, 0, -\hat{d}\psi_{1m}(1), \psi_{1m}(1), 0]^T \tag{2.18d}$$

$$\mathbf{h}_n^{(4)} = [0, 0, 0, \psi_{2n}(x), \hat{d}\psi_{2n}(1), 0, 0, \psi_{2n}(1)]^T \tag{2.18e}$$

ϕ_{1k}, ϕ_{2l}, ψ_{1n}, and ψ_{2m} satisfy the geometric boundary conditions that require them to vanish at $x_3 = 0$. This ensures $\mathbf{h}_k^{(1)}$, $\mathbf{h}_l^{(2)}$, $\mathbf{h}_m^{(3)}$, and $\mathbf{h}_n^{(4)}$ are admissible vectors.

Because Eq. (2.18) is not a true eigenvector, the use of it into Eq. (2.16) does not result in the vanishing of its right-hand side. Instead, a residue $\mathbf{R} \in \mathscr{H}$ remains that is dependent on the numbers of basis functions used N_1, N_2, M_1, and M_2. The expansion coefficients are determined by the requirement that the vectors $\mathbf{h}_k^{(1)}$, $\mathbf{h}_l^{(2)}$, $\mathbf{h}_m^{(3)}$ and $\mathbf{h}_n^{(4)}$ are all separately orthogonal to $\mathbf{R}$. This process results in the discretized eigenvalue problem

$$\lambda^2[\mathbf{M}]\{\mathbf{h}\} + \lambda\hat{\Omega}[\mathbf{G}]\{\mathbf{h}\} + ([\mathbf{K}] - \hat{\Omega}^2[\mathbf{C}])\{\mathbf{h}\} = 0 \tag{2.19a}$$

$$\{\mathbf{h}\} = [a_{11}, a_{12}, \ldots, a_{1N_1}, a_{21}, a_{22}, \ldots, a_{2N_2}, b_{11}, b_{12}, \ldots, b_{1M_1}, b_{21}, b_{22}, \ldots, b_{2M_2}]^T \tag{2.19b}$$

The mass, gyroscopic, stiffness, and centripetal matrices in Eq. (2.19a) are

$$[\mathbf{M}] = \begin{bmatrix} [\mathbf{M}_{11}] & \mathbf{0} & \mathbf{0} & [\mathbf{M}_{14}] \\ \mathbf{0} & [\mathbf{M}_{22}] & [\mathbf{M}_{23}] & \mathbf{0} \\ \mathbf{0} & [\mathbf{M}_{32}] & [\mathbf{M}_{33}] & \mathbf{0} \\ [\mathbf{M}_{41}] & \mathbf{0} & \mathbf{0} & [\mathbf{M}_{44}] \end{bmatrix} \tag{2.20a}$$

$$[\mathbf{M}_{11}]_{pk} = \int_0^1 \overline{\phi_{1p}}\phi_{1k}\mathrm{d}x_3 + \eta\overline{\phi_{1p}(1)}\phi_{1k}(1), \quad p,k = 1,2,\ldots,N_1 \tag{2.20b}$$

$$[\mathbf{M}_{22}]_{ql} = \int_0^1 \overline{\phi_{2q}}\phi_{2l}\mathrm{d}x_3 + \eta\overline{\phi_{2q}(1)}\phi_{2l}(1), \quad q,l = 1,2,\ldots,N_2 \tag{2.20c}$$

$$[\mathbf{M}_{33}]_{rm} = \int_0^1 \alpha\mu\overline{\psi_{1r}}\psi_{1m}\mathrm{d}x_3 + (\nu_{11} + \hat{d}^2\eta)\overline{\psi_{1r}(1)}\psi_{1m}(1), \quad r,m = 1,2,\ldots,M_1 \tag{2.20d}$$

$$[\mathbf{M}_{44}]_{sn} = \int_0^1 \mu\,\overline{\psi_{2s}}\psi_{2n}\mathrm{d}x_3 + (\nu_{22} + \hat{d}^2\eta)\overline{\psi_{2s}(1)}\psi_{2n}(1), \quad s,n = 1,2,\ldots,M_2 \tag{2.20e}$$

$$[\mathbf{M}_{14}]_{pn} = \overline{[\mathbf{M}_{41}]_{np}} = \hat{d}\eta\overline{\phi_{1p}(1)}\psi_{2n}(1) \tag{2.20f}$$

$$[\mathbf{M}_{23}]_{qm} = \overline{[\mathbf{M}_{32}]_{mq}} = -\hat{d}\eta\overline{\phi_{2q}(1)}\psi_{1m}(1) \tag{2.20g}$$

$$[\mathbf{G}] = \begin{bmatrix} \mathbf{0} & [\mathbf{G}_{12}] & [\mathbf{G}_{13}] & \mathbf{0} \\ [\mathbf{G}_{21}] & \mathbf{0} & \mathbf{0} & [\mathbf{G}_{24}] \\ [\mathbf{G}_{31}] & \mathbf{0} & \mathbf{0} & [\mathbf{G}_{34}] \\ \mathbf{0} & [\mathbf{G}_{42}] & [\mathbf{G}^{\mathbf{dc}}] & \mathbf{0} \end{bmatrix} \tag{2.21a}$$

$$[\mathbf{G}_{12}]_{pl} = -\overline{[\mathbf{G}_{21}]_{lp}} = -2\int_0^1 \overline{\phi_{1p}}\phi_{2l}\mathrm{d}x_3 - 2\eta\overline{\phi_{1p}(1)}\phi_{2l}(1) \tag{2.21b}$$

$$[\mathbf{G}_{13}]_{pm} = -\overline{[\mathbf{G}_{31}]_{mp}} = -2\hat{d}\eta\overline{\phi_{1p}(1)}\psi_{1m}(1) \tag{2.21c}$$

$$[\mathbf{G}_{24}]_{qn} = -\overline{[\mathbf{G}_{24}]_{nq}} = -2\hat{d}\eta\overline{\phi_{2q}(1)}\psi_{2n}(1) \tag{2.21d}$$

$$[\mathbf{G}_{34}]_{rn} = -\overline{[\mathbf{G}_{43}]_{nr}} = (\nu_{33} - \nu_{11} - \nu_{22} - 2\hat{d}^2\eta)\overline{\psi_{1r}(1)}\psi_{2n}(1) \tag{2.21e}$$

$$[\mathbf{K}] = \begin{bmatrix} [\mathbf{K}_{11}] & \mathbf{0} & \mathbf{0} & [\mathbf{K}_{14}] \\ \mathbf{0} & [\mathbf{K}_{22}] & [\mathbf{K}_{23}] & \mathbf{0} \\ \mathbf{0} & [\mathbf{K}_{32}] & [\mathbf{K}_{33}] & \mathbf{0} \\ [\mathbf{K}_{41}] & \mathbf{0} & \mathbf{0} & [\mathbf{K}_{44}] \end{bmatrix} \tag{2.22a}$$

$$[\mathbf{K}_{11}]_{pk} = \int_0^1 k_{13}\kappa\overline{\phi'_{1p}}\phi'_{1k}\mathrm{d}x_3 \tag{2.22b}$$

$$[\mathbf{K}_{22}]_{ql} = \int_0^1 k_{23}\kappa\overline{\phi'_{2q}}\phi'_{2l}\mathrm{d}x_3 \tag{2.22c}$$

$$[\mathbf{K}_{33}]_{rm} = \int_0^1 \left(k_{23}\kappa\overline{\psi_{1r}}\psi_{1m} + \alpha\overline{\psi'_{1r}}\psi_{1m}\right)\mathrm{d}x_3 \tag{2.22d}$$

$$[\mathbf{K}_{44}]_{sn} = \int_0^1 \left(k_{13}\kappa\overline{\psi_{2s}}\psi_{2n} + \overline{\psi'_{2s}}\psi'_{2n}\right)\mathrm{d}x_3 \tag{2.22e}$$

$$[\mathbf{K}_{14}]_{pn} = \overline{[\mathbf{K}_{41}]_{np}} = -\int_0^1 k_{13}\kappa\overline{\phi'_{1p}}\psi_{2n}\mathrm{d}x_3 \tag{2.22f}$$

$$[\mathbf{K}_{23}]_{qm} = \overline{[\mathbf{K}_{32}]_{mq}} = \int_0^1 k_{23}\kappa\overline{\phi'_{2q}}\psi_{1m}\mathrm{d}x_3 \tag{2.22g}$$

$$[\mathbf{C}] = \begin{bmatrix} [\mathbf{C}_{11}] & \mathbf{0} & \mathbf{0} & [\mathbf{C}_{14}] \\ \mathbf{0} & [\mathbf{C}_{22}] & [\mathbf{C}_{23}] & \mathbf{0} \\ \mathbf{0} & [\mathbf{C}_{32}] & [\mathbf{C}_{33}] & \mathbf{0} \\ [\mathbf{C}_{41}] & \mathbf{0} & \mathbf{0} & [\mathbf{C}_{44}] \end{bmatrix} \tag{2.23a}$$

$$[\mathbf{C}_{11}]_{pk} = \int_0^1 \overline{\phi_{1p}}\phi_{1k}\mathrm{d}x_3 + \eta\overline{\phi_{1p}(1)}\phi_{1k}(1) \tag{2.23b}$$

$$[\mathbf{C}_{22}]_{ql} = \int_0^1 \overline{\phi_{2q}}\phi_{2l}\mathrm{d}x_3 + \eta\overline{\phi_{2q}(1)}\phi_{2l}(1) \tag{2.23c}$$

$$[\mathbf{C}_{33}]_{rm} = -\int_0^1 \alpha\mu\overline{\psi_{1r}}\psi_{1m}\mathrm{d}x_3 + (\nu_{22} - \nu_{33} + \hat{d}^2\eta)\overline{\psi_{1r}(1)}\psi_{1m}(1) \tag{2.23d}$$

$$[\mathbf{C}_{44}]_{sn} = -\int_0^1 \mu\overline{\psi_{2s}}\psi_{2n}\mathrm{d}x_3 + (\nu_{11} - \nu_{33} + \hat{d}^2\eta)\overline{\psi_{2s}(1)}\psi_{2n}(1) \tag{2.23e}$$

$$[\mathbf{C}_{14}]_{pn} = \overline{[\mathbf{C}_{41}]_{np}} = \hat{d}\eta\overline{\phi_{1p}(1)}\psi_{2n}(1) \tag{2.23f}$$

$$[\mathbf{C}_{23}]_{qm} = \overline{[\mathbf{C}_{32}]_{mq}} = -\hat{d}\eta\overline{\phi_{2q}(1)}\psi_{1m}(1) \tag{2.23g}$$

where the prime denotes differentiation with respect to the spatial coordinate, that is, $()' = \mathrm{d}()/\mathrm{d}x_3$. The matrix operators in Eq. (2.19a) have symmetries that stem from the adjointness properties of the corresponding extended operators in Eq. (2.16). The mass, stiffness, and centripetal matrices are Hermitian, that is, $\overline{[\mathbf{M}]}^T = [\mathbf{M}]$, $\overline{[\mathbf{K}]}^T = [\mathbf{K}]$, and $\overline{[\mathbf{C}]}^T = [\mathbf{C}]$. The gyroscopic matrix is skew-Hermitian $\overline{[\mathbf{G}]}^T = -[\mathbf{G}]$. The matrix eigenvalue problem in Eq. (2.19a) is solved using standard numerical methods for the eigenvalues λ and the eigenvectors $\{\mathbf{h}\}$. The continuum translational deformations $u_1(x_3)$ and $u_2(x_3)$ in Eq. (2.18) are calculated from the elements of $\{\mathbf{h}\}$ with the chosen basis functions $\phi_{1k}(x_3)$ and $\phi_{2l}(x_3)$. Similarly, the continuum rotational deformations $\theta_1(x_3)$ and $\theta_2(x_3)$ are calculated from the elements of $\{\mathbf{h}\}$ with $\psi_{1m}(x_3)$ and $\psi_{2n}(x_3)$.

We use orthogonal polynomials as basis functions for discretization. Admissible sets of orthogonal polynomials are easily generated for the current problem. We briefly describe the process and give the first ten polynomials used in A. A benefit of the current problem is that all deformations can use the same set of orthogonal polynomials. Therefore, the set of basis functions needs only to be constructed once and can be used repeatedly to populate the matrices.

The use of orthogonal polynomials permits simple, closed-form expressions for the matrix elements in Eq. (2.19a). These are given in B. The use of the matrix elements in A is preferred to numerically evaluating the elements in integral form. We found slight errors from numerical integration can break the expected matrix symmetries, causing difficulty solving the matrix eigenvalue problem and spurious instabilities. Numerical calculations using 25 basis functions were used to examine high frequency regions where shear deformation effects are prominent. Fewer basis functions are needed if only the first several modes are of interest.

To investigate the importance of shear deformation effects, we quantify the ratio of the shear strain energy to the total strain energy in a vibration mode using

$$\chi = \frac{\int_0^1 \left[k_{13}\kappa(\theta_2 - u_{1,3})^2 + k_{23}\kappa(\theta_1 + u_{2,3})^2\right] \mathrm{d}x_3}{\int_0^1 \left[k_{13}\kappa(\theta_2 - u_{1,3})^2 + k_{23}\kappa(\theta_1 + u_{2,3})^2 + \alpha\theta_{1,3}^2 + \theta_{2,3}^2\right] \mathrm{d}x_3} \tag{2.24}$$

$$\implies \chi = \frac{\overline{\{\mathbf{h}\}}^T [\mathbf{K}_{\text{shear}}] \{\mathbf{h}\}}{\overline{\{\mathbf{h}\}}^T [\mathbf{K}] \{\mathbf{h}\}} \tag{2.25}$$

where $[\mathbf{K}_{\text{shear}}]$ is the stiffness matrix associated with shear deformation effects. It is only those elements in Eq. (2.22a) that contain κ. Larger values of shear strain energy ratio χ in a given vibration mode indicate larger amounts of shear strain in the corresponding deformations. Conversely, small values of shear strain energy ratio indicate the mode is dominated by beam bending.

2.3 Numerical results

This section numerically analyzes the vibration and stability of spinning cantilevered beams with attached rigid bodies. Two systems are considered. The first system consists of a beam with a square tubular cross-section. The rigid body at its tip is a solid cube. This system possesses identical inertia and stiffness properties in the two bending directions. We will refer to this as the symmetric system. The second system consists of a beam with a rectangular tube cross-section and a rigid body that is a solid rectangular prism. With these characteristics, the system has unequal inertia and stiffness properties in the two bending directions. This will be referred to as the asymmetric system. The offset of the rigid body mass center from the end of the beam is taken as one-half of the body's length, which is the case for a solid body with homogeneous density. The geometric parameters of both systems are given in Table 2.1. The corresponding nondimensional parameters for the symmetric system are $\kappa = 201.1069$, $\mu = 0.001876$, $\alpha = 1$, $k_{13} = k_{23} = 0.4355$,

Table 2.1: Dimensional parameters of the symmetric and asymmetric beam-rigid body systems. The beams have tubular cross-sections.

<table>
<tr><th></th><th>Symmetric</th><th>Asymmetric</th></tr>
<tr><td colspan="3">Beam material properties</td></tr>
<tr><td>Elastic modulus, E (GPa)</td><td colspan="2">68.9</td></tr>
<tr><td>Shear modulus, G (GPa)</td><td colspan="2">26</td></tr>
<tr><td>Density, ρ (kg/m^3)</td><td colspan="2">2710</td></tr>
<tr><td colspan="3">Beam geometry</td></tr>
<tr><td>Length, L (mm)</td><td colspan="2">80</td></tr>
<tr><td>Outer width, w_o (mm)</td><td rowspan="2">10.4</td><td>12.5</td></tr>
<tr><td>Outer height, h_o (mm)</td><td>10</td></tr>
<tr><td>Inner side width, w_i (mm)</td><td rowspan="2">6</td><td>8.5</td></tr>
<tr><td>Inner side height, h_i (mm)</td><td>6</td></tr>
<tr><td colspan="3">Rigid body properties</td></tr>
<tr><td>Density, ρ_M (kg/m^3)</td><td colspan="2">2710</td></tr>
<tr><td>Length, L_M (mm)</td><td colspan="2">10</td></tr>
<tr><td>Width, w_M (mm)</td><td rowspan="2">17.1</td><td>20</td></tr>
<tr><td>Height, h_M (mm)</td><td>15</td></tr>
</table>

$\eta = 0.5068$, $v_{11} = v_{22} = 0.00258875$, $v_{33} = 0.00385782$, $\hat{d} = 0.0625$. The asymmetric system has nondimensional parameters $\alpha = 1.4860$, $v_{11} = 0.003299$, $v_{22} = 0.002144$, and $v_{33} = 0.004124$. The remaining nondimensional parameters are the same as the symmetric system.

To accurately capture higher frequency vibrations, 25 basis functions were used for each deformation (i.e., $N_1 = N_2 = M_1 = M_2 = 25$). Hence, all matrices used in Eqs (2.19a) had dimension 100. Fewer basis functions can be used if only the first several modes are of interest. For instance, to accurately capture the first four modes of the beam-rigid body systems with parameters in Table 2.1, only 10 basis functions are needed for each deformation.

2.3.1 Eigenvalue behavior

Figure 2.2(a) shows the real and imaginary parts of the eigenvalues calculated for a wide range of nondimensional rotation speeds. A region showing the first two pairs of modes at speeds below $\hat{\Omega} = 5$ is shown in Fig. 2.2(b). The eigenvalues of the symmetric system are shown in the dashed (red) lines. The natural frequencies are degenerate at zero speed. For non-zero speeds, the natural frequencies split, with one increasing and the other decreasing with increasing rotation speed. This is typical behavior for the eigenvalues of spinning beams with symmetric cross sections [5]. The addition of a rigid body at the tip and the inclusion of shear deformations in the beam do not alter this behavior.

Speeds where one or more eigenvalues vanish are called critical speeds. The critical speeds for the symmetric system in Fig. 2.2 are degenerate. The critical speeds corresponding to the first three modes are $\hat{\Omega}_c = 1.861$, 13.749, and 37.162. The eigenvalues are purely imaginary and stable immediately below and above all critical speeds, indicating that no instability occurs.

The natural frequencies for the asymmetric system (solid (black) lines in Fig. 2.2) are distinct at $\hat{\Omega} = 0$, as expected, because of the differences in the system inertia and stiffness properties in the two bending directions. We note the stationary natural frequencies for the asymmetric beam differ from those of the symmetric beam. This is due to the differences in the rigid body moments of inertia. Because both v_{11} and v_{22} differ between the two systems, none of the stationary system natural frequencies for the asymmetric system are identical to those of the symmetric system. For increasing speed from zero, one eigenvalue increases and the other decreases, similar to the behavior seen for the symmetric system. Eigenvalue veering regions [160–162] occur for the asymmetric system whenever a decreasing eigenvalue comes in close proximately to an increasing eigenvalue. Within veering regions, the eigenvalues have large local curvatures because their directions change abruptly with speed. No veering regions occur between locally increasing and locally decreasing eigenvalues for the symmetric system, making veering a sharp contrasting feature for the asymmetric system.

The asymmetric system has distinct critical speeds due to the differences in the inertia and stiffness properties in the two bending directions. The critical speeds in Fig. 2.2 occur at $\hat{\Omega}_c = 1.86$, 2.2538, 13.6598, 16.1033, 36.8036, and 41.8150. They are denoted by arrows in Fig. 2.2. Like the stationary system natural frequencies, the critical speeds differ between the two systems because of the differences in the mass moments of inertia. We examine the eigenvalue behavior for a range of speeds from $\hat{\Omega} = 35$ to 45, which includes critical speeds at $\hat{\Omega}_{c5} = 36.8036$ and $\hat{\Omega}_{c6} = 41.8150$. Immediately below the critical speed at $\hat{\Omega}_{c5} = 36.8036$, the lowest frequency eigenvalue is purely imaginary and stable. It vanishes at the critical speed when $\hat{\Omega}_{c5} = 36.8036$. Immediately above $\hat{\Omega}_{c5} = 36.8036$, the eigenvalue becomes real-valued, and positive, and experiences divergence instability. The eigenvalue remains real-valued, positive, and unstable for the entire range of speeds between $\hat{\Omega} = 36.8036$ and 41.8150. The eigenvalue again vanishes at the next critical speed when $\hat{\Omega} = \hat{\Omega}_{c6} = 41.8150$. For speeds immediately above this critical speed, the eigenvalue becomes purely imaginary and regains stability. Similar behavior occurs for each pair of critical speeds shown in Fig. 2.2.

Divergence instability occurs due to asymmetry in the system's inertia or stiffness properties. Shear deformation effects are not necessary. Indeed, we have numerically verified that divergence instabilities remain for the case that shear deformation effects are negligible (i.e., $\kappa \to \infty$).

Flutter instability occurs when a complex-valued eigenvalue has a positive real part. The corresponding single-mode free response will have oscillatory deformations that increase in amplitude with each oscillation cycle. The presence of flutter instabilities is another distinguishing feature of the asymmetric system that is not present when the system is symmetric. Regions of flutter instability are denoted by F1-F8 in Fig. 2.2(a). In all cases of flutter instability, a locally decreasing purely imaginary eigenvalue coalesces with a locally increasing purely imaginary eigenvalue. At speeds immediately above this speed, the eigenvalues become complex-valued. One eigenvalue has a positive real part and experiences flutter instability. Flutter instability continues for a range of speeds before the two eigenvalues again coalesce. Immediately above this speed, the eigenvalues become purely imaginary and regain stability.

Eigenvalue veering and flutter instability are features that only occur in asymmetric systems when shear deformation effects are included. We have numerically confirmed that in the case that shear deformation effects are negligible (i.e., when $\kappa \to \infty$) all regions of eigenvalue veering and flutter instability become vanishingly small.

2.3.2 Vibration modes

The vibration modes for gyroscopic systems are generally complex-valued [157,158]. Physically, this represents non-vanishing (and non-180 degree) phase differences between the vibrations associated with different coordinates in the modes. Figure 2.3 shows the symmetric system modal deformations corresponding to eigenvalues $\lambda =$ j0.358 and j3.337 at $\hat{\Omega} = 1.5$ (see Fig. 2.2(b)). The solid (blue) and dashed (red) lines in Fig. 2.3 are the real and imaginary parts of the complex-valued modes, respectively. The modes shown are normalized so that the maximum amplitude of u_1 is 0.5. Both modes resemble the first bending mode for typical stationary beams. As seen in Fig. 2.3, the modal deformations $u_1(x_3)$ and $\theta_2(x_3)$ are real-valued (their imaginary parts vanish). $u_2(x_3)$ and $\theta_1(x_3)$ are purely imaginary (their real parts vanish). The magnitudes of the bending and rotational deformations are identical, that is, $|u_1(x_3)| = |u_2(x_3)|$ and $|\theta_1(x_3)| = |\theta_2(x_3)|$.

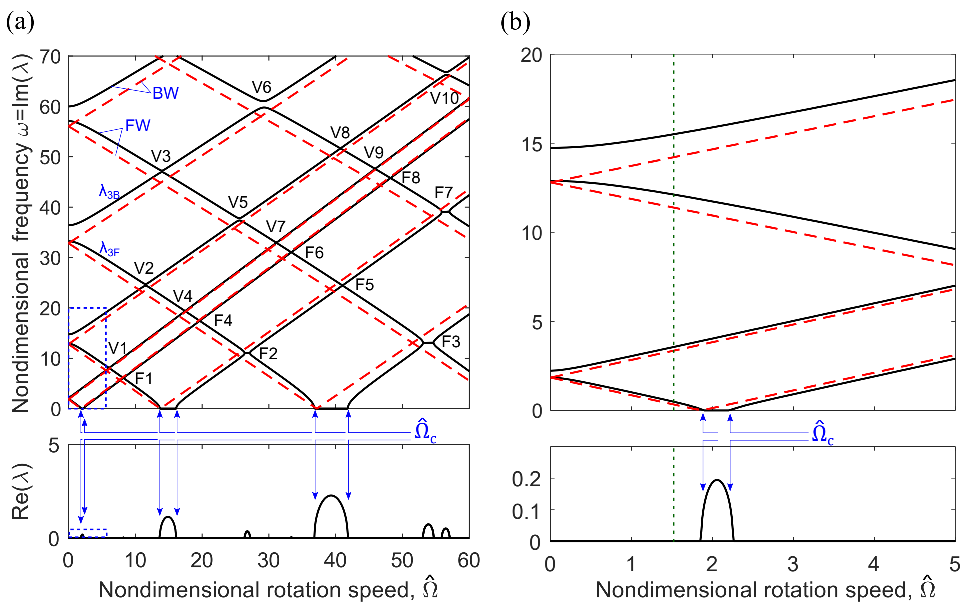

Figure 2.2: (a) Beam-rigid body eigenvalue loci for varying nondimensional rotation speed. (b) The regions shown by the dotted (blue) boxes in (a). The dashed (red) lines are for the symmetric system. The solid (black) lines are for the asymmetric system. The parameters are given in Table 2.1.

The modal deformations have further properties that lead to specific vibratory features in single-mode response. For the mode corresponding to $\lambda = \mathrm{j}0.358$ in Figs. 2.3(a,c), the deformations can be written as $u_1(x_3) = \hat{u}(x_3)$ and $u_2(x_3) = -\mathrm{j}\hat{u}(x_3)$. Hence, the deformations u_2 have a 90 degree ($\pi/2$ radians) phase lag with the deformations u_1 at all material points along the span. The rotational deformations can similarly be written as $\theta_2(x_3) = \hat{\theta}(x_3)$ and $\theta_1(x_3) = \mathrm{j}\hat{\theta}(x_3)$, indicating θ_1 leads θ_2 by 90 degrees ($\pi/2$ radians). The single-mode response corresponding to Eq. (2.15) is calculated from $\mathbf{h}e^{\lambda t} + cc$, where cc denotes the complex conjugate of all preceding terms. From the first element of $\mathbf{h}$, the bending deformation $u_1(x_3,t) = \hat{u}(x_3)e^{\mathrm{j}\omega t} + cc = 2\hat{u}(x_3)\cos\omega t$. The second element gives $u_2(x_3,t) = -\mathrm{j}\hat{u}(x_3)e^{\mathrm{j}\omega t} + cc = 2\hat{u}(x_3)\sin\omega t$. These results show that material particles located along the beam span have perfectly circular motion with radius $2|\hat{u}(x_3)|$ about the undeformed position. The material particles move in the direction of rotation. The frequency of revolution is the natural frequency $\omega = \mathrm{Im}(\lambda)$ of the corresponding mode. We will refer to these as forward orbit modes.

By a similar analysis, the mode corresponding to $\lambda = \mathrm{j}3.337$ with deformations in Figs. 2.3(b,d) correspond to perfectly circular orbits about the undeformed position that move in the direction opposite of the rotation. Indeed, the modal bending deformations can be written $u_1(x_3) = \hat{u}(x_3)$ and $u_2(x_3) = \mathrm{j}\hat{u}(x_3)$. In single-mode response $u_1(x_3,t) = \hat{u}(x_3)e^{\mathrm{j}\omega t} + cc = 2\hat{u}(x_3)\cos\omega t$, like for forward orbiting modes. The other bending deformation is now $u_2(x_3,t) = \mathrm{j}\hat{u}(x_3)e^{\mathrm{j}\omega t} + cc = -2\hat{u}(x_3)\sin\omega t$. The expressions for the rotational deformations can be determined similarly. These confirm the circular geometry of the motion and its backward direction of travel (with respect to the direction of rotation).

The mathematical structure leading to forward and backward orbiting deformations in single-mode response applies to all pairs of symmetric system eigenvalues shown in Fig. 2. All decreasing eigenvalues correspond to modes that have perfectly circular forward orbits at all material points along the span. Similarly, all increasing eigenvalues with increasing speed correspond to backward orbiting deformations with perfectly circular orbits. These modal properties are consistent with slender beams without shear deformation effects [5]. Forward and backward orbit vibrations also occur in systems with cyclic symmetry [163–166]. Closely related are forward and backward wave vibrations that occur in axisymmetric systems like spinning disks [150, 167–169] and rings [170–175], for example.

The modal shear strains along the beam span are shown in Figs. 2.3(e) and 2.3(f). These are calculated from $\varepsilon_{13} = \hat{u}_1' - \hat{\theta}_2$ and $\varepsilon_{23} = \hat{u}_2' + \hat{\theta}_1$. Because of the properties of the deformations, the bending strain ε_{13} is real-valued and ε_{23} is purely imaginary. As seen in the figures, the shear strains are small for the entire beam span in both the forward (Fig. 2.3(e)) and backward (Fig. 2.3(f)) orbit modes. The maximum shear strain is just $\varepsilon_{13} = 0.0184$ ($\varepsilon_{13} = 0.018$) for the forward (backward) orbit mode in Fig. 2.3(e) (Fig. 2.3(f)). The shear strains do not vanish at the beam tip because of the presence of a rigid body. In systems without a rigid body, the shear strains vanish at the beam tip. Because the shear strains are small, this mode would be accurately predicted using models that exclude shear deformation effects (e.g., an Euler-Bernoulli beam model). The shear strains increase for higher modes (not shown).

Figure 2.4 shows example modal deformations for two modes from the asymmetric system at $\hat{\Omega} = 1.5$. The modal deformations shown in Figs. 2.4(a,c) correspond to the eigenvalue $\lambda = \mathrm{j}12.138$ (see Fig. 2.2(b)). The modal deformations corresponding to the eigenvalue $\lambda = \mathrm{j}15.491$ are shown in Figs. 2.4(b,d). The modes are normalized so that the maximum deformation is 0.5. Like for the symmetric system modes in Fig. 2.3, the modes for the asymmetric system in Fig. 2.4 have real-valued $u_1(x_3)$ and $\theta_2(x_3)$ and purely imaginary $u_2(x_3)$ and $\theta_1(x_3)$. Additionally, the bending deformations u_2 lag those for u_1 by 90 degrees ($\pi/2$ radians) for the majority of the beam span in Fig. 2.4(a). u_2 leads u_1 by 90

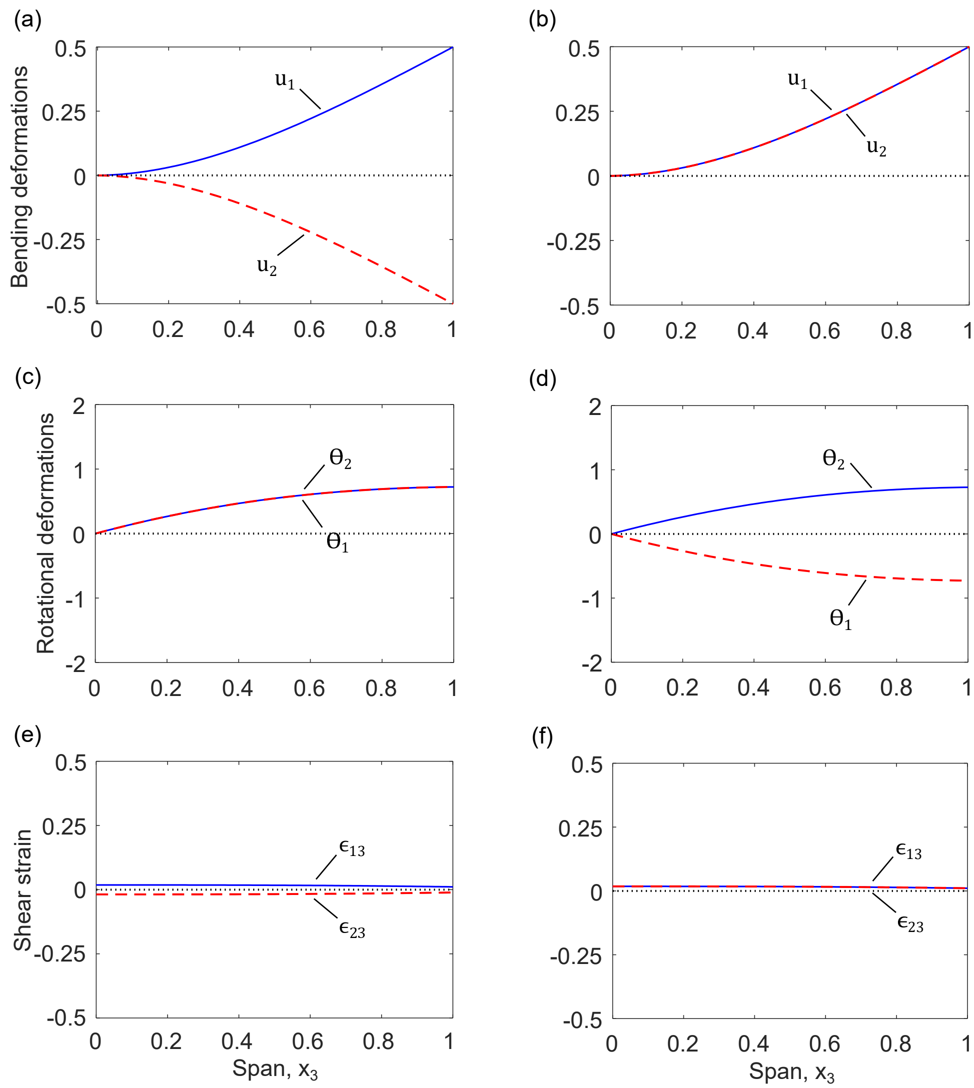

Figure 2.3: Modal deformations corresponding to the first pair of eigenvalues for the symmetric beam-rigid body system at $\hat{\Omega} = 1.5$. The modal bending deformations, rotational deformations, and shear strains are shown in (a, c, e) and (b, d, f) for the forward orbit and backward orbit modes, respectively. The solid (blue) and dashed (red) lines are the real and imaginary parts of the complex-valued quantities. The dotted (black) lines denote vanishing quantities.

degrees ($\pi/2$ radians) for the majority of the span in Fig. 2.4(b). These phase differences are responsible for the forward and backward orbit vibrations in single-mode response. The modes in Fig. 2.4 have different magnitudes of bending and rotational deformations in the two bending directions, however. Hence, the single-mode free vibration will have material points that travel in elliptical, not circular, orbits in the direction of rotation (forward orbits) and the direction opposite of rotation (backward orbits). The sizes of the elliptical paths traveled by material points vary along the span. The semi-major and semi-minor axes always lie along u_1 and u_2.

Away from veering and instability regions, the vibration modes have predominantly forward orbit or backward orbit form, like in Fig. 2.4 for the second pair of modes at $\hat{\Omega} = 1.5$. The entire span does not generally have only forward or backward orbits, however. Indeed, small regions of the beam span generally near nodes have material points that are often in the opposite direction. We demonstrate this behavior using the deformations shown in Fig. 2.4(a). The nodal point where u_1 vanishes occurs at $x_3 = 0.9708$. u_2 vanishes at $x_3 = 0.9688$, however. Therefore, within the small region from $x_3 = 0.9688$ to 0.9708 the deformation u_2 leads u_1 and the resulting vibration has material points with backward orbits. We note the remainder of the span (i.e., from $x_3 = 0$ to 0.9688 and from 0.9708 to unity) has material points that have forward orbits. The regions where the orbit direction changes increase with increasing mode. It always remains small compared to the beam span. For example, the first nodal points for the fifth forward mode are $x_3 = 0.2972$ for u_1 and 0.3032 for u_2 (not shown). The behavior described is driven by shear deformation effects and the attached rigid body at the beam tip. For thin cantilevered beams without rigid bodies at their tip, the nodal points of u_1 are identical to those for u_2, and the vibration modes have one orbit direction along the entire span.

The modal shear strains for the asymmetric system are shown in Figs. 2.4(e,f). As can seen in these figures, ε_{13} is larger for the forward orbit mode in Fig. 2.4(e), whereas ε_{23} has larger magnitude for the backward orbit mode in Fig. 2.4(f). These larger shear strains correlate to generally larger deformations within the beam span.

The modal shear strain energy ratios, calculated from Eq. (2.25), for the symmetric system are shown by the dashed (red) lines in Fig. 2.5. For the stationary system at $\hat{\Omega} = 0$, the strain energy ratios for each mode within a pair are identical. The stationary system shear strain energy ratios increase with increasing mode pair. In the first pair of modes, the shear strain energy ratio is just 0.0322. It increases to 0.1914 for the second pair of modes. The shear strain energy ratio increases further to 0.3259 for the fourth pair of modes, which is the largest pair of modes shown in Fig. 2.5. These larger strain energy ratios demonstrate the importance of shear deformation effects for the higher frequency modes in this system. For increasing speed from zero, the shear strain energy ratio increases (decreases) nearly linearly with increasing speed for forward orbit (backward orbit) modes. For each pair, the shear strain energy ratio for the forward orbit mode is always larger than that for the backward orbit mode. At higher speeds, lower forward orbit modes may have larger χ than higher backward orbit modes from different pairs. We consider the speed $\hat{\Omega} = 40$ as an example. At this speed, the second forward orbit mode has $\chi = 0.2991$, which is larger than the third backward orbit mode with $\chi = 0.2615$.

The shear strain energy ratios for the asymmetric system (solid (black) lines in Fig. 2.5) have features that distinguish them from shear strain energy ratios for the symmetric system. All χ are distinct for vanishing rotation speed due to the disruption of symmetry from differences in inertia and stiffness properties in the two bending directions. In each pair of shear strain energy ratio curves, the larger and smaller values correspond to the backward and forward orbit modes, respectively. Similar to the symmetric system, the

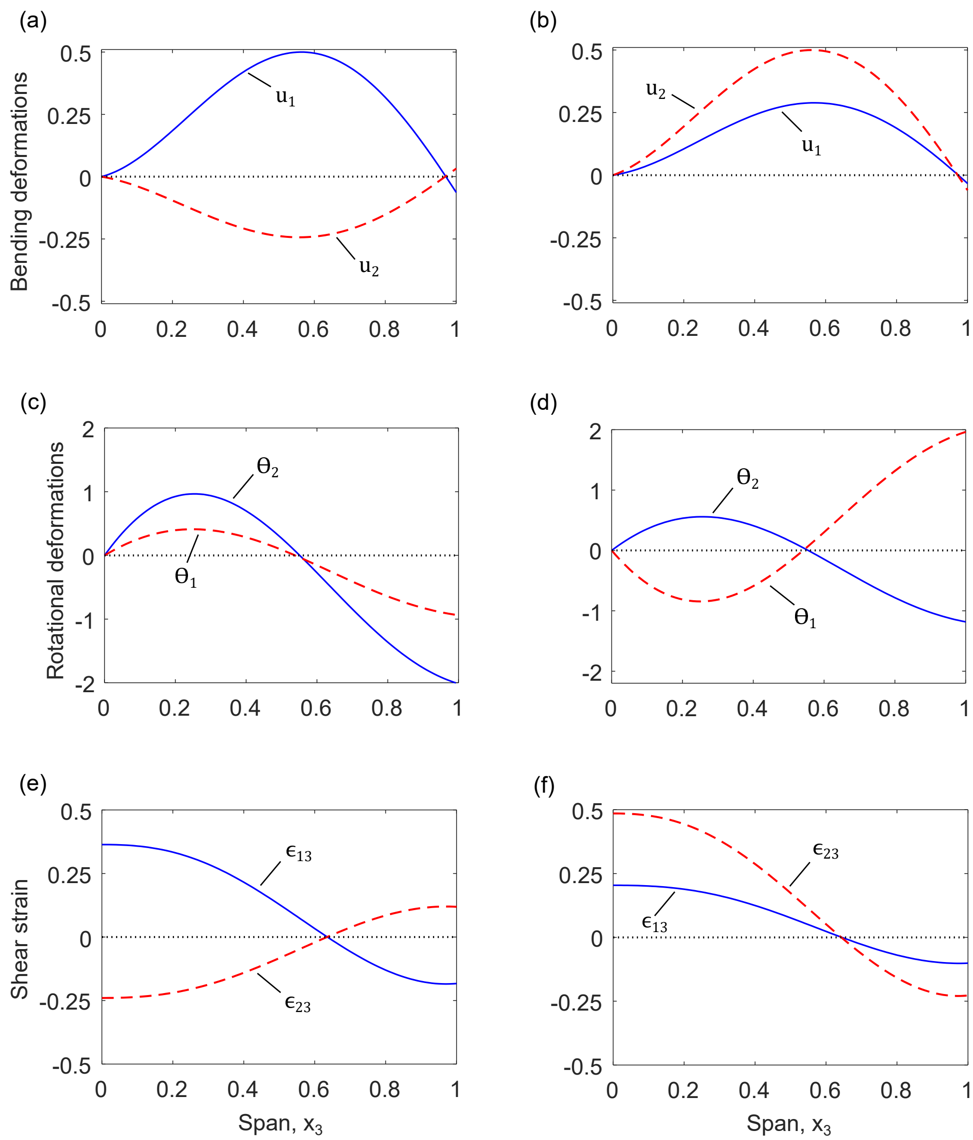

Figure 2.4: Modal deformations corresponding to the second pair of eigenvalues for the asymmetric beam-rigid body system at $\hat{\Omega} = 1.5$. The modal bending deformations, rotational deformations, and shear strains are shown in (a, c, e) and (b, d, f) for the forward orbit and backward orbit modes, respectively. The solid (blue) and dashed (red) lines are the real and imaginary parts of the complex-valued quantities. The dotted (black) lines denote vanishing quantities.

shear strain energy ratio for the forward (backward) orbit mode increases (decreases) for increasing speed from $\hat{\Omega} = 0$. The shear strain energy ratios are equal at a sufficiently high rotation speed. For further increases in rotation speed, the shear strain energy ratio for the forward orbit mode is larger than the corresponding backward orbit mode. To illustrate these behaviors, we consider the shear strain energy ratio changes of the second pair of modes for varying rotation speeds. At $\hat{\Omega} = 0$, the shear strain energy ratio for the forward and backward orbit modes are 0.194 and 0.254, respectively. The forward (backward) orbit mode has $\chi = 0.212$ (0.239) at $\hat{\Omega} = 1.5$, where the modal deformations are shown in Fig. 2.4. The forward and backward orbit modes have nearly identical shear strain energy ratios near $\hat{\Omega} = 3.45$. For speeds immediately above $\hat{\Omega} = 3.45$, the forward orbit mode shear strain energy ratio is larger than that for the backward orbit mode. At higher rotation speeds, sharp local changes in the shear strain energy ratio occur. Comparing to Fig. 2.2 reveals these regions correspond to locations where the eigenvalues experience veering or flutter instability. These behaviors will be explored further later in the paper.

Relatively sharp changes also occur locally when the forward orbit mode eigenvalues approach critical speeds. Immediately before the critical speed, the shear strain energy ratios locally decrease with increasing speed. These decreases increase as the speed approaches the critical speed. Immediately above the critical speed, the shear strain energy ratio increases with increasing speed. It continues to increase, nearly linearly, until the speed approaches the next critical speed. At this point, the shear strain energy ratio again experiences local decreases with increasing speed. The shear strain energy ratio increases monotonically with further increasing speeds, following a trajectory similar to the one it did prior to the corresponding eigenvalue experiencing critical speeds and divergence instability.

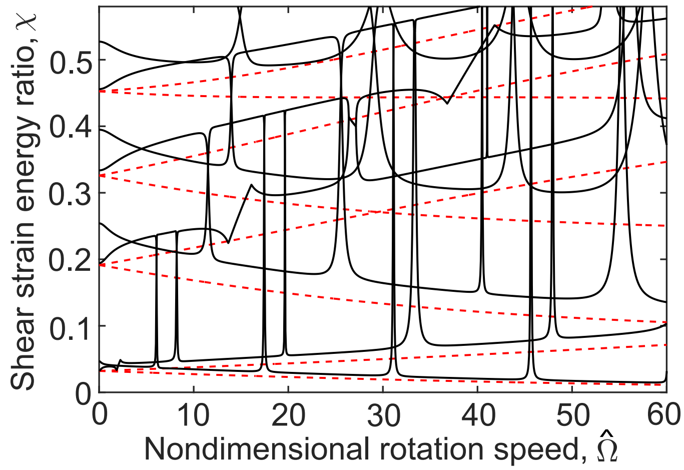

Figure 2.5: Modal shear strain energy ratio for varying nondimensional rotation speed. The dashed (red) and solid (black) lines are for the symmetric and asymmetric systems, respectively. The parameters are given in Table 2.1.

2.3.3 Eigenvalue veering

Eigenvalue veering is accompanied by strong coupling of the two corresponding vibration modes within the veering region and an exchange of the modal properties after the veering region [160–162]. This section analyzes the modal coupling within veering regions for the asymmetric system. Eigenvalue veering does not occur for the symmetric system. All eigenvalue loci cross, without interaction, for symmetric systems (see the dashed (red) lines in Fig. 2.2).

We consider the veering interaction V5 indicated in Fig. 2.2 as an example. Figure 2.6(a) shows the large local curvatures of the eigenvalue loci within the veering region. In this region, the locally increasing eigenvalue of the second backward orbit mode interacts with the locally decreasing eigenvalue of the fourth forward orbit mode. Figures 2.6(b) and (f) show the vibration modes before veering at $\hat{\Omega} = 23$ (denoted by the leftmost circle markers in Fig. 2.6(a)). Only the bending deformations are shown for brevity; rotational deformations have similar features and are not shown. Within the veering region these modes couple. This is shown in Fig. 2.6(c) for the upper locus and Fig. 2.6(g) for the lower locus at $\hat{\Omega} = 25.6$ (the middle circle markers in Fig. 2.6(a)). The strong modal coupling leads to the beam having both forward and backward orbits within its span. To distinguish between the two orbits, we shade regions of the beam span where forward orbits occur in Figs. 2.6(c,g). In unshaded regions, the material points on the beam have backward orbits. For this veering interaction, the modes have two regions where forward orbits occur and one region where backward orbits occur. These regions differ in length between the two modes. For the mode corresponding to the upper locus in Fig. 6(c), forward orbits occur from $0 < x_3 < 0.228$ and $0.928 < x_3 < 1$. On the lower locus for the mode shown in Fig. 6(g), the forward orbits occur from $0 < x_3 < 0.256$ and $0.871 < x_3 < 1$. After the veering region, the coupling between modes no longer occurs and the modal properties are exchanged. Specifically, the upper locus now corresponds to the second backward orbit mode (Fig. 2.6(d)), and the lower locus corresponds to the fourth forward orbit mode (Fig. 2.6(h)).

The coupling between the two interacting modes, with both forward and backward orbits occurring simultaneously along the span, is responsible for the sharp changes in the shear strain energy ratio shown in Fig. 2.6(e). Before the veering region, modest changes in χ with increasing speed are observed. At $\hat{\Omega} = 23$, the second backward orbit (fourth forward orbit) mode has 0.18 (0.53) shear strain energy ratio. When the speed is near $\hat{\Omega} = 25.6$ large local changes in the shear strain energy ratio occur. The shear strain energy ratio for the fourth forward orbit mode decreases, and that for the second backward orbit mode increases. Beyond $\hat{\Omega} = 28$ where the veering region ends, the shear strain energy ratio for the fourth forward orbit mode is 0.54, which is near the value it had prior to the veering interaction. Similarly, the second backward orbit mode has 0.17 shear strain energy ratio at $\hat{\Omega} = 28$, which is near its pre-veering value.

The behavior shown in Fig. 2.6 is representative of the other veering regions indicated in Fig. 2.2. The forward participating mode always corresponds to higher mode numbers compared to the backward participating mode. Outside veering regions, the modes have either forward or backward orbiting deformations throughout the entire span. Within veering regions where the two interacting modes couple, the beam has a mixture of both forward and backward orbiting deformations within the span. The number of forward orbit and backward orbit regions within the beam span is not related to the modes that interact. For instance, greater numbers of orbit transitions within the beam span occur for V3, V6, and V7, while the numbers are fewer for V1, V8, and V9. However, the higher modes generally have larger numbers of orbit transitions. Within the veering regions, most modes have forward orbits at the beginning of the beam span. Furthermore, the region of backward orbits is generally larger than that of forward orbits.

Eigenvalue veering for spinning cantilevered beams with attached rigid bodies at their tip is a unique behavior that occurs because of shear deformation effects. We have numerically verified that the asymmetric system has no eigenvalue veering when shear deformation effects are negligible (i.e. when $\kappa \to \infty$). For models that exclude shear deformations, all eigenvalues cross without interaction as the rotation speed varies. In the absence of shear deformation effects, all modes have purely forward or backward orbits within the beam span.

2.3.4 High-speed instability

This section builds on the instability features observed from the asymmetric system's eigenvalues shown in Fig. 2.2 and discussed in Section 2.3.1. A focus is on the changes in stability and types of instability that occur as the system parameters are varied. In some

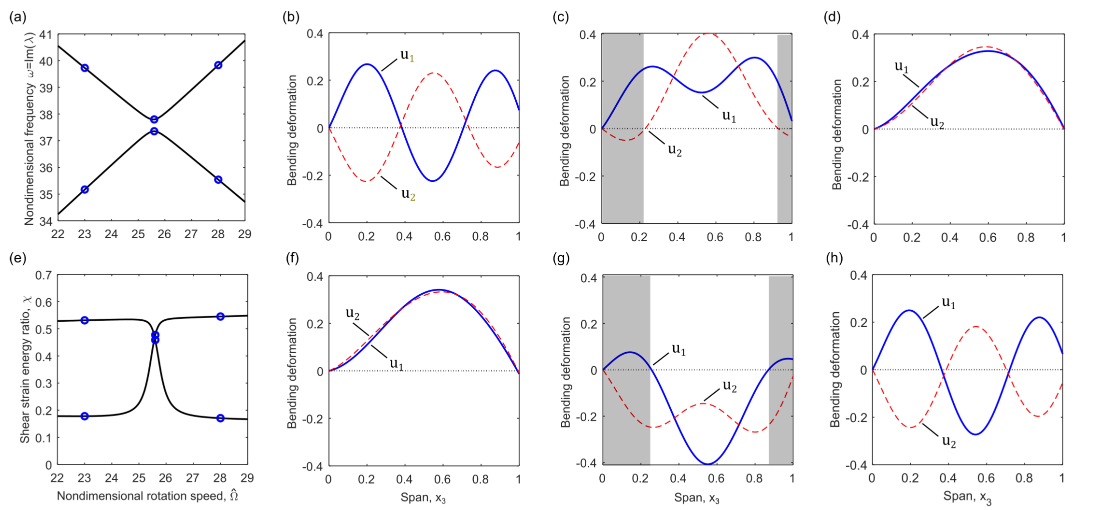

Figure 2.6: (a) Eigenvalue loci for varying speed near the veering interaction V5 in Fig. 2.2. (b-d) Modal bending deformations of the upper locus before, within, and after the veering region, respectively. (f-h) Modal bending deformations of the lower locus before, during, and after the veering region, respectively. (e) Shear strain energy ratio for the modes corresponding to the two interacting eigenvalues in (a). In (b-d) and (f-h) the solid (blue) and dashed (red) lines are the real and imaginary parts of the complex-valued deformations, respectively. The dotted (black) lines denote vanishing bending deformations. The grayed regions in (c) and (g) denote forward orbit vibrations.

cases, large parameter values are included to demonstrate the overall eigenvalue behavior of the system.

Figure 2.7 shows the modal behavior of the unstable eigenvalue within the flutter instability region F7 in Fig. 2.2. A zoomed region of the eigenvalue loci within F7 is shown in Fig. 2.7(a). Prior to experiencing flutter instability the two eigenvalues correspond to the fifth forward orbit mode (Fig. 2.7(b)) and the second backward orbit mode (Fig. 2.7(f)). The two eigenvalues coalesce at the speed $\hat{\Omega} = 55.6$. Immediately above $\hat{\Omega} = 55.6$ one eigenvalue becomes complex-valued with a positive real part and experiences flutter instability. The two eigenvalues coalesce again at $\hat{\Omega} = 56.7$. Stability is regained above $\hat{\Omega} = 56.7$, with the eigenvalues following paths similar to those prior to flutter instability.

Figure 2.7(e) shows the shear strain energy ratio corresponding to the eigenvalues in Fig. 2.7(a). Sharp local changes occur for the two interacting modes as the speed approaches $\hat{\Omega} = 55.6$. The shear strain energy ratio for the fifth forward orbit mode decreases from $\chi = 0.67$ at $\hat{\Omega} = 54$ to $\chi = 0.6352$ at $\hat{\Omega} = 55.9$. For the second backward orbit mode, it increases from 0.41 to 0.6352 at these speeds. The shear strain energy ratio is nearly constant with speed within the flutter instability region from $\hat{\Omega} = 55.6$ to 56.7. Sharp changes in shear strain energy return as the speed departs from $\hat{\Omega} = 56.7$.

Within the unstable region, the modal properties observed for the stable eigenvalues no longer hold. The bending deformations u_1 corresponding to the unstable eigenvalue at $\hat{\Omega} = 56$ are shown in Fig. 2.7(c). The u_2 deformations are the complex conjugate of those for u_1 in Fig. 2.7(c) and are not shown. The rotational deformations have similar behavior to the bending deformations and are not shown. Notably, the deformations u_1, and those for u_2 that are not shown, are complex-valued. Because the phase differences vary along the span and generally differ from $\pm\pi/2$, the forward and backward orbit nature of the single-mode response is lost within flutter instability regions. Indeed, the pathway to large oscillations

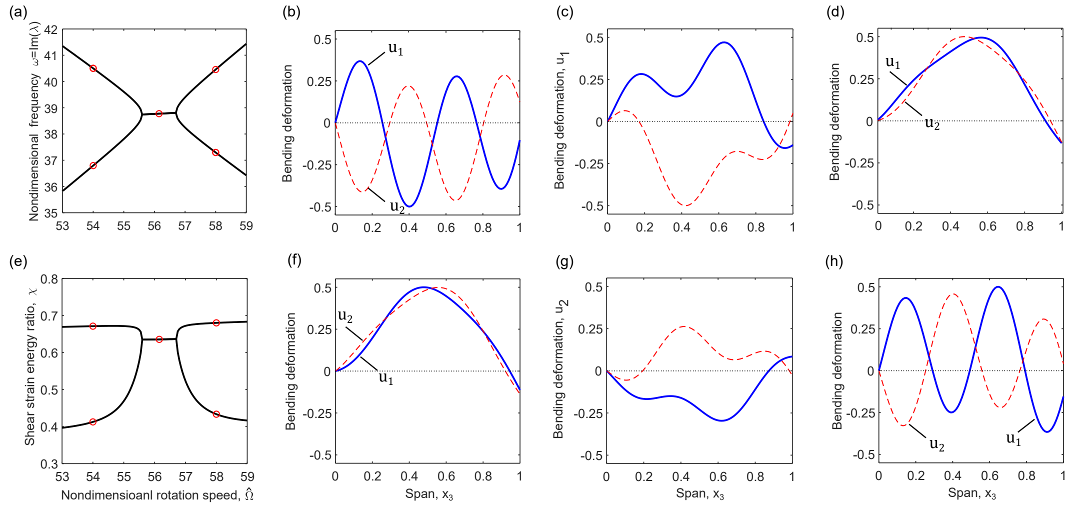

Figure 2.7: (a) Eigenvalue loci for varying speed near the flutter instability region F7 in Fig. 2.2. (b-d) Modal bending deformations of the upper locus before, within, and after the flutter instability region, respectively. (f-h) Modal bending deformations of the lower locus before, during, and after the flutter instability region, respectively. (e) Shear strain energy ratio for the modes corresponding to the two interacting eigenvalues in the flutter region. In (b-d) and (f-h) the solid (blue) and dashed (red) lines are the real and imaginary parts of the complex-valued deformations, respectively. The dotted (black) lines denote vanishing bending deformations.

in the system will not consist of purely forward or purely backward orbits that increase in amplitude with each oscillation cycle. The modal deformations u_2 corresponding to the stable complex-valued eigenvalue are shown in Fig. 2.7(g). The modal deformations of u_1 in the stable mode are not shown because they are the complex-conjugate of u_2. As seen in Figs. 2.7(d) and 2.7(h), the forward and backward orbit modal structure returns along with the eigenvalue stability but with characteristics exchanged. The behavior shown in Fig. 2.7 for the region F7 is representative of the other flutter regions indicated in Fig. 2.2.

Figure 2.8 shows the phase differences for the stable and unstable eigenvalues within the flutter bandwidth F7. The phase difference of the eigenvalues inside the divergence bandwidth varies from $-\pi$ to π rather than experiencing only $\pm\pi/2$. Nevertheless, the

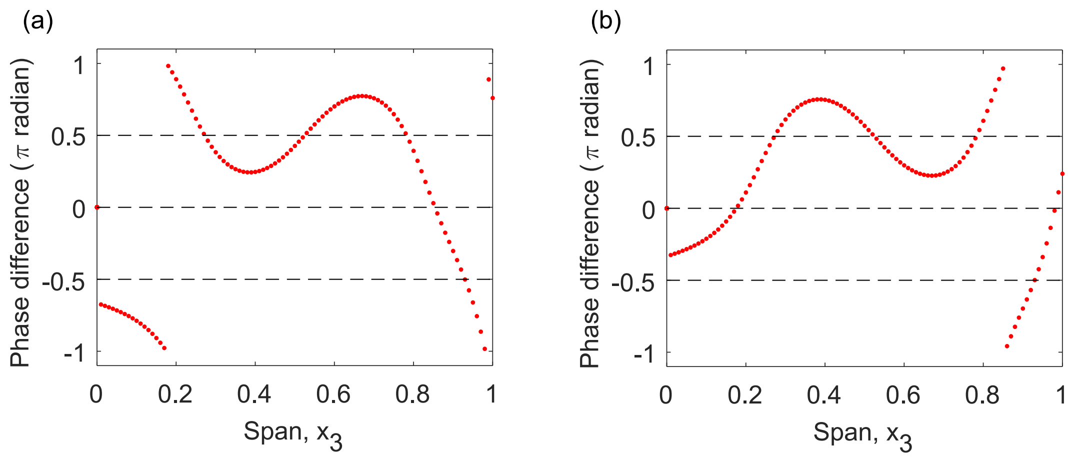

Figure 2.8: Modal phase difference of eigenvalues within the flutter instability bandwidth F7. (a) Stable eigenvalue, (d) Unstable eigenvalue.

summation of the phase difference of the stable and unstable eigenvalues is equal to $\pm\pi$ due to their complex-conjugate relation.

Modal orbits for stable and unstable eigenvalues within the flutter bandwidth F7 at the beam span sections $x = 1/3, 2/3$, and 1 are shown in Fig. 2.9. Figs. 2.9 (a-c) illustrate the decreasing modal orbits for the stable eigenvalue. Figs. 2.9 (d-f) illustrate the increasing modal orbits for the unstable eigenvalue. The orbit shape in the flutter bandwidth is an ellipse, in which the direction of its major axis deviates from the normal cross-section axes e_1 and e_2. This deviation is associated with the phase differences other than $\pm\pi/2$ Their directions also vary across the beam span. For phase differences between 0 to π, the orbits spin clockwise, whereas they spin counter-clockwise for phase differences between 0 to $-\pi$.

Figure 2.10 shows the impact of the beam's input parameters on the high-speed stability of the beam-rigid body system. The rigid body at the tip has parameters given by the asymmetric system in Table 2.1. Figure 2.10(a) shows the beam-rigid body system instabilities for varying ratio of cross-sectional moments of inertia $\alpha = I_{22}/I_{11}$. The solid (black) lines denote critical speeds, which are calculated from Eq. (2.19a) with $\lambda \to 0$. The markers are speeds where divergence (circle (red) markers) and flutter (dot (blue) markers)

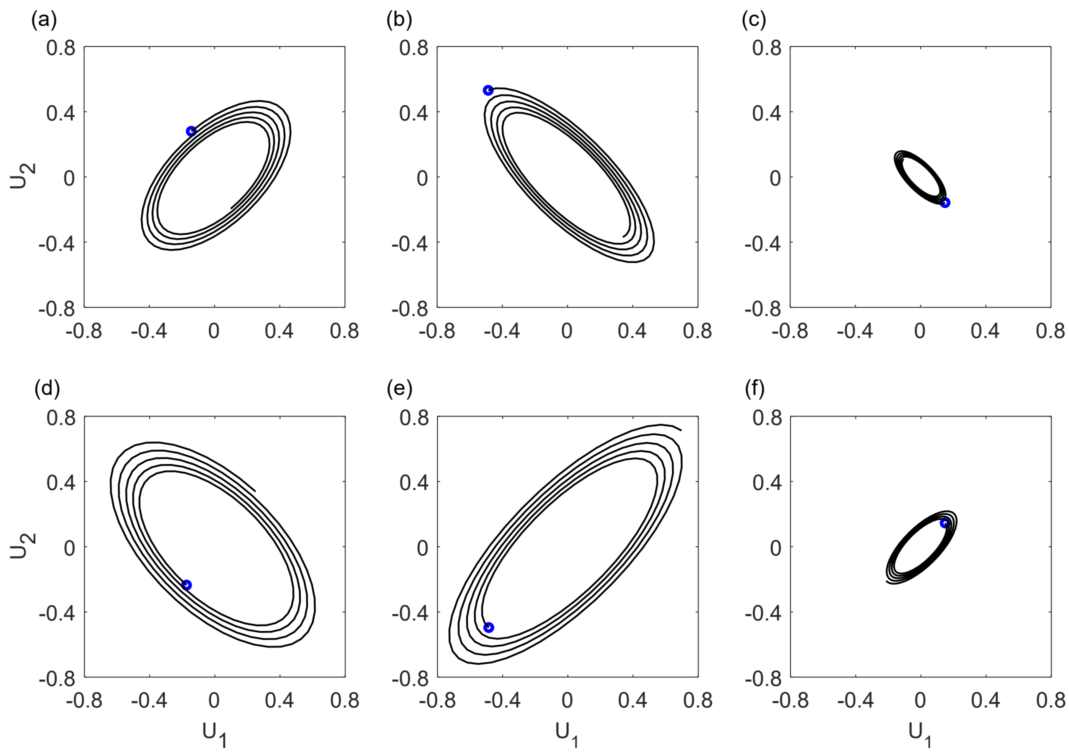

Figure 2.9: Modal orbits of flutter eigenvalues at some beam span sections for the flutter region F7. (a-c) Stable eigenvalues at $x = 1/3, 2/3$, and 1, (d-f) Unstable eigenvalues at $x = 1/3, 2/3$, and 1. Blue circles denote initial points.

instability occur, as determined from natural frequency-speed diagrams like in Fig. 2.2. Even for $\alpha = 1$ the system is asymmetric because $J_{11} \neq J_{22}$, so small regions of instability still exist. For non-unity α the critical speeds separate further, with one critical speed increasing and the other remaining unchanged with increasing α. Between each pair of critical speeds is a region of divergence instability. Increasing the cross-section ratio α increases the speed bandwidths of divergence instability. The divergence instability bandwidths are most sensitive to changes in α for $\alpha < 4$; more gradual changes occur for $\alpha > 4$. The regions of flutter instability increase monotonically in speed with increasing α.

Figure 2.10(b) shows the high-speed instability behavior for varying ratio of shear stiffness to bending stiffness $\kappa = GAL^2/EI_{11}$. The speed range of divergence instability increases with increasing κ. The speed bandwidths of flutter instability are less sensitive to increases in κ within the range shown. For the case that the shear deformation effects are negligible with $\kappa \to \infty$, all regions of flutter instability vanish and all regions of divergence instability are identical to those for slender beams with rotary inertia.

Variations in the ratio of rotary inertia to the transverse inertia $\mu = \rho I_{11}/\rho AL^2 = I_{11}/AL^2$ do not significantly change the locations and speed bandwidths of instabilities and critical speeds. These are not included in Fig. 2.10.

The effect of the rigid body mass $\eta = M/\rho AL$ on the high-speed instability behavior is shown in Fig. 2.11(a). Increases in η monotonically decrease the critical speeds, as seen in the solid (black) lines. The regions of divergence instability (circle (red) markers) change modestly with η. The regions of flutter instability (dot (blue) markers) also decrease in speed but remain of similar bandwidth for increasing η.

Increases in the mass offset parameter $\hat{d}$ (not shown) lead to monotonic decreases in the critical speeds. The regions of divergence and flutter stability decrease to lower speeds

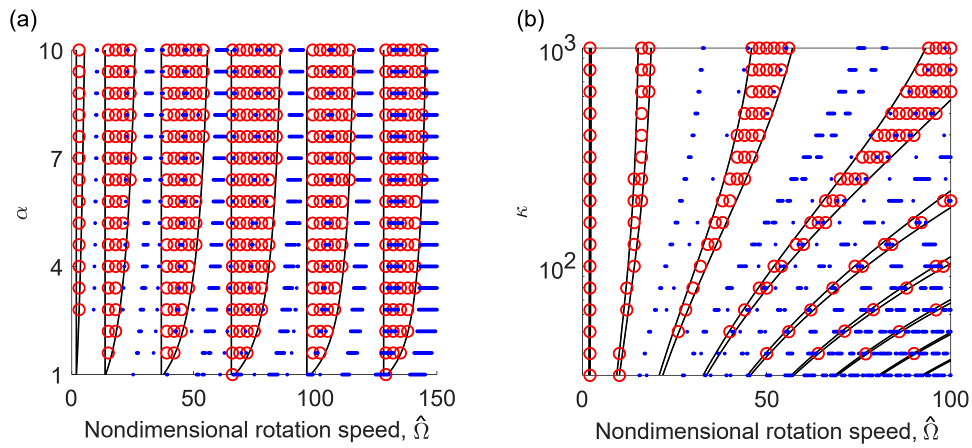

Figure 2.10: High-speed instability behavior for varying (a) cross-section ratio α and (b) ratio of shear stiffness to bending stiffness κ. The solid (black) lines are critical speeds. The circle (red) and dot (blue) markers denote divergence and flutter instability, respectively. Except for the varying parameters, the system has properties given in Table 2.1 for the asymmetric system.

with increases in $\hat{d}$. The unstable speed bandwidths are largely unchanged with changes in $\hat{d}$.

The changes in high-speed stability with varying mass moment of inertia v_{11} are shown in Fig. 2.11(b). Increasing v_{11} decreases one critical speed of each critical speed pair; the other critical speed remains unchanged with increases in v_{11}. The unchanging critical speeds include $\hat{\Omega}_c = 16.10$, 41.82, and 71.98. The speed bandwidths of divergence instability increase with increasing v_{11} (circle (red) markers). Below $v_{11} = 0.008$, the critical speeds separate regions of stability from divergence instability. For mass moments of inertia larger than $v_{11} = 0.008$, however, the regions of divergence instability extend beyond the critical speeds. Increasing v_{11} generally decreases the speed region where flutter instability occurs and increases its speed bandwidth. Some new, small speed bandwidth regions of flutter instability emerge at larger v_{11}. Flutter instability regions occur within divergence instability regions for larger v_{11}.

Changes in the high-speed stability behavior with varying ν_{22} are shown in Fig. 2.11(c). A notable feature is the vanishing of certain divergence instability regions corresponding to values of ν_{22} where the critical speeds are degenerate. Indeed, the critical speeds $\hat{\Omega}_c = 13.66$, 36.80, and 65.55 remain unchanged with changes in ν_{22}. The other critical speeds corresponding to each pair decrease monotonically with increasing ν_{22}. We consider the second pair of critical speeds as an example. The region of divergence instability vanishes for $\nu_{22} = 0.0145$, where the degenerate critical speeds are $\hat{\Omega}_c = 13.66$. Similar behavior occurs for the third and fourth regions of divergence instability when $\nu_{22} = 0.0081$ ($\hat{\Omega}_c = 36.80$) and 0.0060 ($\hat{\Omega}_c = 65.55$), respectively. The values of ν_{22} where the critical speeds become degenerate decrease with increasing speeds. For increasing ν_{22} beyond these values, the regions of divergence instability re-emerge, and the speed bandwidth increases. Some flutter instability regions show similar decreasing-to-increasing speed bandwidths as ν_{22} increases.

The parametric studies in Fig. 2.11 also reveal atypical instability behaviors at high speeds. Before investigating them, we briefly review the typical eigenvalue behavior during divergence and flutter instability. Typical divergence instability occurs when a purely imaginary eigenvalue vanishes at a critical speed, and then becomes real-valued and positive for speeds immediately above the critical speed. The eigenvalue generally regains stability across the very next critical speed when the real and positive eigenvalue becomes purely imaginary again. All regions of divergence instability shown in Fig. 2.2 follow this typical behavior. Typical flutter instability occurs when two purely imaginary eigenvalues coalesce as the rotation speed increases. For speeds immediately above that where coalescence occurs, the eigenvalues become complex-valued. One eigenvalue has a positive real part and experiences flutter instability. The eigenvalues coalesce again at some later speed. The formerly complex-valued eigenvalues then become purely imaginary again across this speed.

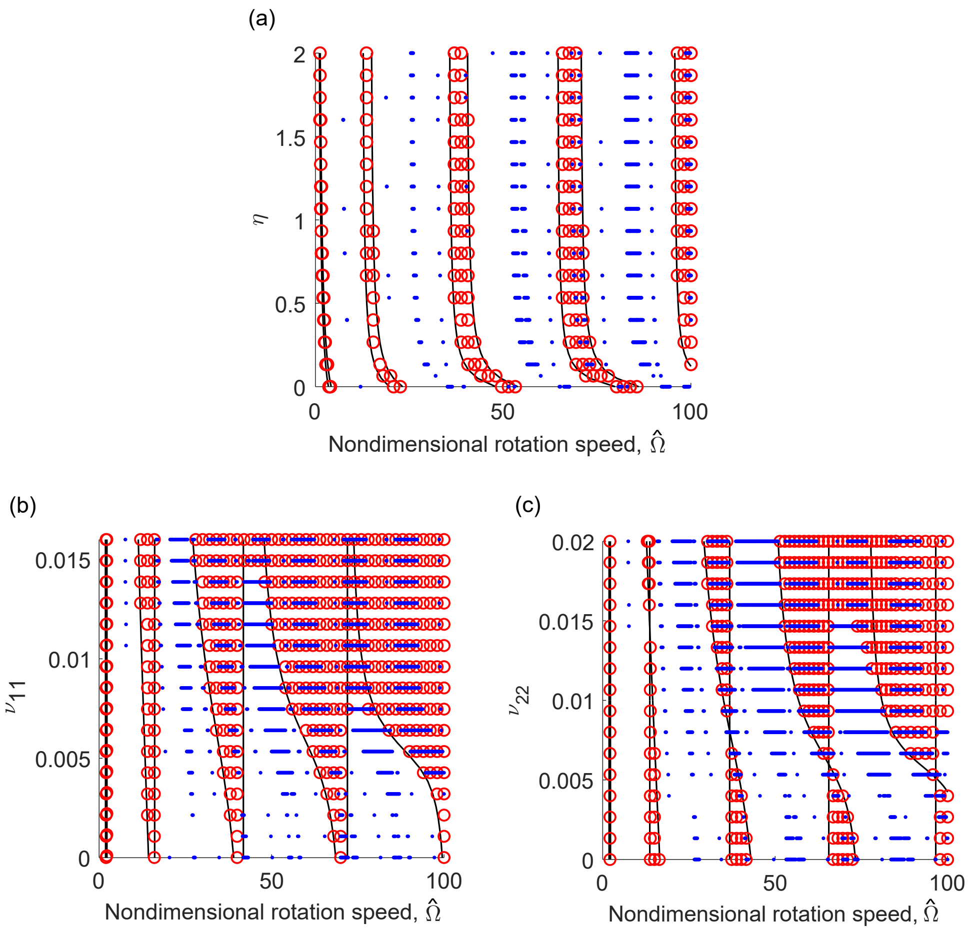

Figure 2.11: High-speed instability behavior for varying rigid body (a) mass η, (b) mass moment of inertia ν_{11}, and (c) mass moment of inertia ν_{22}. The solid (black) lines are critical speeds. The circle (red) and dot (blue) markers denote divergence and flutter instability, respectively. Except for the varying parameters, the system has properties given in Table 2.1 for the asymmetric system.

The unstable eigenvalue thus regains stability. All flutter regions shown in Fig. 2.2 have this typical behavior.

For asymmetric systems, it is possible for more than one eigenvalue to experience divergence instability simultaneously. Typically, this occurs when a region of divergence instability immediately above a critical speed does not end at the next critical speed. Instead, a second eigenvalue experiences divergence instability across that critical speed. An example of this unusual behavior is shown in Fig. 2.12(a). The system has $v_{11} = 0.14$ and the remaining parameters are identical to those in Table 2.1. A root locus plot is included in Fig. 2.12(b). The circles (crosses) represent the initial (final) eigenvalue locations at $\hat{\Omega} = 40$ ($\hat{\Omega} = 45$). Arrows show the direction the eigenvalues travel with increasing rotation speed. The blue lines and markers are stable eigenvalues. The green (red) lines and markers are used to denote eigenvalues that experience divergence (flutter) instability. Across the critical speed at $\hat{\Omega} = 28.098$ (not shown) an eigenvalue experiences divergence instability in the usual way. At $\hat{\Omega} = 40$ the eigenvalue is still unstable. A second eigenvalue begins at B when $\hat{\Omega} = 40$. It approaches the origin of the complex plane as speed increases. At the next critical speed when $\hat{\Omega} = 41.827$ (C), the eigenvalue that began at B vanishes, and the eigenvalue originally at point A remains real-valued and unstable. Immediately above $\hat{\Omega} = 41.827$ (C), the eigenvalue becomes real-valued and positive and experiences divergence instability. Both eigenvalues now experience divergence instability simultaneously for the speed bandwidth between $\hat{\Omega} = 41.827$ (C) and 41.906 (D). Similar behavior has also been shown to occur in high-speed planetary gears [176].

Figures 2.12(a) and (b) demonstrate a second unusual instability feature, where an immediate transition from divergence instability to flutter instability occurs. Immediately above the critical speed $\hat{\Omega} = 41.827$ (C), two eigenvalues are real-valued and positive and experience divergence instability. The lower real-valued eigenvalue increases, while the higher real-valued eigenvalue decreases with increasing speed from $\hat{\Omega} = 41.827$. The real-valued eigenvalues coalesce at $\hat{\Omega} = 41.906$ (D). Immediately above $\hat{\Omega} = 41.906$, one eigenvalue becomes complex-valued with a positive real part and experiences flutter instability. This demonstrates an immediate transition from divergence instability to flutter instability with no stable region separating them. Similar behavior has also been observed in high-speed planetary gears [176] and fluid conveying pipes [177].

Immediate transitions from flutter instability to divergence instability have also been observed. An example is shown in Figs. 2.12(c) and (d). The eigenvalue at A is complex-valued with a positive real part. The imaginary part decreases with increasing speed from A. It coalesces with another eigenvalue at $\hat{\Omega} = 46.088$ (B). Immediately above $\hat{\Omega} = 46.088$, the two eigenvalues split into two real-valued and positive eigenvalues that both experience divergence instability. For increasing speeds from $\hat{\Omega} = 46.088$ (B), one eigenvalue increases along the real axis with increasing speed. The other decreases along the real axis with increasing speed. The decreasing real-valued eigenvalue vanishes at the next critical speed when $\hat{\Omega} = 48.646$ (C). Stability is regained for this eigenvalue for speeds above $\hat{\Omega} = 48.646$.

Figures 2.12(e) and (f) show the eigenvalue loci for the asymmetric system with parameters in Table 2.1 and v_{11} increased from 0.14 to 0.15. At $\hat{\Omega} = 40$ the eigenvalue at A is real-valued and positive and experiences divergence instability. It decreases along the real axis with increasing speed. The eigenvalue at B decreases along the imaginary axis with increasing speed. It vanishes at the critical speed $\hat{\Omega} = 41.815$ (C). Above $\hat{\Omega} = 41.815$, the eigenvalue becomes real-valued and positive and experiences divergence instability. The two eigenvalues approach one another along the real axis as the speed approaches $\hat{\Omega} = 43.3$. Similar to veering, they appear to repel one another, instead of crossing or coalescing, as the rotation speed increases through $\hat{\Omega} = 43.3$. Past the interaction near

$\hat{\Omega} = 43.3$ each eigenvalue appears to follow the trajectory of the other, which is another characteristic typical of veering. Investigation of the modal deformations corresponding to these eigenvalues did not show any special characteristics or coupling in the modes, unlike the typical strong modal coupling that occurs when purely imaginary eigenvalues interact within veering regions. The interaction near $\hat{\Omega} = 43.3$ is therefore not like typical veering seen at lower speeds. For speeds above $\hat{\Omega} = 43.3$, one eigenvalue decreases with increasing speed and vanishes at the next critical speed. Immediately above the critical speed, the eigenvalue is purely imaginary and regains stability. The other eigenvalue remains unstable for the entire range of speeds shown. Because of the interaction near $\hat{\Omega} = 43.3$, only divergence instability occurs. These eigenvalues do not experience flutter instability in the speed range shown.

2.4 Conclusion

Symmetric cantilevered beam-rigid body systems with identical inertia and stiffness properties in the two bending directions have degenerate eigenvalues at zero speed that split, becoming distinct, for non-zero speeds. The increasing eigenvalues correspond to backward orbit vibrations in single-mode free response, where material points along the beam span move in circular orbits in the direction opposite of rotation. The decreasing eigenvalues correspond to forward orbit vibrations in single-mode free response. Material points along the beam span also move in circular orbits in these modes, but their motion is in the direction of rotation. The forward orbit eigenvalues always cross the backward orbit eigenvalues, without interaction, as the rotation speed varies. At high speeds, the forward orbit eigenvalues may experience critical speeds, where the eigenvalue vanishes. Away from critical speeds, the symmetric system's eigenvalues are purely imaginary and stable. The prominence of shear deformations increases with increasing speed for forward orbit

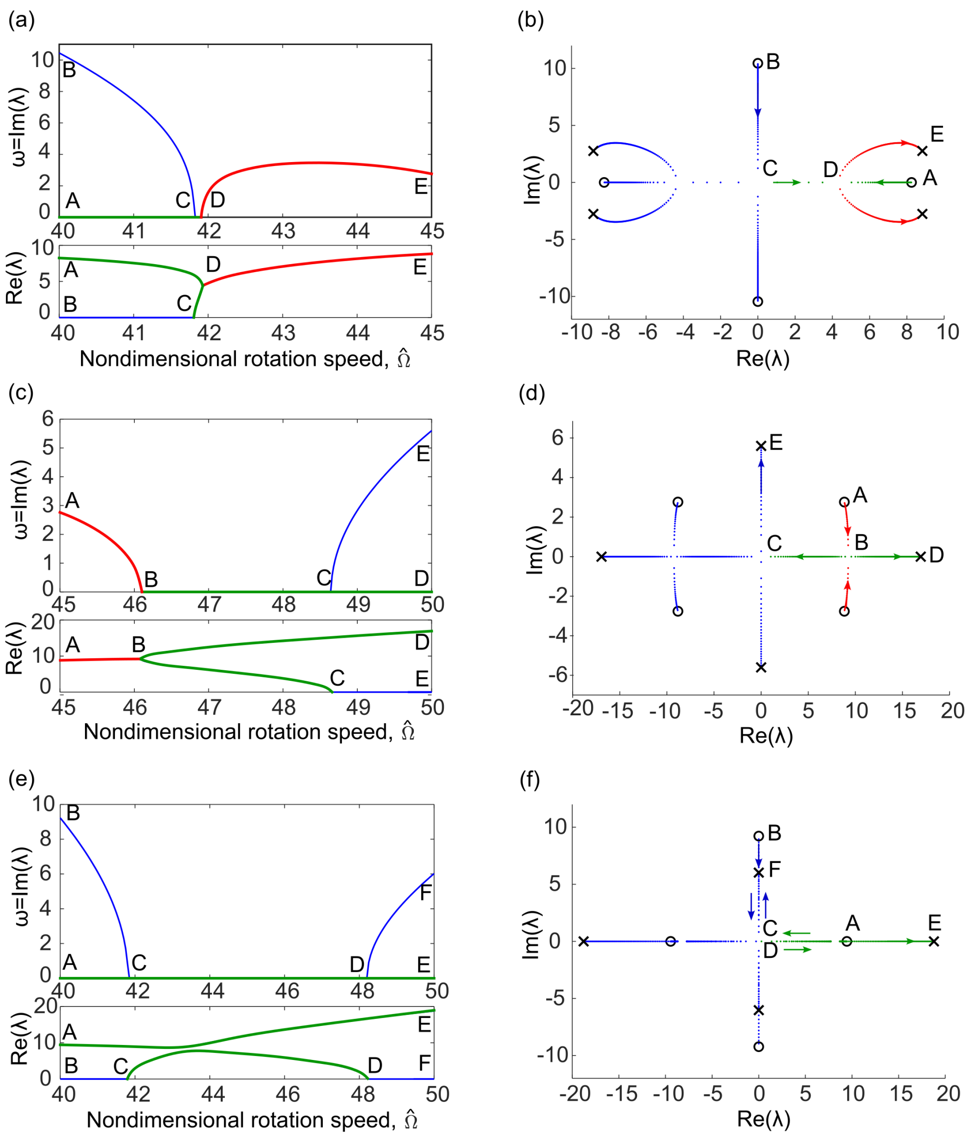

Figure 2.12: The transition between two types of unstable eigenvalues with increasing ν_{11}. Eigenvalue loci for varying speeds are shown in (a, c, e) and their corresponding root loci are shown in (b, d, f). In (a-d) $\nu_{11} = 0.014$, and in (e-f) $\nu_{11} = 0.015$. In (b,d,f) the initial and final locations are denoted using circle and cross markers, respectively. The arrows denote the direction the eigenvalues change with increasing speed. Except for parameter ν_{11}, the system has properties given in Table 2.1 for the asymmetric system.

modes, even though their natural frequencies decrease. Conversely, the prominence of shear deformations decreases with increasing speed for backward orbit modes, even though their natural frequencies increase with increasing speed.

The eigenvalues for asymmetric cantilevered beam-rigid body systems are distinct at zero speed due to the system having different inertia and stiffness properties in the two bending directions. One eigenvalue increases and the other decreases with increasing speed from zero. The locally decreasing and increasing eigenvalues still correspond to forward and backward orbit modes, respectively. Material points along the beam span move in elliptical orbits in single-mode free vibration. Veering interactions occur whenever decreasing forward orbit eigenvalues come into close proximity with increasing backward orbit eigenvalues. Within veering regions the modes become strongly coupled, with forward orbit vibrations in some regions along the span and backward orbit vibrations along others. The presence of both forward and backward orbit vibrations results in sharp changes in the shear strain energy of the interacting modes within the veering region. Flutter instabilities are prominent at high speeds. Certain combinations of rigid body parameters can result in atypical eigenvalue behavior like multiple eigenvalues experiencing divergence instability simultaneously and immediate transitions between divergence and flutter instability.

CHAPTER THREE

CLOSED-FORM ANALYTICAL SOLUTIONS FOR THE VIBRATIONS OF SPINNING TIMOSHENKO BEAM WITH IDENTICAL CROSS-SECTIONS

3.1 Introduction

Achieving an exact analytical solution to mathematical problems is the top priority in studies. Analytical solutions can be used to evaluate the validity and accuracy of the solutions obtained by numerical or approximate methods. They can also contribute to predicting the behavior of similar or more complex dynamic systems and identifying the determining factors. Furthermore, they can be employed to derive approximate solutions for more complicated problems. In vibration problems as an example, deriving approximate formulas for fundamental frequencies through energy-based methods, serving as basis functions in weighted residual techniques, and being used as elastic modes in Component Mode Synthesis (CMS) are notable applications of analytical solutions for this purpose.

Vibrations in the elastic spinning beams under classical boundary conditions were analytically studied by Bauer [5] using the Euler-Bernoulli beam theory. Rotatory inertia and shear deformations are neglected in the Euler-Bernoulli modeling. The effects of rotatory inertia were incorporated in some later studies [10, 12] using the Rayleigh beam theory for the spinning beam. For spinning Timoshenko beams, Zu and Han [18] presented closed-form solutions and mode shapes for six types of boundary conditions. They included both effects of rotary inertia and shear deformations in their analytical investigations. Some modal analysis formulations [10, 13, 14] were also developed to follow these studies.

Vibrating beams carrying various types of rigid bodies or concentrated masses make up a wide range of dynamic systems. Laura et al. [19] obtained closed-form solutions for a non-rotating fixed-free Euler-Bernoulli beam with a lumped mass attached at its free end. The impacts of relatively large tip bodies on the beam vibrations are investigated in Refs. [23, 24]. Bruch et al. [132] and Rossi et al. [20] employed Timoshenko beam theory to study the vibrations of a cantilevered beam with a tip rigid body. Similar non-rotating dynamic systems under various working conditions have also been investigated in a wide range of studies [21, 22, 25, 28, 128]. Free vibrations in spinning Timoshenko shafts carrying concentrated masses or rigid disks were also investigated using analytical and numerical approaches [30, 31].

In this chapter, closed-form solutions for natural frequencies and their corresponding mode shapes are achieved for a spinning cantilever beam with symmetric cross-sectional geometry carrying a rigid body attached at its end. Bending deformations lying on two perpendicular planes are blended in a complex-valued format to halve the number of equations and facilitate the solving process. Mode shapes and their determining coefficients for spinning beams with and without a rigid tip body for a range of rotation speeds are investigated in detail.

3.2 Closed-form modeling of the beam with a symmetric geometry

The dynamic system, consisting of a cantilevered beam and a rigid tip body, rotating about its longitudinal axis at a constant speed Ω, is depicted in Fig. 2.1. The length and cross-sectional area of the beam are represented by L and A. The beam material is isotropic elastic with density ρ, elastic modulus E, and shear modulus G.

The governing equations are

$$\rho A\ddot{U}_1 - 2\Omega\rho A\dot{U}_2 - k_{13}GA(U_{1,33} - \theta_{2,3}) - \Omega^2\rho AU_1 = 0 \tag{3.1a}$$

$$\rho A\ddot{U}_2 + 2\Omega\rho A\dot{U}_1 - k_{23}GA(U_{2,33} + \theta_{1,3}) - \Omega^2\rho AU_2 = 0 \tag{3.1b}$$

$$\rho I_{22}\ddot{\theta}_1 + k_{23}GA(U_{2,3} + \theta_1) - EI_{22}\theta_{1,33} + \Omega^2\rho I_{22}\theta_1 = 0 \tag{3.1c}$$

$$\rho I_{11}\ddot{\theta}_2 - k_{13}GA(U_{1,3}-\theta_2) - EI_{11}\theta_{2,33} + \Omega^2\rho I_{11}\theta_2 = 0, \quad 0 < X_3 < L \tag{3.1d}$$

$$M\ddot{U}_{1c} - 2\Omega M\dot{U}_{2c} + k_{13}GA(U_{1,3}-\theta_2)\big|_L - \Omega^2 MU_{1c} = 0 \tag{3.2a}$$

$$M\ddot{U}_{2c} + 2\Omega M\dot{U}_{1c} + k_{23}GA(U_{2,3}+\theta_1)\big|_L - \Omega^2 MU_{2c} = 0 \tag{3.2b}$$

$$J_{11}\ddot{\Theta}_1 - \Omega\,(J_{11}+J_{22}-J_{33})\,\dot{\Theta}_2 + EI_{22}\theta_{1,3}\big|_L + dk_{23}GA(U_{2,3}+\theta_1)\big|_L - \Omega^2(J_{22}-J_{33})\Theta_1 = 0 \tag{3.2c}$$

$$J_{22}\ddot{\Theta}_2 + \Omega(J_{11}+J_{22}-J_{33})\dot{\Theta}_1 + EI_{11}\theta_{2,3}\big|_L - dk_{13}GA(U_{1,3}-\theta_2)\big|_L - \Omega^2(J_{11}-J_{33})\Theta_2 = 0 \tag{3.2d}$$

Equations (3.1) and (3.2) consist of a set of partial differential equations representing the beam motions that are coupled to a set of ordinary differential equations representing the mass motions. The geometric (essential) boundary conditions at the fixed end are $U_1(0,T)=0$, $U_2(0,T)=0$, $\theta_1(0,T)=0$, and $\theta_2(0,T)=0$.

3.2.1 Nondimensionalized equation

The nondimensional form of variables are given by

$$x_i = \frac{X_i}{L}, \quad t = \frac{1}{L^2}\sqrt{\frac{EI_{11}}{\rho A}}T, \quad u_{1,2} = \frac{U_{1,2}}{L}, \quad \hat{d} = \frac{d}{L}, \quad \kappa = \frac{GAL^2}{EI_{11}}, \quad \mu = \frac{I_{11}}{AL^2},$$
$$\alpha = \frac{I_{22}}{I_{11}}, \quad \eta = \frac{M}{\rho AL}, \quad \hat{\Omega} = \sqrt{\frac{\rho AL^4}{EI_{11}}}\Omega, \quad \nu_{11} = \frac{J_{11}}{\rho AL^3}, \quad \nu_{22} = \frac{J_{22}}{\rho AL^3}, \quad \nu_{33} = \frac{J_{33}}{\rho AL^3} \tag{3.3}$$

The differentiation relations $\partial(\ )/\partial X_3 = (1/L)\partial(\ )/\partial x_3$ and $\partial(\ )/\partial T = \sqrt{EI_{11}/\rho AL^4}\,\partial(\ )/\partial t$ are defined based on these nondimensional parameters. The dimensionless equations of motion and natural boundary conditions result from substituting nondimensional parameters from Eq. (3.3) into Eqs. (3.1) and (3.2)

$$\ddot{u}_1 - 2\hat{\Omega}\dot{u}_2 - k_{13}\kappa(u_{1,33} - \theta_{2,3}) - \hat{\Omega}^2 u_1 = 0 \tag{3.4a}$$

$$\ddot{u}_2 + 2\hat{\Omega}\dot{u}_1 - k_{23}\kappa(u_{2,33} + \theta_{1,3}) - \hat{\Omega}^2 u_2 = 0 \tag{3.4b}$$

$$\alpha\mu\ddot{\theta}_1 + k_{23}\,\kappa\,(u_{2,3} + \theta_1) - \alpha\theta_{1,33} + \hat{\Omega}^2\alpha\mu\theta_1 = 0 \tag{3.4c}$$

$$\mu\ddot{\theta}_2 - k_{13}\kappa(u_{1,3} - \theta_2) - \theta_{2,33} + \hat{\Omega}^2\mu\theta_2 = 0 \tag{3.4d}$$

$$\eta\ddot{u}_{1c} - 2\hat{\Omega}\eta\dot{u}_{2c} + k_{13}\kappa(u_{1,3} - \theta_2)\big|_1 - \hat{\Omega}^2\eta u_{1c} = 0 \tag{3.5a}$$

$$\eta\ddot{u}_{2c} + 2\hat{\Omega}\eta\dot{u}_{1c} + k_{23}\kappa(u_{2,3} + \theta_1)\big|_1 - \hat{\Omega}^2\eta u_{2c} = 0 \tag{3.5b}$$

$$\begin{aligned}\nu_{11}\ddot{\Theta}_1 - \hat{\Omega}(\nu_{11} + \nu_{22} - \nu_{33})\dot{\Theta}_2 + \alpha\theta_{1,3}\big|_1 + \hat{d}k_{23}\kappa(u_{2,3} + \theta_1)\big|_1 \\ - \hat{\Omega}^2(\nu_{22} - \nu_{33})\Theta_1 = 0\end{aligned} \tag{3.5c}$$

$$\nu_{22}\ddot{\Theta}_2 + \hat{\Omega}(\nu_{11} + \nu_{22} - \nu_{33})\dot{\Theta}_1 + \theta_{2,3}\big|_1 - \hat{d}k_{13}\kappa(u_{1,3} - \theta_2)\big|_1 - \hat{\Omega}^2(\nu_{11} - \nu_{33})\Theta_2 = 0 \tag{3.5d}$$

The resulting dimensionless boundary conditions at the fixed end are $u_1(0,t) = 0$ and $u_2(0,t) = 0$ for transverse displacements and $\theta_1(0,t) = 0$ and $\theta_2(0,t) = 0$ for rotational displacements.

3.2.2 Analytical modeling of the closed-form solution

The vibration of a spinning beam with a rigid body attached to its tip has forward- and backward-orbit vibrations at all stable speeds away from veering regions. The vibration of spinning beams with identical cross-sections has additional vibration properties that do not occur for beams with non-identical cross-sections. Specifically, the vibrations of the rigid body and all material points along the beam span execute perfectly circular orbits in single-mode response.

The physical characteristics of the single-mode vibration result in specific mathematical properties in the vibration modes. These properties are shown in Fig. 2.3(a) and (b) for the first forward-orbit and backward-orbit mode, respectively. In the forward-orbit mode (Fig. 2.3(a)), the modal deformations $u_1(x_3) = u(x_3)$ and $u_2(x_3) = -\mathrm{j}u(x_3)$. The rotational deformations $\theta_1(x_3) = \Theta(x_3)$ and $\theta_2(x_3) = \mathrm{j}\Theta(x_3)$. For the backward-orbit mode the translational deformations $u_1(x_3) = u(x_3)$ and $u_2(x_3) = \mathrm{j}u(x_3)$, and the rotational deformations $\theta_1(x_3) = -\mathrm{j}\Theta(x_3)$ and $\theta_2(x_3) = \Theta(x_3)$.

The mathematical structure of the modes also permits model reduction for a more efficient numerical solution. Eqs. (3.4) consist of four second-order equations, making the system of equations eight-order. The satisfaction of all boundary conditions would require the determinant of an eight-dimensional square matrix. Closed-form solutions would be challenging. As will be seen, the mathematical properties reduce the number of unknowns and decrease the number of equations that must be solved.

The modal mathematical structure is lost for non-identical cross-sections when the inertial and stiffness properties in the two bending directions differ. This is shown numerically in Fig. 2.4 for the second pair of bending modes. These modes have differing modal translational and rotational deformation amplitudes.

For a system with symmetric geometry, the transverse deformations at any point on the beam's neutral axis are defined in the complex form $u = u_1 \pm \mathrm{j}u_2$. The plus (minus) sign in u relation corresponds to forward (backward) orbits. The rotational deformations at any point on the beam's neutral axis about two consecutive independent axes perpendicular to $\mathbf{E}_3$ are defined in the complex form $\Theta = \theta_2 \mp j\theta_1$. The minus (plus) sign in Θ relation corresponds to forward (backward) orbits.

The four nondimensional equations of motion in Eqs. (3.4) for the symmetric system converts into a complex form consisting of two equations.

$$\ddot{u} \pm 2j\hat{\Omega}\dot{u} - k_{13}\kappa(u_{,33} - \Theta_{,3}) - \hat{\Omega}^2 u = 0 \tag{3.6a}$$

$$\mu\ddot{\Theta} - k_{13}\kappa(u_{,3} - \Theta) - \Theta_{,33} + \hat{\Omega}^2\mu\Theta = 0 \tag{3.6b}$$

The nondimensional essential boundary conditions at the fixed end for the symmetric system convert into the complex forms $u(0,t) = 0$ and $\Theta(0,t) = 0$.

Similarly, the nondimensional natural boundary conditions at the free end in Eqs. (3.7) convert into complex forms as follows

$$\eta\ddot{u}_c \pm 2j\hat{\Omega}\eta\dot{u}_c + k_{13}\kappa(u_{,3} - \Theta)\big|_1 - \hat{\Omega}^2\eta u_c = 0 \tag{3.7a}$$

$$\nu_{22}\ddot{\Theta} \pm j\hat{\Omega}(\nu_{11} + \nu_{22} - \nu_{33})\dot{\Theta} + \Theta_{,3}\big|_1 - \hat{d}k_{13}\kappa(u_{,3} - \Theta)\big|_1 - \hat{\Omega}^2(\nu_{11} - \nu_{33})\Theta = 0 \tag{3.7b}$$

where $\nu_{11} = \nu_{22}$ and the plus (minus) signs in these equations correspond to the forward (backward) orbit modes. The number of equations in the boundary conditions on each side is reduced from four to two.

For homogeneous equations of motion, the separable solutions are assumed to be $u(x,t) = U(x)e^{i\omega t}$, $\Theta(x,t) = \Theta(x)e^{i\omega t}$. Both mode shapes have a similar form as $U(x) = ae^{rx}$ and $\Theta(x) = be^{rx}$. Substitution of these solutions into Eq. (3.6) gives the eigenvalue problem in the matrix form as follows

$$\begin{bmatrix} -(\omega \pm \hat{\Omega})^2 - k_{13}\kappa r^2 & k_{13}\kappa r \\ -k_{13}\kappa r & k_{13}\kappa - \mu(\omega + \hat{\Omega})(\omega + \hat{\Omega}) - r^2 \end{bmatrix} \begin{bmatrix} a \\ b \end{bmatrix} = \begin{bmatrix} 0 \\ 0 \end{bmatrix} \tag{3.8}$$

where the plus (minus) sign corresponds to forward (backward) orbits.

A nontrivial solution of Eq. (3.8) exists only if the determinant of the coefficient matrix vanishes. Equating the determinant of this matrix with zero gives the mode coefficients r_1 and r_2 as

$$r_1^2, r_2^2 = -\frac{(\omega+\hat{\Omega})\left[\omega+\hat{\Omega}+k_{13}\kappa\mu(\omega-\hat{\Omega}) \pm \sqrt{[\omega+\hat{\Omega}-k_{13}\kappa\mu(\omega-\hat{\Omega})]^2+(2k_{13}\kappa)^2}\right]}{2k_{13}\kappa} \tag{3.9a}$$

for forward orbits and

$$r_1^2, r_2^2 = -\frac{(\omega-\hat{\Omega})\left[\omega-\hat{\Omega}+k_{13}\kappa\mu(\omega+\hat{\Omega}) \pm \sqrt{[\omega-\hat{\Omega}-k_{13}\kappa\mu(\omega+\hat{\Omega})]^2+(2k_{13}\kappa)^2}\right]}{2k_{13}\kappa} \tag{3.9b}$$

for backward orbits. r_1 and r_2 are distinguished by the condition $r_1^2 < 0$ and $r_2^2 > 0$. Mode shapes as general solutions are made up of trigonometric functions of $(r_1 x)$ and hyperbolic functions of $(r_2 x)$ as follows

$$U(x) = C_1\cos(r_1x)+C_2\sin(r_1x)+C_3\cosh(r_2x)+C_4\sinh(r_2x) \tag{3.10a}$$

$$\begin{aligned}\phi(x) = {} & \frac{C_1\left[(\omega\pm\hat{\Omega})^2-k_{13}\kappa r_1^2\right]}{k_{13}\kappa r_1}\sin(r_1x) - \frac{C_2\left[(\omega\pm\hat{\Omega})^2-k_{13}\kappa r_1^2\right]}{k_{13}\kappa r_1}\cos(r_1x) \\ & + \frac{C_3\left[(\omega\pm\hat{\Omega})^2+k_{13}\kappa r_2^2\right]}{k_{13}\kappa r_2}\sinh(r_2x) + \frac{C_4\left[(\omega\pm\hat{\Omega})^2+k_{13}\kappa r_2^2\right]}{k_{13}\kappa r_2}\cosh(r_2x)\end{aligned} \tag{3.10b}$$

In the same way, the plus (minus) sign corresponds to forward (backward) orbits. Substituting the mode shapes from Eqs. (3.10) into the essential boundary conditions $u(0,t) = 0$ and $\Theta(0,t) = 0$ and natural boundary conditions in Eqs. (3.7) yields

$$[\mathbf{A}]\mathbf{c} = \mathbf{0} \tag{3.11a}$$

$$\mathbf{c} = [C_1, C_2, C_3, C_4]^T \tag{3.11b}$$

$$[\mathbf{A}] = \begin{bmatrix} 1 & 0 & 1 & 0 \\ 0 & A_{22} & 0 & A_{44} \\ A_{31} & A_{32} & A_{33} & A_{34} \\ A_{41} & A_{42} & A_{43} & A_{44} \end{bmatrix} \tag{3.12a}$$

$$A_{22} = \frac{(\omega \pm \hat{\Omega})^2 - k_{13}\kappa r_1^2}{r_1} \tag{3.12b}$$

$$A_{24} = -\frac{(\omega \pm \hat{\Omega})^2 + k_{13}\kappa r_2^2}{r_2} \tag{3.12c}$$

$$A_{31} = \frac{-(\omega \pm \hat{\Omega})^2 \left\{ \eta \left[\left((\omega \pm \hat{\Omega})^2 - k_{13}\kappa r_1^2 \right) \hat{d} \sin(r_1) + k_{13}\kappa r_1 \cos(r_1) \right] + k_{13}\kappa \sin(r_1) \right\}}{r_1} \tag{3.12d}$$

$$A_{32} = \frac{-(\omega \pm \hat{\Omega})^2 \left\{ \eta \left[\left(-(\omega \pm \hat{\Omega})^2 + k_{13}\kappa r_1^2 \right) \hat{d} \cos(r_1) + k_{13}\kappa r_1 \sin(r_1) \right] - k_{13}\kappa \cos(r_1) \right\}}{r_1} \tag{3.12e}$$

$$A_{33} = \frac{-(\omega \pm \hat{\Omega})^2 \left\{ \eta \left[\left((\omega \pm \hat{\Omega})^2 + k_{13}\kappa r_1^2 \right) \hat{d} \sinh(r_1) + k_{13}\kappa r_1 \cosh(r_1) \right] + k_{13}\kappa \sinh(r_1) \right\}}{r_1} \tag{3.12f}$$

$$A_{34} = \frac{-(\omega \pm \hat{\Omega})^2 \left\{ \eta \left[\left((\omega \pm \hat{\Omega})^2 - k_{13}\kappa r_1^2 \right) \hat{d} \sin(r_1) + k_{13}\kappa r_1 \cos(r_1) \right] + k_{13}\kappa \sin(r_1) \right\}}{r_1} \tag{3.12g}$$

$$A_{41} = \frac{-\left[\omega^2 \nu_{11} \pm \omega\hat{\Omega}(2\nu_{11} - \nu_{33}) + \hat{\Omega}^2(\nu_{11} - \nu_{33}) \right] \left[(\omega \pm \hat{\Omega})^2 - k_{13}\kappa r_1^2 \right] + \hat{d} k_{13}\kappa(\omega \pm \hat{\Omega})^2}{r_1} \times \sin(r_1) + \left[(\omega \pm \hat{\Omega})^2 - k_{13}\kappa r_1^2 \right] \cos(r_1) \tag{3.12h}$$

$$A_{42} = \frac{\left[\omega^2 \nu_{11} \pm \omega\hat{\Omega}(2\nu_{11} - \nu_{33}) + \hat{\Omega}^2(\nu_{11} - \nu_{33}) \right] \left[(\omega \pm \hat{\Omega})^2 - k_{13}\kappa r_1^2 \right] - \hat{d} k_{13}\kappa(\omega \pm \hat{\Omega})^2}{r_1} \times \cos(r_1) + \left[(\omega \pm \hat{\Omega})^2 - k_{13}\kappa r_1^2 \right] \sin(r_1) \tag{3.12i}$$

$$A_{43} = \frac{-\left[\omega^2\nu_{11} \pm \omega\hat{\Omega}(2\nu_{11}-\nu_{33}) + \hat{\Omega}^2(\nu_{11}-\nu_{33})\right]\left[(\omega\pm\hat{\Omega})^2 + k_{13}\kappa r_2^2\right] + \hat{d}k_{13}\kappa(\omega\pm\hat{\Omega})^2}{r_2} \times \sinh(r_2) + \left[(\omega\pm\hat{\Omega})^2 + k_{13}\kappa r_2^2\right]\cosh(r_2) \quad (3.12j)$$

$$A_{44} = \frac{-\left[\omega^2\nu_{11} \pm \omega\hat{\Omega}(2\nu_{11}-\nu_{33}) + \hat{\Omega}^2(\nu_{11}-\nu_{33})\right]\left[(\omega\pm\hat{\Omega})^2 + k_{13}\kappa r_2^2\right] + \hat{d}k_{13}\kappa(\omega\pm\hat{\Omega})^2}{r_2} \times \cosh(r_2) + \left[(\omega\pm\hat{\Omega})^2 + k_{13}\kappa r_2^2\right]\sinh(r_2) \quad (3.12k)$$

Where matrix $[\mathbf{A}]$ determines the boundary conditions. The plus (minus) signs in $\omega \pm \hat{\Omega}$ are associated with the forward (backward) orbit modes. The effects of the rigid tip body and its offset are also included in these relations. Eigenvalues are calculated numerically by solving $\det([\mathbf{A}]) = 0$, where $[\mathbf{A}]$ is considered the characteristic equation. For the beam without any rigid tip body, parameters η and ν are zero.

3.2.3 The closed-form solutions for the critical speeds

Critical speeds are characterized as the speeds at where an eigenvalue vanishes. Critical speeds can be computed by assuming $\omega = 0$ in Eq. (3.12). The coefficients r_1 and r_2 can be calculated by the relation below

$$r_1^2, r_2^2 = -\frac{\hat{\Omega}_{Cr}^2\left[1 - k_{13}\kappa\mu \pm \sqrt{(1-k_{13}\kappa\mu)^2 + \left(\frac{2k_{13}\kappa}{\hat{\Omega}_{Cr}}\right)^2}\right]}{2k_{13}\kappa} \quad (3.13)$$

Similarly, the mode shapes for critical speeds are

$$U(x) = C_1 \cos(r_1 x) + C_2 \sin(r_1 x) + C_3 \cosh(r_2 x) + C_4 \sinh(r_2 x) \tag{3.14a}$$

$$\begin{aligned}\phi(x) = {} & \frac{C_1 \left[\hat{\Omega}_{Cr}^2 - k_{13}\kappa r_1^2\right]}{k_{13}\kappa r_1} \sin(r_1 x) - \frac{C_2 \left[\hat{\Omega}_{Cr}^2 - k_{13}\kappa r_1^2\right]}{k_{13}\kappa r_1} \cos(r_1 x) \\ & + \frac{C_3 \left[\hat{\Omega}_{Cr}^2 + k_{13}\kappa r_2^2\right]}{k_{13}\kappa r_2} \sinh(r_2 x) + \frac{C_4 \left[\hat{\Omega}_{Cr}^2 + k_{13}\kappa r_2^2\right]}{k_{13}\kappa r_2} \cosh(r_2 x)\end{aligned} \tag{3.14b}$$

Substituting the mode shapes from Eqs. (3.14) into the essential boundary conditions and natural boundary conditions in Eqs. (3.7) gives

$$[\mathbf{B}]\mathbf{c} = \mathbf{0} \tag{3.15a}$$

$$\mathbf{c} = [C_1, C_2, C_3, C_4]^T \tag{3.15b}$$

$$[\mathbf{B}] = \begin{bmatrix} 1 & 0 & 1 & 0 \\ 0 & B_{22} & 0 & B_{44} \\ B_{31} & B_{32} & B_{33} & B_{34} \\ B_{41} & B_{42} & B_{43} & B_{44} \end{bmatrix} \tag{3.16a}$$

$$B_{22} = \frac{\hat{\Omega}_{Cr}^2 - k_{13}\kappa r_1^2}{r_1} \tag{3.16b}$$

$$B_{24} = -\frac{\hat{\Omega}_{Cr}^2 + k_{13}\kappa r_2^2}{r_2} \tag{3.16c}$$

$$B_{31} = \frac{-\hat{\Omega}_{Cr}^2 \left\{\eta \left[\left(\hat{\Omega}_{Cr}^2 - k_{13}\kappa r_1^2\right)\hat{d}\sin(r_1) + k_{13}\kappa r_1 \cos(r_1)\right] + k_{13}\kappa \sin(r_1)\right\}}{r_1} \tag{3.16d}$$

$$B_{32} = \frac{-\hat{\Omega}_{Cr}^2 \left\{ \eta \left[\left(-\hat{\Omega}_{Cr}^2 + k_{13}\kappa r_1^2 \right) \hat{d} \cos(r_1) + k_{13}\kappa r_1 \sin(r_1) \right] - k_{13}\kappa \cos(r_1) \right\}}{r_1} \tag{3.16e}$$

$$B_{33} = \frac{-\hat{\Omega}_{Cr}^2 \left\{ \eta \left[\left(\hat{\Omega}_{Cr}^2 + k_{13}\kappa r_1^2 \right) \hat{d} \sinh(r_1) + k_{13}\kappa r_1 \cosh(r_1) \right] + k_{13}\kappa \sinh(r_1) \right\}}{r_1} \tag{3.16f}$$

$$B_{34} = \frac{-\hat{\Omega}_{Cr}^2 \left\{ \eta \left[\left(\hat{\Omega}_{Cr}^2 - k_{13}\kappa r_1^2 \right) \hat{d} \sin(r_1) + k_{13}\kappa r_1 \cos(r_1) \right] + k_{13}\kappa \sin(r_1) \right\}}{r_1} \tag{3.16g}$$

$$B_{41} = \frac{-\left[\hat{\Omega}_{Cr}^2 (\nu_{11} - \nu_{33}) \right] \left[\hat{\Omega}_{Cr}^2 - k_{13}\kappa r_1^2 \right] + \hat{d} k_{13}\kappa \hat{\Omega}_{Cr}^2}{r_1} \sin(r_1) + \left[\hat{\Omega}_{Cr}^2 - k_{13}\kappa r_1^2 \right] \cos(r_1) \tag{3.16h}$$

$$B_{42} = \frac{\left[\hat{\Omega}_{Cr}^2 (\nu_{11} - \nu_{33}) \right] \left[\hat{\Omega}_{Cr}^2 - k_{13}\kappa r_1^2 \right] - \hat{d} k_{13}\kappa \hat{\Omega}_{Cr}^2}{r_1} \cos(r_1) + \left[\hat{\Omega}_{Cr}^2 - k_{13}\kappa r_1^2 \right] \sin(r_1) \tag{3.16i}$$

$$B_{43} = \frac{-\left[\hat{\Omega}_{Cr}^2 (\nu_{11} - \nu_{33}) \right] \left[\hat{\Omega}_{Cr}^2 + k_{13}\kappa r_2^2 \right] + \hat{d} k_{13}\kappa \hat{\Omega}_{Cr}^2}{r_2} \sinh(r_2) + \left[\hat{\Omega}_{Cr}^2 + k_{13}\kappa r_2^2 \right] \cosh(r_2) \tag{3.16j}$$

$$B_{44} = \frac{-\left[\hat{\Omega}_{Cr}^2(\nu_{11}-\nu_{33})\right]\left[\hat{\Omega}_{Cr}^2 + k_{13}\kappa r_2^2\right] + \hat{d}k_{13}\kappa\hat{\Omega}_{Cr}^2}{r_2}\cosh(r_2) + \left[\hat{\Omega}_{Cr}^2 + k_{13}\kappa r_2^2\right]\sinh(r_2) \quad (3.16k)$$

Solving $\det([\mathbf{B}]) = 0$ in Eq. (3.16) yields the critical speeds $\hat{\Omega}_{Cr}$.

3.3 Closed-form solution results

In this section, the results of the closed-form solutions are computed for a cantilevered beam with a relatively large rigid tip mass as an example. The overall cross-sectional geometry of the system is deemed to be symmetric. This system comprises a tubular beam and a rigid tip body, both with a square cross-section. They possess identical inertial and stiffness properties in the two perpendicular directions. The geometric and material parameters of this Beam-rigid body system are listed in Table 2.1. The beam cross-section is considered relatively thick for meaningful shear deformation.

$\det([\mathbf{A}]) = 0$ is solved to calculate the natural frequencies ω. The natural frequencies for the forward and backward orbit modes are computed separately using distinct sets of equations. The coefficients r_1 and r_2 are determined from Eqs. (3.9)(a) for forward orbit modes and from Eqs. (3.9)(b) for backward orbit modes. The boundary conditions on the fixed side of the beam require C_3 to be equal to $-C_1$. The coefficients C_2 and C_4 can be determined by equating the three relations out of four relations of the boundary conditions in Eq. (3.12). Coefficient C_1 is assumed to be one (unity) to set a specific uniform scale for the mode shapes. These coefficients can also be determined from the null space basis of matrix $\mathbf{A}$ for the computed natural frequencies.

Figure 3.1 shows natural frequencies calculated for a wide range of nondimensional rotation speeds. The natural frequencies computed by the analytical closed-form solutions

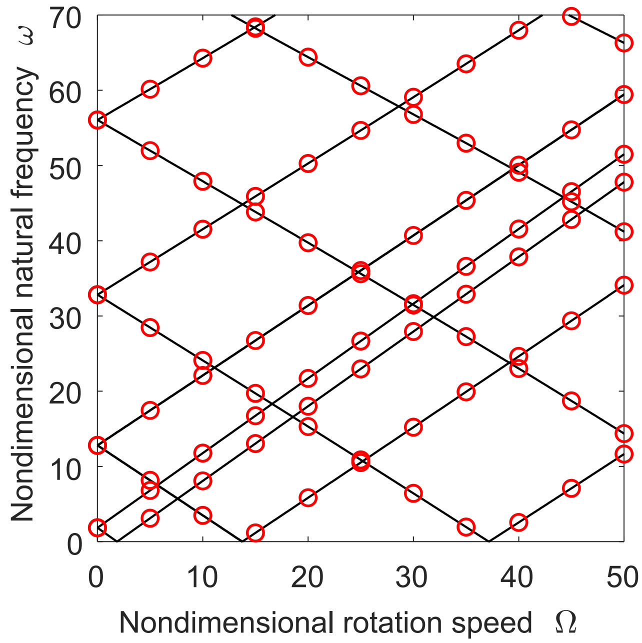

Figure 3.1: Beam-rigid body natural frequencies for varying nondimensional rotation speed. The black lines correspond to closed-form solutions. The red circles correspond to the Galerkin method results. The parameters are given in Table 2.1.

are shown in black lines. The same results, determined by the Galerkin method, are also shown in red circles in 3.1 to compare with the closed-form solution results.

The increasing (decreasing) natural frequencies corresponding to the backward (forward) modes are computed from $\det[\mathbf{A}] = 0$ in Eq. (3.12) by considering the minus (plus) sign in relation $(\omega \pm \hat{\Omega})$. At zero speed, the natural frequencies are degenerate because the beam cross-section is symmetric and the bending stiffnesses are equal. A complete agreement between the closed-form solution results and the Galerkin solutions is observed. The critical speeds (where the eigenvalue vanishes) are degenerate.

3.3.1 Mode characteristics for the system with no rigid tip body

Variations in the mode shape coefficients r_1, r_2, C_2, and C_4 of the first mode of the spinning system without any tip body for a wide range of rotation speeds are shown in Figs. 3.2. Results are calculated separately for each forward and backward orbit mode. The natural frequencies of the first mode over a range of rotation speeds are shown in Figs. 3.2 (a). The solid black lines correspond to the first forward mode, and the dashed red lines correspond to the first backward mode.

Figures 3.2 (b) and (c) show the variations in the coefficients r_1 and r_2 for the first forward and backward modes versus the rotation speed, respectively. The solid blue lines correspond to the coefficient r_1 and the dashed red lines correspond to the coefficient r_2. The coefficients r_1 and r_2 differ slightly over a wide range of rotation speeds for both forward and backward modes. For the forward mode from $\hat{\Omega} = 0$ to $\hat{\Omega} = 50$, r_1 varies from 1.868 to 1.890, while r_2 varies from 1.826 to 2.023. For the backward mode, r_1 varies from 1.868 to 1.842, while r_2 varies from 1.826 to 1.644.

Figures 3.2 (d) and (e) show the variations in the modal coefficients C_2 and C_4 for the first pair of forward and backward modes over the rotation speed, respectively. The solid blue lines correspond to C_2, and the dashed red lines correspond to C_4. Also, C_3 equals -1 or $-C_1$. The coefficients C_2 and C_4 do not differ meaningfully over a wide range of rotation speeds for both forward and backward modes. For the forward mode from $\hat{\Omega} = 0$ to $\hat{\Omega} = 50$, C_2 varies from -0.766 to -0.635, while C_4 varies from 0.725 to 0.664. For the backward mode, C_2 varies from -0.766 to -0.912, while C_4 varies from 0.725 to 0.781. Similarly, slight differences are observed in the coefficients between the forward and backward modes. Since the mode shapes are determined by these coefficients, small changes in their magnitudes suggest that the mode shapes corresponding to the first mode do not change meaningfully.

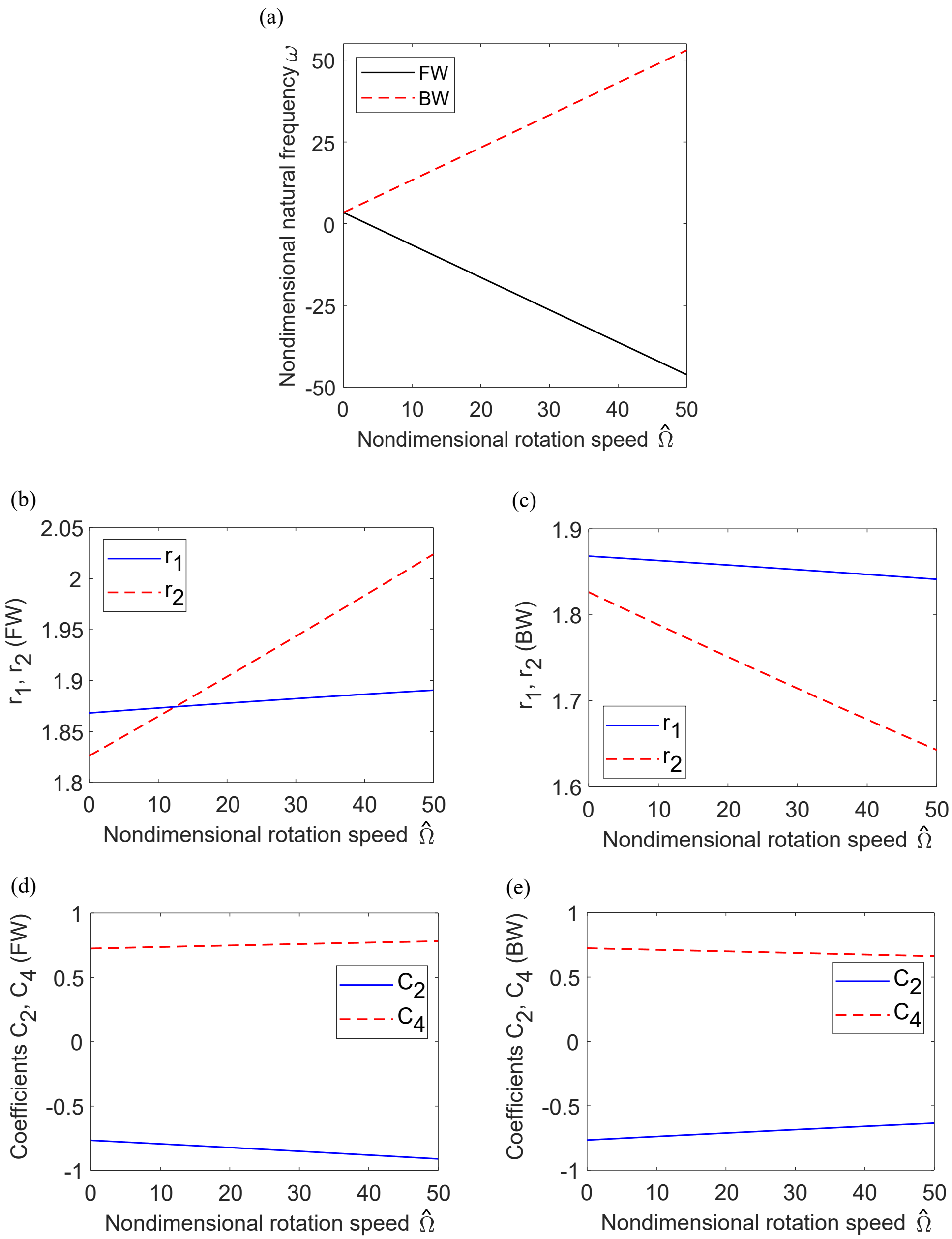

Figure 3.2: (a) variation in the first mode natural frequencies for varying speeds in the system with no tip mass. (b-e) variations in the corresponding coefficients for varying speeds. (b) and (d) correspond to forward (FW) orbits. (c) and (e) correspond to backward (BW) orbits.

Figures 3.2 show the variations in the mode shape coefficients r_1, r_2, C_2, and C_4 for the third forward and backward modes of the spinning system with no tip mass over a broad range of rotation speeds. Similar to the previous section, the coefficients $C_1 = 1$ and $C_3 = -1$. The natural frequencies of the third mode for the varying rotation speed are shown in Fig. 3.3 (a). Variations in the coefficients r_1 and r_2 for the third forward and backward modes versus the rotation speed are presented in Figs. 3.3 (b) and (c) respectively. The coefficients r_1, used in the trigonometric function, do not differ meaningfully over a wide range of rotation speeds for both forward and backward modes. The coefficients r_2, used in hyperbolic functions, exhibit larger but still insignificant changes across the speed range. For the forward mode from $\hat{\Omega} = 0$ to $\hat{\Omega} = 100$, r_1 varies from 7.593 to 7.759, while r_2 varies from 5.660 to 6.822. For the backward mode, r_1 varies from 7.593 to 7.415, while r_2 varies from 5.660 to 4.619.

Variations in the modal coefficients C_2 and C_4 over the rotation speed for the third forward and backward modes are shown in Figs. 3.3 (d) and (e) respectively. Neither the coefficients differ noticeably over a wide range of rotation speeds for both forward and backward modes. Variations in C_4 as the coefficient of hyperbolic functions are negligible. For the forward mode from $\hat{\Omega} = 0$ to $\hat{\Omega} = 100$, C_2 varies from -2.018 to -2.576, while C_4 varies from 0.992 to 0.998. For the backward mode, C_2 varies from -2.018 to -1.559, while C_4 varies from 0.992 to 0.981. Similarly, a slight difference is observed between the forward and backward modes. Although variations in coefficients r_2 are rather noticeable over the rotation speed, variations in coefficients C_4 are negligible. This softens the total changes. Small changes in the determining coefficients indicate that the mode shapes do not change significantly.

Figure 3.4 shows the changes that occur in the bending and rotational mode shapes after applying a relatively high spinning speed. Figure 3.4 (a-b) shows the bending and

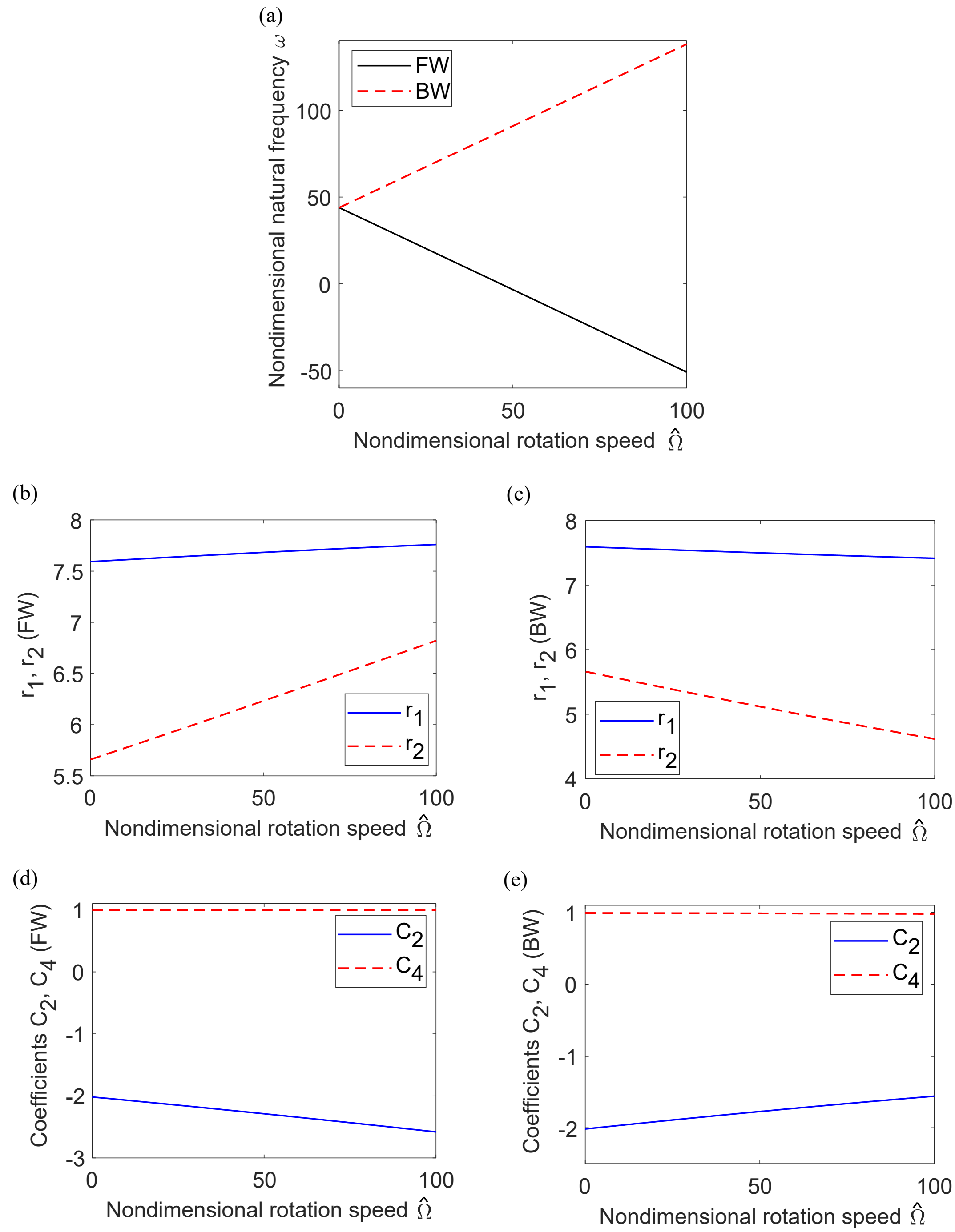

Figure 3.3: (a) variation in the third mode natural frequencies for varying speed in the system with no tip mass. (b-e) variations in the determining coefficients for varying speeds. (b) and (d) correspond to forward (FW) orbits. (c) and (e) correspond to backward (BW) orbits.

rotational mode shapes in the first mode, whereas Figs. 3.4 (c-d) shows the mode shapes for the third mode. The first and third modes are selected for the investigation. Comparison is also made between the forward and backward modes of the first and third mode numbers. The results indicate that although increasing the rotation speed causes some changes in the mode shapes, it keeps the general form of the mode shapes, which can be considered insignificant. This difference is more meaningful when the forward and backward orbit modes are compared. By increasing the speed, the mode shapes of the forward and backward orbits vary in two opposite directions.

3.3.2 Mode characteristics for the system with a relatively large tip mass

A similar investigation is also performed for the spinning system carrying a relatively large rigid tip body. Fig. 3.5 shows the variations in the mode shape coefficients r_1, r_2, C_2, and C_4 for each forward and backward orbit of the first mode, where $C_1 = 1$ and C_3=-1. The natural frequencies of the first mode for the varying rotation speed are shown in Fig. 3.5 (a). The solid black lines correspond to the first forward mode, and the dashed red lines correspond to the first backward mode. Variations in the coefficients r_1 and r_2 for the first forward and backward modes versus the rotation speed are shown in Fig. 3.5 (b) and (c) respectively. The solid blue lines correspond to the coefficient r_1 and the dashed red lines correspond to the coefficient r_2. The coefficients r_1 and r_2 differ slightly over a wide range of rotation speeds ($0 < \hat{\Omega} < 50$) for forward and backward modes. The coefficient r_1 in the forward mode varies from 1.368 to 1.430 over this speed range. The coefficient r_2 in the forward mode varies from 1.352 to 1.547. The coefficient r_1 in the backward mode varies from 1.368 to 1.289. The coefficient r_2 in the backward mode varies from 1.352 to 1.162.

Variations in the modal coefficients C_2 and C_4 for the first forward and backward modes over the speed range are shown in Fig. 3.5 (d) and (e), respectively. The solid blue

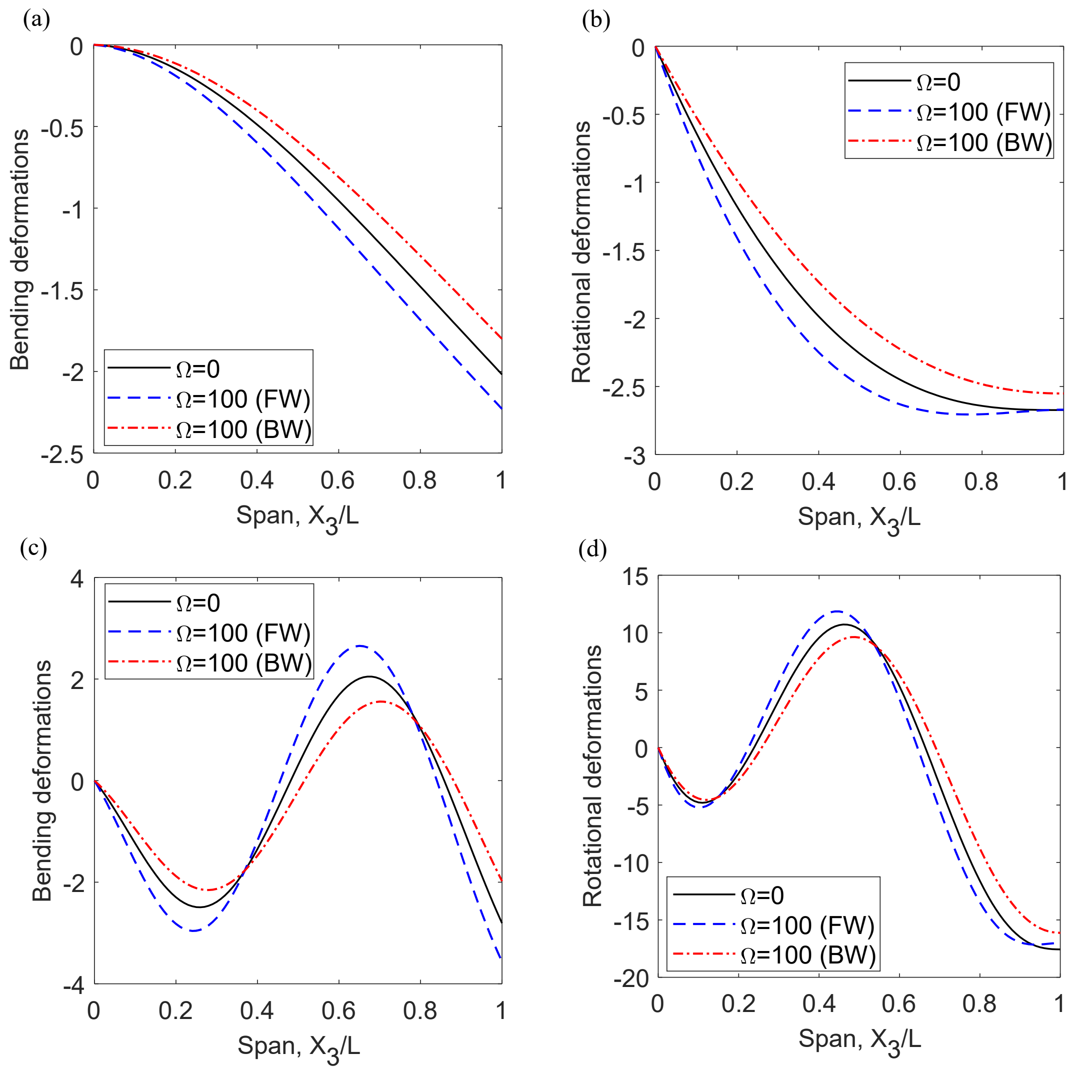

Figure 3.4: Bending and rotational mode shapes in the system with no rigid tip body for $\hat{\Omega} = 0$ and $\hat{\Omega} = 100$ (a-b) First mode. (b-c) Third mode. The solid black lines correspond to zero speed. The dashed blue lines correspond to forward modes in $\hat{\Omega} = 100$. The dashed-dotted red lines correspond to backward modes in $\hat{\Omega} = 100$.

lines correspond to C_2, and the dashed red lines correspond to C_4. All these coefficients do not vary meaningfully over a wide range of rotation speeds ($0 < \hat{\Omega} < 50$) for both forward and backward modes. Variations in C_4 as the coefficient of hyperbolic functions are negligible. C_2 in the forward mode varies from -0.802 to -0.996 over this range. C_4 in the forward varies from 0.777 to 0.876. C_2 in the backward mode varies from -0.766 to -0.611. C_4 in the backward mode varies from 0.725 to 0.655. Consequently, no meaningful changes are seen in the mode shapes corresponding to the first mode over the speed range.

Figure 3.6 shows the variations in the mode shape coefficients r_1, r_2, C_2, and C_4 for each forward and backward orbit of the third mode. The natural frequencies of the third mode for varying rotation speeds are shown in Figure 3.6 (a). Variations in the coefficients r_1 and r_2 versus a range of rotation speeds ($0 < \hat{\Omega} < 100$) for the third forward and backward modes are shown in (b) and (c), respectively. Variations in both coefficients r_1 and r_2 over the speed range are not negligible. r_1 (r_2) in the forward mode varies from 6.363 (5.105) to 6.955 (6.399) over the speed range. r_1 (r_2) in the backward mode varies from 6.363 (5.105) to 5.620 (3.935).

Variations in the modal coefficients C_2 and C_4 versus the speed range ($0 < \hat{\Omega} < 100$) for the third forward and backward modes are shown in (d) and (e), respectively. The solid blue lines correspond to C_2, the dashed red lines correspond to C_4. All these coefficients do not differ meaningfully over a wide range of rotation speeds for both forward and backward orbit modes. C_2 (C_4) in forward mode varies from -1.690 (0.994) to -2.312 (1.001). C_2 (C_4) in backward mode varies from -1.690 (0.994) to -1.559 (0.967). As a result, the mode shapes corresponding to the third mode experience noticeable changes.

Figure 3.7 shows the differences between the mode shapes of the system with a tip mass under stationary and high-speed conditions. Figure 3.7 (a) and (b) show the bending and rotational modal shapes for the first mode. Figure 3.7 (c) and (d) show the bending

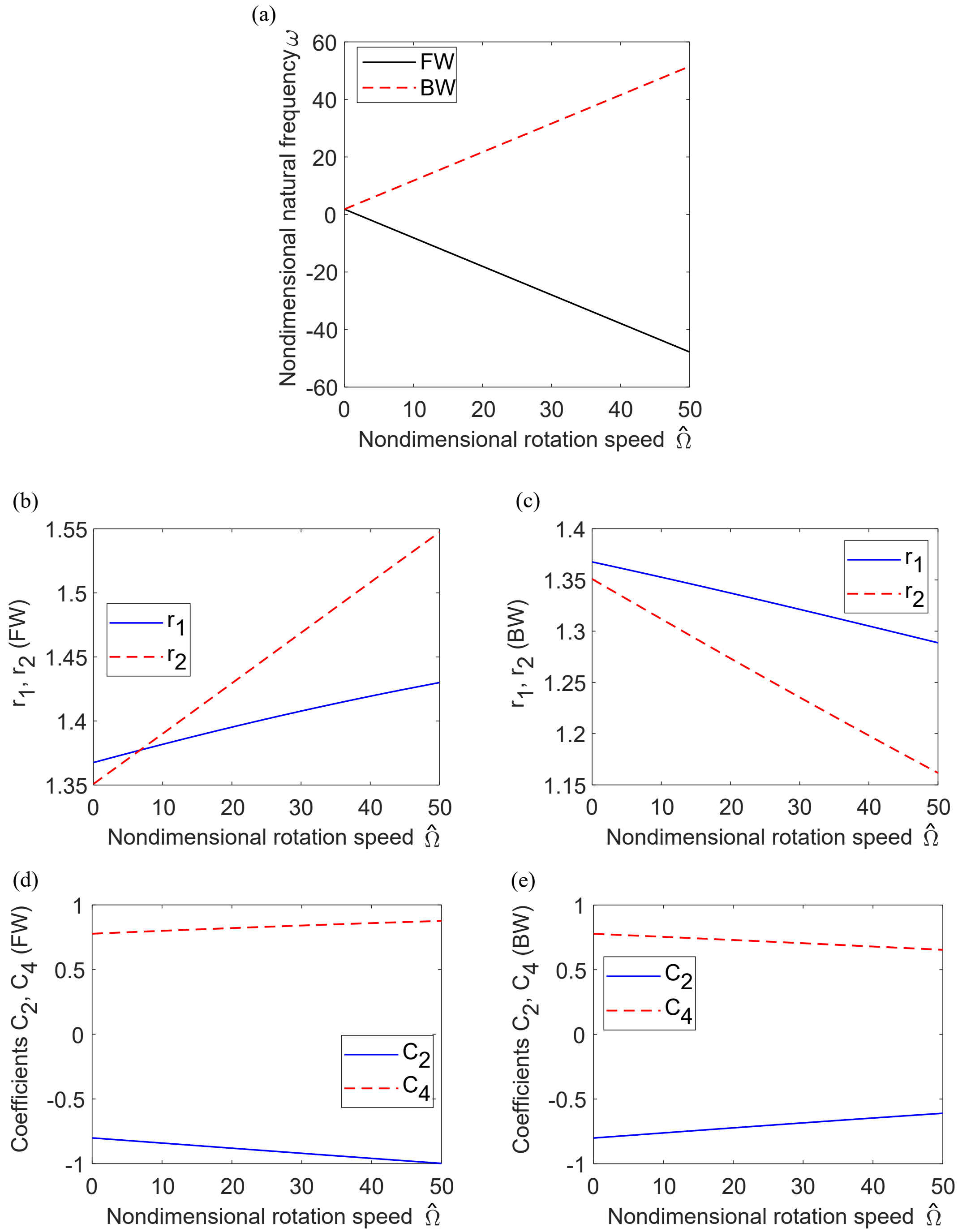

Figure 3.5: (a) Variation in the first mode natural frequencies for varying speed in the system with a tip mass. (b-e) variations in the determining coefficients for varying speeds. (b) and (d) corresponding to the forward (FW) orbit mode. (c) and (e) corresponding to the backward (BW) orbit mode.

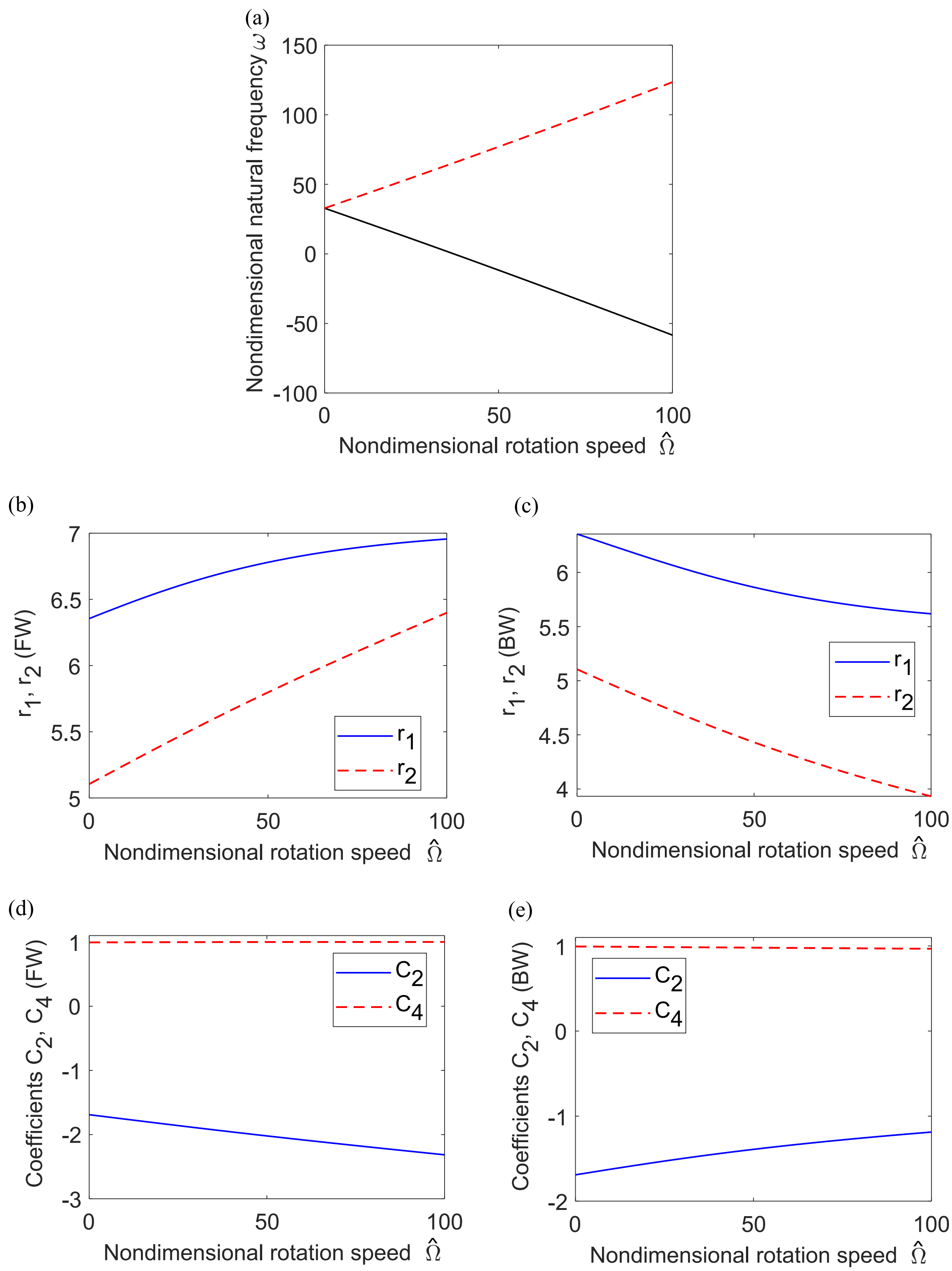

Figure 3.6: (a) Variation in the third mode natural frequencies for varying speeds in the system with a tip mass. (b-e) variations in the corresponding coefficients for varying speeds. (b) and (d) corresponding to the forward (FW) orbit mode. (c) and (e) corresponding to the backward (BW) orbit mode.

and rotational modal shapes for the third mode. As seen in these figures, the presence of a relatively large tip mass makes the mode shapes more sensitive to changes in rotation speed. This difference is more pronounced when comparing the mode shapes of the forward and backward orbit modes.

Figure 3.8 shows the effects of a relatively massive rigid tip body on the mode shapes for the first and third modes at zero speed. The first and third modes are selected as examples. Figure 3.8 (a) and (b) show the bending and rotational modal shapes for the first mode. Figure 3.8 (c) and (d) show the bending and rotational modal shapes for the third mode. The solid purple lines correspond to the system without any rigid tip body, and the dashed green lines correspond to the system with a rigid tip body. The general form of the mode shape corresponding to the first mode remains nearly unchanged between beams with and without a tip mass. By adding a rigid tip mass to the beam, some changes occur in the general form of the mode shapes corresponding to the third mode. Although their general form looks similar, the position of extremums along the beam span differs. For instance, the maximum peak in the bending deformations of the third mode occurs around $x_3 = 0.81$ and $x_3 = 0.67$ for the systems with and without a tip mass, respectively. The maximum peak in the rotational deformations of the third mode also occurs around $x_3 = 0.57$ and $x_3 = 0.45$ for the systems with and without a tip mass, respectively. The results indicate that the slopes of the mode shapes differ noticeably in both sign and magnitude across many regions.

3.4 Conclusion

Closed-form solutions are derived for spinning cantilever Timoshenko beams with a rigid body attached at its end. Both the beam and the rigid body are considered geometrically symmetric. The equations of motion are re-defined in the complex form to reduce the number of equations from four to two; that is, the order of equations decreases from

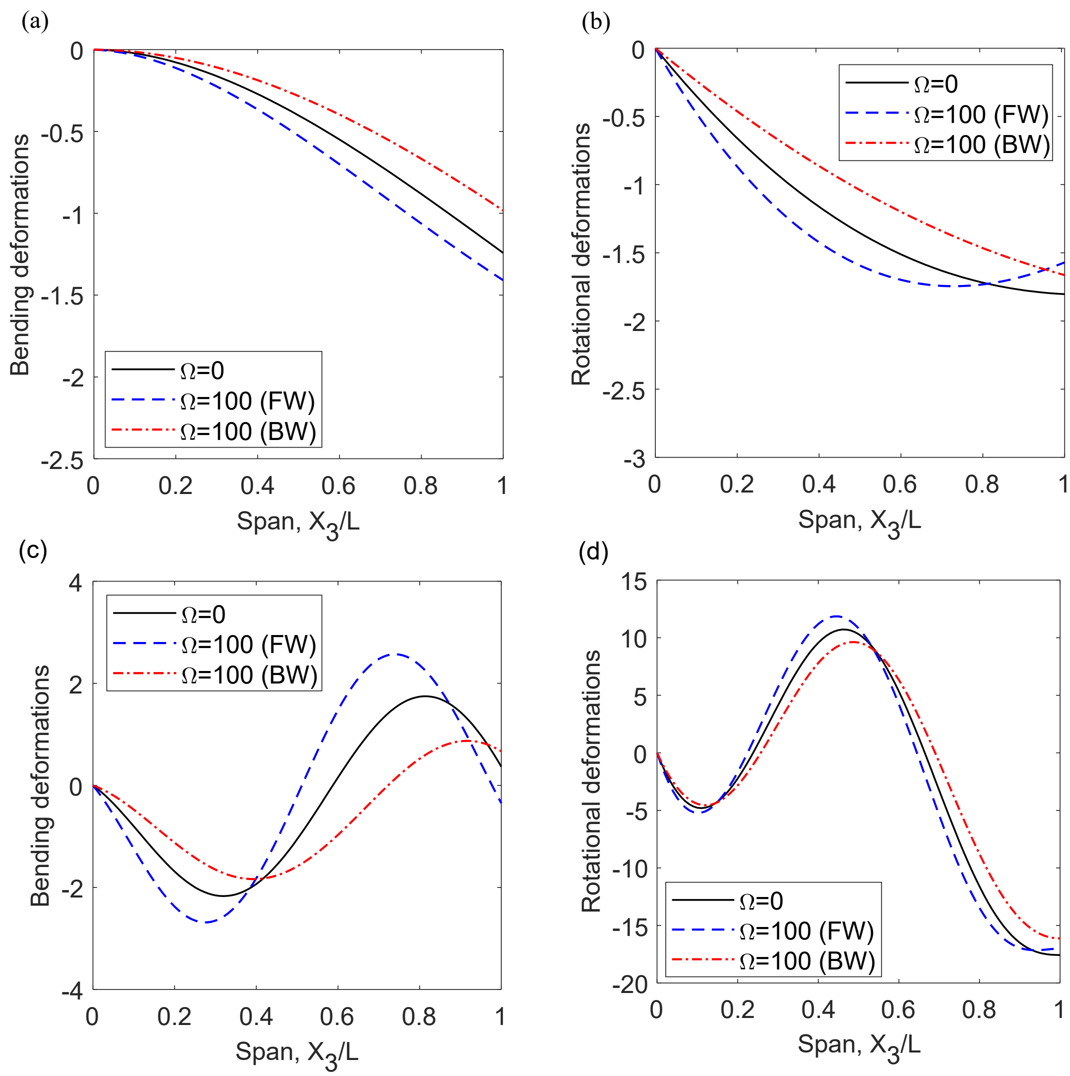

Figure 3.7: Bending and rotational mode shapes in the system with a tip mass for $\hat{\Omega} = 0$ and $\hat{\Omega} = 100$ (a-b) First mode. (b-c) Third mode. The solid black lines correspond to zero speed, the dashed blue lines correspond to forward modes in $\hat{\Omega} = 100$, and the dashed-dotted red lines correspond to backward modes in $\hat{\Omega} = 100$.

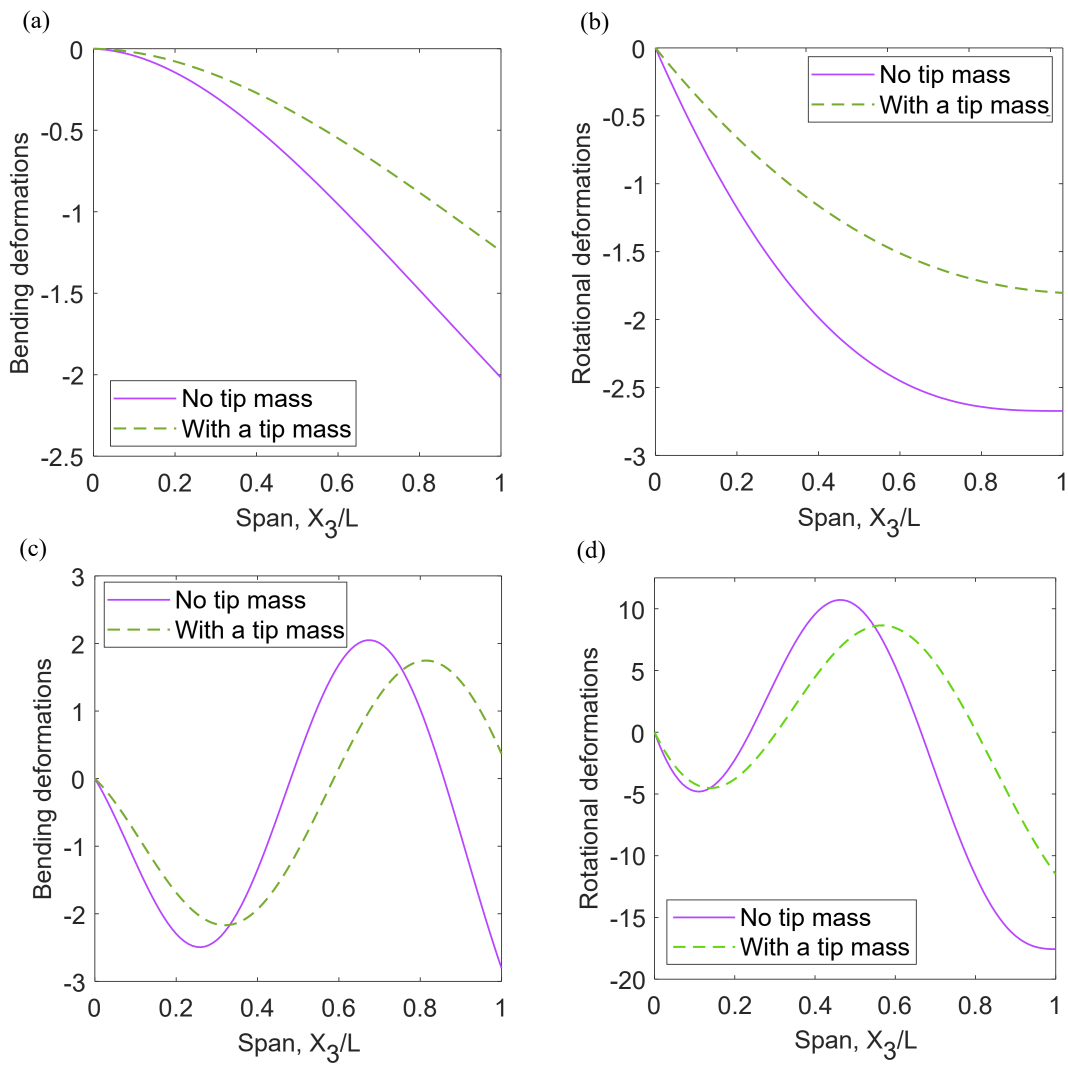

Figure 3.8: Mode shapes for the systems with and without a rigid tip body at zero speed ($\hat{\Omega} = 0$). (a-b) First mode. (b-c) Third mode. The solid purple lines correspond to the system with no tip mass. The dashed green lines correspond to the system with a tip mass.

four to two. The effects of the rigid tip body are applied through the natural boundary conditions. Natural frequencies and the coefficients of the mode shapes are calculated numerically. Complete agreements are observed between the results computed by the analytical closed-form solutions and the Galerkin method results using polynomial basis functions. Changes that occur in the mode shapes of higher modes are more significant than those of the first mode. These changes are also more fundamental when a rigid body is attached to the end of the beam. The closed-form solutions and the results presented in this chapter can be used to estimate fundamental frequencies in more complex systems and provide proper basis functions for discretization. They can also be employed in the analysis of similar systems with nonlinear behaviors.

CHAPTER FOUR

ANALYZING THE VIBRATIONS AND STABILITY OF THE SPINNING SYSTEM USING FINITE ELEMENT SIMULATIONS

4.1 Introduction

Continuum systems generally involve complexities arising from factors such as geometry, boundary conditions, material behavior, nonlinearity, and couplings. These complexities make it impossible to solve the problem using analytical methods. The Finite Element Method (FEM) is one of the most effective approaches for analyzing such complex continuum problems by discretizing its domain into smaller elements. This method employs variational principles and the Galerkin method to accurately approximate solutions of the governing partial differential equations. The approximated solution is calculated by minimizing the residual value in the weak form of the discretized equations. One of the primary applications of the finite element method is in modal analysis, which allows for evaluating the dynamic behaviors of complex systems, such as their natural frequencies, mode shapes, and damping properties. The finite element method has been used to study free vibrations in stationary Timoshenko beams under various working conditions [178–181]. Some studies have investigated vibrations in rotating beams along their perpendicular axis [182–184]. Software such as ANSYS and ABAQUS is a specialized computational tool designed to perform numerical simulations using the finite element method. Their advantages are ease of application and high accuracy. Finite element analysis has been widely employed in vibration and modal analysis for a wide range of dynamic systems [185–187].

In this chapter, the natural frequencies and mode shapes of the spinning cantilever with a rigid tip body are calculated using the finite element method performed in ANSYS. These results and mode shapes are compared with those from analytical modeling. Variations in the natural frequencies in the inertial coordinate system for both symmetric and asymmetric systems with varying rotation speeds are also investigated through finite element simulations. The natural frequencies computed in the inertial coordinate system are transformed into the co-rotational coordinate system to allow for the comparison with the results obtained by the analytical modeling. The simulation results are used to evaluate the validity of the results obtained from analytical modeling presented in the previous chapters.

4.2 Geometry and Material

The dynamic system, consisting of a cantilevered beam and rigid tip body, rotating about its longitudinal axis at a constant speed Ω, is depicted in Fig. 2.1. The length and the cross-sectional area of the beam are represented by L and A. The beam's material is isotropic elastic with density ρ, elastic modulus E, and shear modulus G.

The beam rotates at a constant speed Ω $\{\mathbf{i},\mathbf{j},\mathbf{k}\}$ about the beam neutral axis $\mathbf{E}_3 = \mathbf{k}$ (along the beam length). Two other perpendicular base vectors $\mathbf{E}_1$ and $\mathbf{E}_2$ are aligned with the principal axes of the cross-section. At the free end of the beam, a rigid body is placed along the $\mathbf{E}_3$ axis, whose mass center is offset by a distance of d from the beam end. A local body-fixed basis $\{\mathbf{e}_1,\mathbf{e}_2,\mathbf{e}_3\}$ is defined to determine the rotations of the rigid body relative to $\{\mathbf{E}_1,\mathbf{E}_2,\mathbf{E}_3\}$. $\mathbf{J} = J_{11}\mathbf{e}_1 \otimes \mathbf{e}_1 + J_{22}\mathbf{e}_2 \otimes \mathbf{e}_2 + J_{33}\mathbf{e}_3 \otimes \mathbf{e}_3$ denotes the mass moment of inertia of the rigid body with mass M about its mass center, consisting of three components J_{11}, J_{22}, J_{33} along the axes $\mathbf{e}_1$, $\mathbf{e}_2$, $\mathbf{e}_3$.

Two systems consisting of beams with tubular cross-sections and solid rigid bodies are studied. The cross-sections of the beam and the rigid body in the first system are square, which is called symmetric in this study. The inertial and stiffness properties in this system are identical in the two bending directions. On the other hand, the cross-sections of the beam and the rigid body in the second system, called asymmetric, are rectangular with unequal inertial and stiffness properties in the two bending directions. The geometric and material parameters of this beam-rigid body system are given in Table 2.1. The offset of the rigid body mass center from the beam's end is equivalent to $5mm$ as one-half of the rigid body's length d. The elastic and shear moduli of the tip mass are very large, about 10^5 times larger than those of the elastic beam.

The corresponding nondimensional parameters for the symmetric system are $\kappa = 201.1069$, $\mu = 0.001876$, $\alpha = 1$, $k_{13} = 0.4355$, $\eta = 0.5068$, $v_{11} = 0.00258875$, $v_{22} = 0.00258875$, $v_{33} = 0.00385782$, $\hat{d} = 0.0625$. The asymmetric system has nondimensional parameters $\alpha = 1.4860$, $v_{11} = 0.003299$, $v_{22} = 0.002144$, and $v_{33} = 0.004124$. The remaining nondimensional parameters are identical to those of the symmetric system.

4.3 Finite element mesh

To prepare the problem for processing, the continuous system is discretized into smaller elements by generating a mesh. The mesh size for the beam's elements is set to be 1 mm. Larger mesh sizes are applied to the rigid body's elements because it is almost rigid and does not have any elastic deflections. A visualization of the generated mesh for the asymmetric system is shown in Fig. 4.1.

The number of nodes in the symmetric system is 81 along the beam length, 12 along the width, and 12 along the height. The number of nodes in the asymmetric system is 81, 14, and 12 through the beam length, width, and height, respectively.

At $x_3 = 0$, the displacements along the axes $\mathbf{E}_1$, $\mathbf{E}_2$, and $\mathbf{E}_3$ and the rotations are considered zero. For spinning systems, only rotation about the axis E_3 is allowed.

4.4 Simulation results for the stationary systems

Numerical simulation is performed for the zero speed ($\Omega = 0$) The convergence of the results is checked by comparing them to those computed for smaller mesh sizes. The

(a) (b)

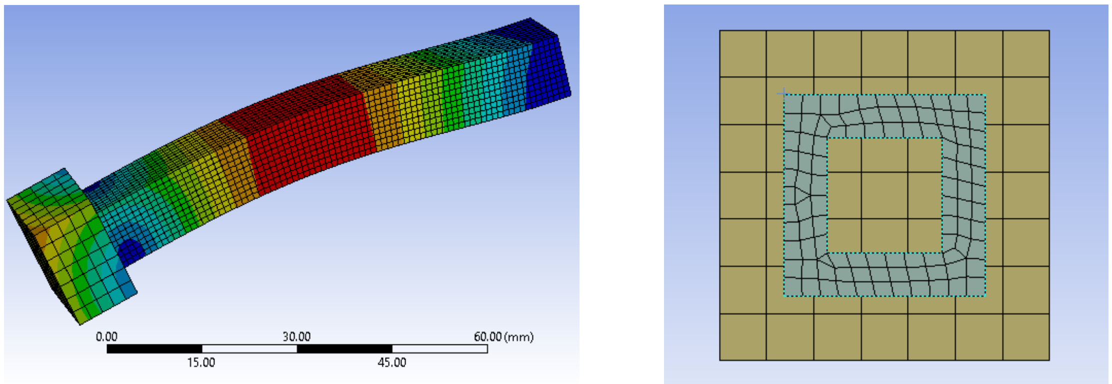

Figure 4.1: Picture of generated mesh for (a) side view, (b) back view

natural frequencies and mode shapes are calculated and compared with those of analytical modeling.

4.4.1 Natural frequencies

The first eight natural frequencies for the symmetric system, computed using finite element simulations, are given in Table 4.1. The dimensionless natural frequencies are provided using the relation $\bar{\omega} = \sqrt{\rho A L^4 / E I_{11}}\,\omega$ to be compared with the ones computed by the analytical modeling provided in another column of this table. Mode types are also determined in a column of this table to be distinguished. Each bending mode appears as a pair, whereas other modes are unique. Due to the symmetry of the beam cross-section, there are two sets of bending modes about the perpendicular axes X_1 and X_2 with exactly equal values of natural frequencies. It can be seen in this table that the torsional mode lies between the first and second bending modes in the simulation results, but they are not included in the analytical modeling. The axial mode exists between the second and third bending modes in the simulation results, while they are not included in this analytical modeling. The differences between the finite element simulation results and those of the Galerkin method are within 1, 3, and 5 percent for the first, second, and third bending modes, respectively.

Table 4.1: Natural frequencies computed by ANSYS simulation and analytical modeling for the symmetric system ($\Omega = 0$)

Mode number	Mode type	Frequency [Hz]	Nondimensional natural frequency ANSYS	Nondimensional natural frequency analytical modeling
1	1st Bending	809.3	1.8621	1.8476
2	1st Bending	809.4	1.8621	1.8476
3	1st Torsion	4758.3	10.9485	
4	2nd Bending	5708.5	13.1348	12.804
5	2nd Bending	5708.7	13.1352	12.804
6	1st Axial	10795.0	24.8385	
7	3rd Bending	14886.6	34.2530	32.826
8	3rd Bending	14886.6	34.2530	32.826

Similarly, a comparison of the first eight natural frequencies for the asymmetric system is also provided in Table 4.2. Each bending mode has two different natural frequencies in two perpendicular planes. The difference between the finite element simulation results and those of the Galerkin method is less than 5 percent for the first three bending modes. The agreement between two groups of values decreases in higher modes.

4.4.2 Mode shapes

Mode shapes of the bending, axial, and torsional modes calculated by finite element simulations are shown in Figs. 4.2. The second bending mode is shown in Fig. 4.2(a), while the first axial and torsional modes are shown in Figs. 4.2(b) and (c), respectively. The red regions on the beam correspond to the largest deformations, whereas the yellow and blue regions on the beam represent moderate and smallest deformations, respectively. The undeformed state of the axial mode in Fig. 4.2(b) is also displayed as a wire frame. As expected, the end of the beam has the largest deformations in the axial mode shape. The largest torsional mode deformations occur at locations farthest from the neutral axis.

Table 4.2: Natural frequencies computed by ANSYS simulation and analytical modeling for the asymmetric system ($\Omega = 0$)

Mode number	Mode type	Frequency [Hz]	Nondimensional natural frequency ANSYS	Nondimensional natural frequency analytical modeling
1	1st Bending	807.3	1.8621	1.8486
2	1st Bending	980.0	2.2553	2.2316
3	1st Torsion	4910.5	11.3009	
4	2nd Bending	5647.0	12.9957	12.8870
5	2nd Bending	6670.5	15.3511	14.7440
6	1st Axial	10795.0	24.8430	
7	3rd Bending	14604.9	33.6111	33.2226
8	3rd Bending	16848.9	38.7753	36.4074

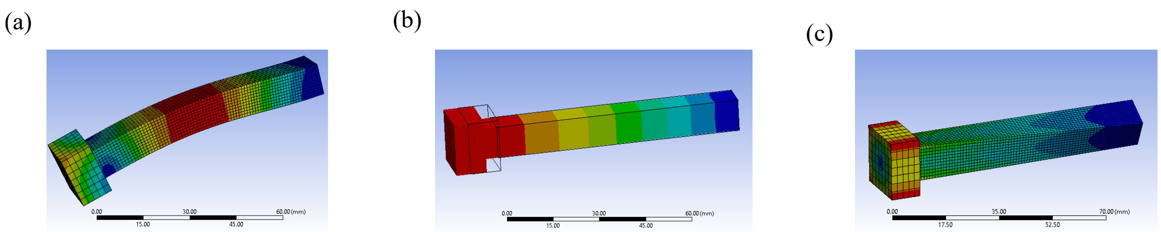

Figure 4.2: Visualization of the mode shapes for (a) bending mode, (b) axial mode, (c) torsional mode

The third and fourth bending mode shapes obtained by finite element simulations are illustrated in Figs. 4.3. The third and fourth bending mode shapes are shown in Fig. 4.3(a) and (b), respectively. The number of extrema seen in the bending mode shapes is typically one less than the mode number. The third mode in Fig. 4.3(a) shows two extrema, while the fourth mode in Fig. 4.3(b) shows three extrema.

Figures 4.4 makes a comparison between the boundary lines of the fourth bending mode shape calculated by the analytical modeling and finite element simulations. Deformations of the mode shapes are displayed at an exaggerated scale to make the differences more apparent. The boundary lines of the mode shapes from finite element simulations on the front face and midface of the beam are compared in Fig. 4.4(a). Solid

(a)

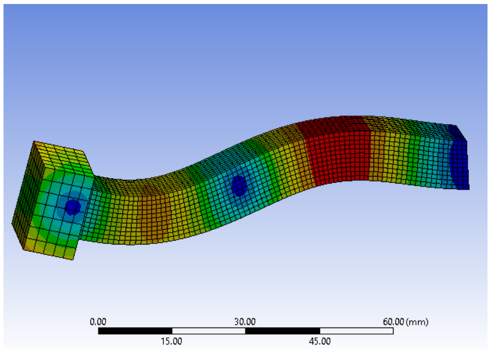

(b)

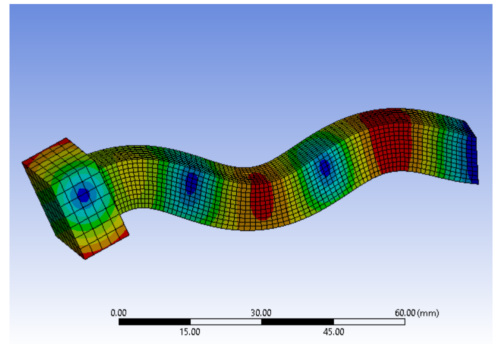

Figure 4.3: Visualization of bending mode shapes obtained by finite element simulations: (a) third bending mode, (b) fourth bending mode

blue lines correspond to the boundary lines on the frontal face. Dashed red lines correspond to the boundary lines on the midface. No meaningful differences are seen between the boundary lines of the mode shapes on the midface and front face. The boundary lines of the mode shapes computed by finite element simulation and analytical modeling are compared in Fig. 4.4(b). Solid green lines correspond to boundary lines determined by analytical modeling. Dashed red lines correspond to boundary lines determined by the finite element simulation on the midface. The analytical modeling is only able to calculate the neutral axis of the beam. The boundary lines of the mode shapes for the analytical modeling are estimated assuming a constant slope across the beam thickness. Mode shapes predicted by the analytical model are in close agreement with the finite element simulation results.

4.5 Simulation results for the rotating systems

Figure 4.5 shows variations in the system's natural frequencies for varying rotation speeds in the inertial coordinate. This diagram is known as the Campbell Diagram. Natural frequencies are calculated in the fixed (inertial) coordinate system. The boundary condition at the fixed end is assumed to permit free rotations around the X_3 axis, while the other directions are constrained. Figure 4.5(a) shows the variations for the system with a symmetric

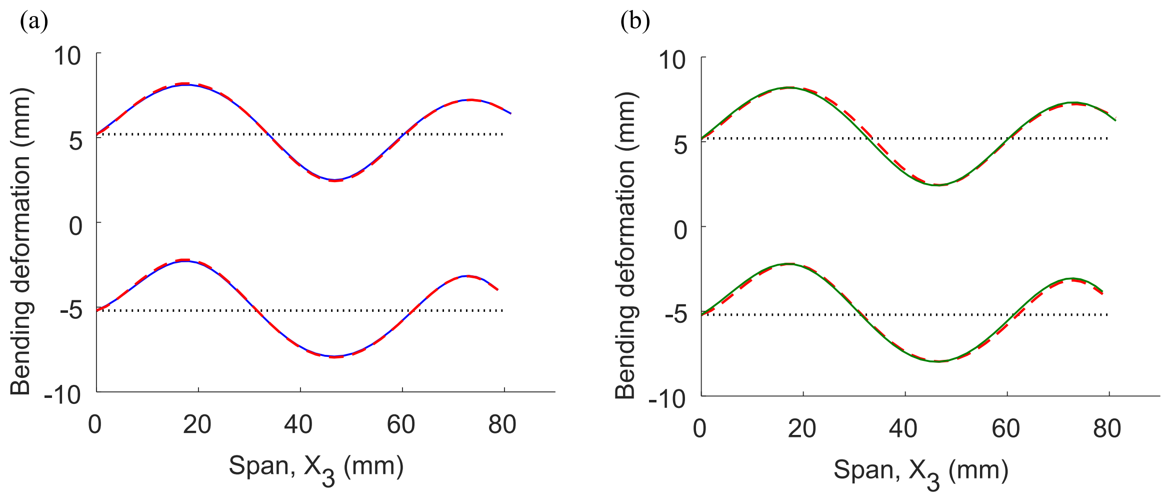

Figure 4.4: (a) Mode shapes boundary lines determined by the finite element simulations on the midface and front face. (b) Mode shapes boundary lines determined by the finite element simulation on the midface and analytical modeling. Solid blue lines in (a) correspond to the finite element simulation results on the frontal face. Dashed red lines correspond to the finite element simulation results on the midface. Solid green lines in (b) correspond to analytical modeling.

cross-section. In the symmetric system, the natural frequencies of only the bending modes are degenerate at zero speed, while the axial and torsional modes are unique. For nonzero speeds, the increasing (decreasing) natural frequencies correspond to the forward (backward) bending modes. In the Campbell diagram, because of the fixed coordinate system, critical speeds, shown by red circles, are determined by equating the natural frequency with the rotation speed ($\hat{\Omega} = \omega$). As the rotation speed increases, the natural frequency of the first torsional and axial modes increases and decreases, respectively. As seen in this figure, critical speeds determined by the intersections of the natural frequency curves and the line $\omega = \bar{\Omega}$ are not unique for each mode number. This is in contrast to the analytical modeling results.

Figure 4.5(b) shows the variations for the system with an asymmetric cross-section. In the asymmetric system, the natural frequencies of each pair of bending modes are distinct at zero speed. For nonzero speeds, the increasing natural frequencies located on the higher

Table 4.3: Nondimensional critical speeds calculated by ANSYS finite element simulation and the analytical modeling

Symmetric		Asymmetric	
finite element	Analytical modeling	finite element	Analytical modeling
1.8485	1.8600	1.8530	1.8600
1.8761	1.8600	2.2616	2.2538
12.2239	13.6598	12.5429	13.6598
14.2114	13.6598	15.9423	16.1033
30.2182	36.8036	31.2908	36.8036
40.4178	36.8036	42.9525	41.8150

branch correspond to the forward bending modes. For nonzero speeds, the decreasing natural frequencies located on the lower branch correspond to the backward bending modes. With increasing the rotation speeds, the natural frequency of the first torsional and axial modes increases and decreases, respectively.

Table 4.3 presents the critical speeds computed by the finite element simulations and analytical modeling for both symmetric and asymmetric systems. In the symmetric system, the values of critical speeds computed by analytical modeling fall between the values determined by the finite element simulation. Thus, these results can serve as a domain to estimate the critical speeds. In the asymmetric system, the values of critical speeds determined by the finite element simulation lie on either side of the values obtained by the analytical modeling. In other words, the bandwidth of the divergence instability is broader in the Campbell diagram than in the analytical modeling.

To compare the results from the finite element simulation with those from analytical modeling, they must be transformed from the inertial coordinate system into the co-rotational coordinate system. The natural frequencies transformed into the inertial coordinate system can be calculated by adding (subtracting) the value of the rotation speed $\hat{\Omega}$ to (from) the natural frequencies of the inertial coordinate system with backward (forward) orbits. Figure 4.6 shows the variations in the natural frequency for varying rotation speeds in

(a)

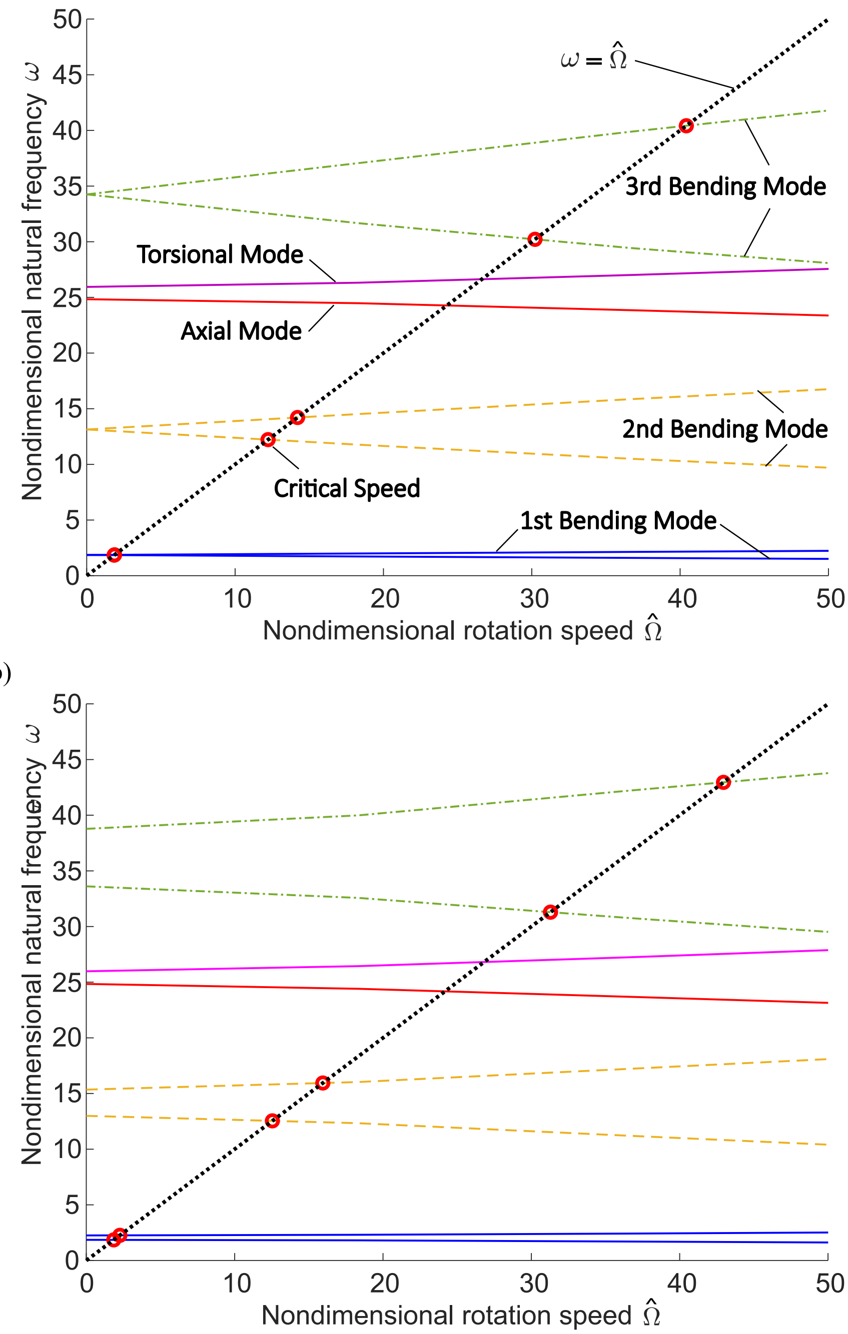

Figure 4.5: Variations in the natural frequencies for varying rotation speeds computed in the inertial coordinate. (a) symmetric cross-section, and (b) asymmetric cross-section.

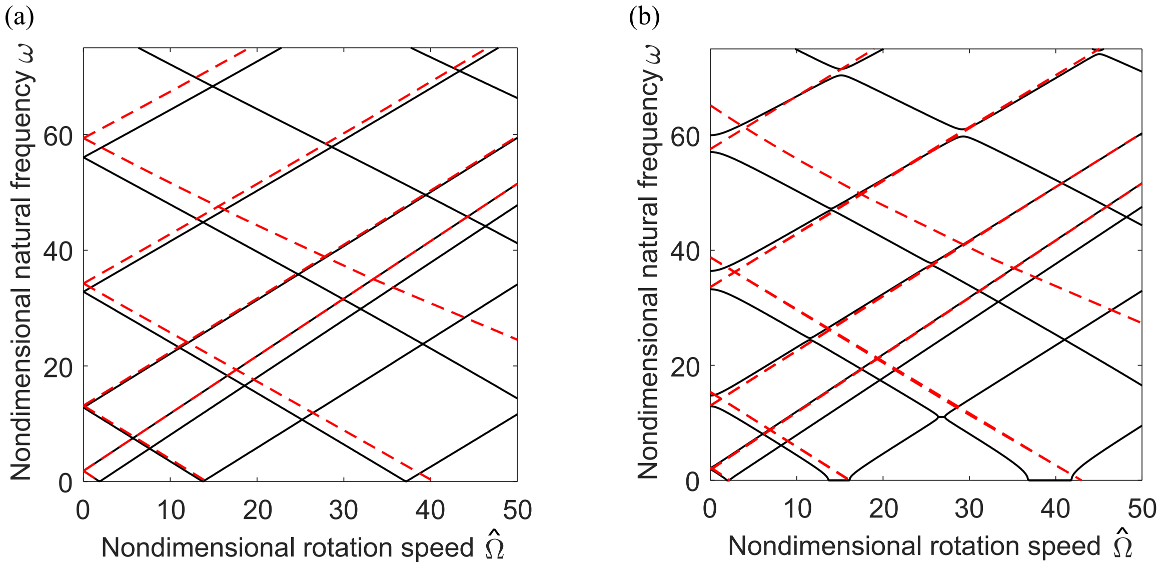

Figure 4.6: The natural frequencies versus rotation speeds in the inertial coordinate system. (a) symmetric geometry, and (b) asymmetric geometry. The solid black lines correspond to analytical modeling. The dashed red lines correspond to the finite element simulation results.

the co-rotational system. The solid black lines correspond to analytical modeling results. Dashed red lines correspond to the finite element simulation results transformed into the inertial coordinate system.

Figure 4.6(a) shows the natural frequencies versus speeds for the symmetric system. A close agreement is seen in the natural frequencies of the lower modes computed by analytical solution and finite element simulations. The agreement slightly decreases at higher modes and speeds. Figure 4.6(b) shows the natural frequencies versus speeds for the asymmetric system. Similarly, an agreement is seen in the natural frequencies of the lower modes, which decreases for higher modes. No veering interaction and flutter instabilities are observed. This disagreement emerges around the eigenvalues, where both forward and backward orbits exist across the beam span.

4.6 Conclusion

Modal analysis is performed using the finite element analysis for a spinning cantilever beam with a rigid body attached at its free end. The beam's cross-section is deemed moderately thick, leading to noticeable shear deformations. The natural frequencies and their corresponding mode shapes for symmetric and asymmetric systems are computed using finite element simulations. The results are then compared with those obtained by analytical modeling. In addition to the bending modes, axial and torsional modes are also modeled by the finite element simulations. A close agreement is seen in the boundary lines of the mode shapes drawn by the analytical modeling and the finite element simulation. Variations in the natural frequencies for varying rotation speeds are plotted using the finite element simulations and compared with the plots calculated by the analytical modeling. The critical speeds for the symmetric system determined in the Campbell diagram are not unique. Nevertheless, the critical speeds computed by the analytical modeling lie around these pairs of values computed by finite element simulations. The results are transformed from the inertial coordinate system to the co-rotational coordinate system for comparison. The transformed diagram shows a relatively good agreement with those of analytical modeling for lower modes, which diminishes in higher modes. However, flutter instabilities and veering interactions, where no consistent orbits exist along the beam span, were not modeled in the finite element simulations conducted in the inertial coordinate system.

CHAPTER FIVE

MODELING AND EQUILIBRIUM ANALYSIS OF CIRCULAR DIELECTRIC ELASTOMER ACTUATORS

5.1 Introduction

Circular dielectric elastomer membranes are used in a variety of advanced devices, such as adaptive lenses, stacked actuators, and capacitive sensors. In applications, accurate predictions of the voltage-induced deformations are necessary to ensure high performance, especially at large stretches. Precise modeling of large stretches in circular dielectric elastomer membranes depends on the adoption of proper hyperelastic formulations and sufficient understanding of their electro-mechanical interactions.

Deformations arising from the electromechanical coupling in circular dielectric elastomer membranes functioning as actuators have been widely studied [84, 91–94, 102]. Wissler et al. [93] employed Mooney-Rivlin [76], Ogden [78], and Yeoh [188] hyperelastic models to derive an analytical solution for the instantaneous response of a pre-stretched circular actuator. They also performed finite element simulations to investigate the time-dependent behaviors. A lumped-parameter inverse model for pre-strained circular dielectric elastomer actuators is proposed by Liang et al. [94] for efficient computations. Further studies are needed to understand equilibria at larger stretches and the influence of hyperelastic models to predict large-stretch deformations. An effective technique to improve large stretches in dielectric transducers is to produce a prestretch by applying an external load to the elastomer [94, 107]. This approach not only facilitates larger and more uniform stretches but also amplifies the electric field and allows the membrane to withstand much higher voltages.

A wide range of hyperelastic models have been proposed to predict large deformations in hyperelastic materials [74, 75, 77, 78]. Models such as Neo-Hookean [74] and Mooney-Rivlin [76] models are accurate for small to moderate stretches, while some other models, such as Ogden [78], Yeoh [188], and Gent [79] models, are designed to capture larger stretches. Among these models, the Gent hyperelastic formulation is widely used in dielectric elastomer membrane research related to acrylic elastomers. However, the Gent model does not have sufficient flexibility to accurately capture nonlinear stiffening stretches in diverse hyperelastic materials.

This chapter studies the nonlinear equilibrium responses of circular dielectric membranes subjected to a pre-stretch loading and varying electric potential employing analytical approaches and finite element simulations. Two models are investigated. In the first model, only the portion of the membrane is included. In the second model, both the inner active and outer passive regions are included. The pre-stretch tension is applied to the active region through the passive region, which is stretched and fixed at the outer boundary. The models are compared to the available experimental results obtained by a research team from the University of Dayton. With the help of finite element simulations, variations in stretches throughout the membrane body for two magnitudes of pre-stretch load are investigated. Furthermore, the capacity of several standard hyperelastic formulations to fit a given data set is examined.

5.2 Modeling

A schematic of a circular dielectric elastomer membrane is shown in Fig. 5.1. The undeformed and deformed membranes are shown by dashed (red) and solid (black) lines, respectively. The undeformed membrane is circular with the outer radius R_0 and thickness H_0. The membrane is pre-stretched by a constant, uniform radial load P before the electrical

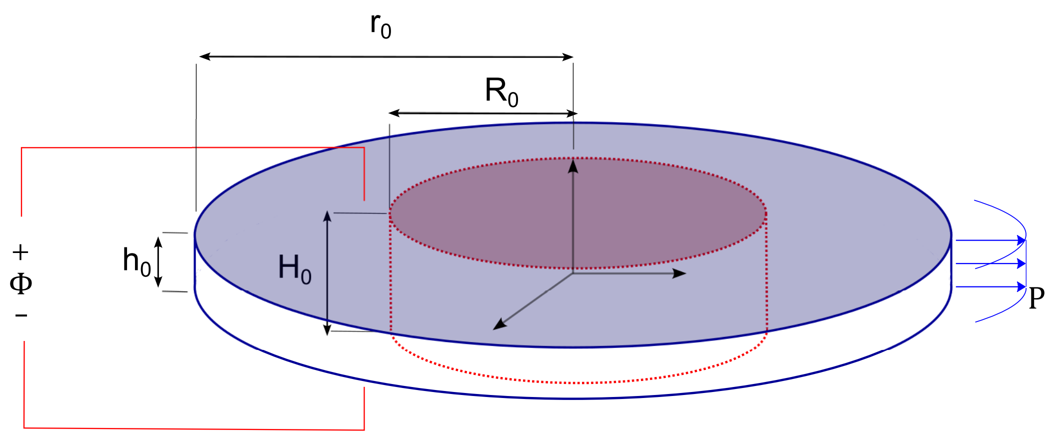

Figure 5.1: Schematic of a single active dielectric elastomer membrane subjected to radial prestretch tension. Dashed (red) lines represent the undeformed configuration, and solid (black) lines represent the deformed configuration.

activation, which allows very large stretches without failure by electrical breakdown. The radial load P is uniformly distributed on the outer circumferential surface of the membrane. The voltage Φ, applied through the thickness of the membrane, reduces the thickness to h_0 and expands the radius to r_0 through the Maxwell stress tensor.

The deformed membrane remains circular by the assumption of homogeneous deformations. The position of a material particle in the membrane before deformation is represented by $\mathbf{X} = R\mathbf{E}_r + X_3\mathbf{E}_3$. R and X_3 are the radial and axial coordinates, respectively, that satisfy $0 \leq R \leq R_0$ and $-H_0/2 \leq X_3 \leq H_0/2$. The position of a material particle after an axis-symmetric deformation at time t is $\mathbf{x} = r(R,t)\mathbf{E}_r + x_3(X_3,t)\mathbf{E}_3$. In the deformed membrane, the radial position $r(R,t) = R\lambda(t)$ and the axial position $x_3(X_3,t) = X_3\lambda^{-2}$ for assumed incompressible deformations are functions of the stretch $\lambda(t)$. Incompressibility, which is a common assumption for elastomers, enforces a constant volume in the membrane during deformation. The velocity vector of the particle $\dot{x}$, as the time derivatives of the particle position, is

$$\dot{\mathbf{x}} = R\dot{\lambda}\mathbf{E}_r - 2\lambda^{-3}\dot{\lambda}X_3\mathbf{E}_3 \tag{5.1}$$

where $(\dot{\ })$ denotes derivatives of the variable with respect to time. The kinetic energy K over the undeformed volume of the membrane V_0 with the mass density of ρ is obtained by substituting (5.1) into $K = 1/2\int_V \rho\dot{\mathbf{x}}\cdot\dot{\mathbf{x}}\mathrm{d}V_0$. The kinetic energy is

$$K = \frac{1}{4}\pi\rho R_0^4 H_0\left[1+\frac{2}{3}\left(\frac{H_0}{R_0}\right)^2\lambda^{-6}\right]\dot{\lambda}^2 \tag{5.2}$$

The free energy density in the membrane caused by the electrical field is $u_e = D_3^2/2\varepsilon$, where $D_3 = -\varepsilon\Phi/h_0$ represents the electric displacement field through the membrane thickness. Φ is the applied electric potential. The material's permittivity $\varepsilon = \varepsilon_r\varepsilon_0$, where ε_r denotes the relative permittivity and ε_0 is vacuum permittivity. To derive the mechanical part of the free energy density $u_m(\lambda)$, the nonlinear strain stiffening behaviors of the elastomer at large stretches need to be captured by hyperelastic models. Integrating the total free energy density, which is considered constant throughout the body, over the undeformed volume gives the total free energy

$$U = \pi\rho R_0^2\left[\frac{1}{2}\frac{\varepsilon}{H_0^2}\Phi^2\lambda^4 + u_m(\lambda)\right] \tag{5.3}$$

The constant radial traction $P/2\pi h_0 r_0$ applies an in-plane pre-stretch on the outer circumferential surface of the deformed membrane $2\pi h_0 r_0$. The product of the distributed tension force and the virtual displacement δr_0 produces a non-conservative mechanical virtual work $\delta W^{(nc)} = PR_0\delta\lambda$, where δr_0 represents the virtual derivatives. A non-conservative virtual work also results from the variation of voltage through the membrane thickness over time as $\delta W^{(nc)} = \Phi\delta q$. δq is the virtual charge on the top electrode. A uniform charge is distributed across the top electrode, equal to $q = \pi\varepsilon R_0^2/H_0\Phi\lambda^4$ The total non-conservative work is derived as

$$\delta W^{(nc)} = \left(PR_0 + 4\pi\varepsilon\frac{R_0^2}{H_0}\Phi\lambda^3\right)\delta\lambda \tag{5.4}$$

Hamilton's principle $\int_{t_0}^{t}[\delta K - \delta U + \delta W] = 0$ is used to derive the governing equations of motion for the dielectric membrane as follows

$$\frac{1}{2}\pi\rho R_0^4 H_0\left[1+\frac{2}{3}\left(\frac{R_0}{H_0}\right)^2\lambda^{-6}\right]\ddot{\lambda} - \pi\rho R_0^2 H_0^4\lambda^{-7}\dot{\lambda}^2 + \pi R_0^2 H_0\frac{\partial u_m}{\partial\lambda} - 2\pi\varepsilon\frac{R_0^2}{H_0}\Phi^2\lambda^3 = PR_0 \tag{5.5}$$

Non-dimensional parameters are introduced as

$$\tau = \frac{1}{R_0}\sqrt{\frac{\mu}{\rho}}t, \quad \eta = \frac{H_0}{R_0}, \quad \phi = \sqrt{\frac{\varepsilon}{\mu}}\frac{\Phi}{H_0}, \quad \chi = \frac{P}{2\pi\mu H_0 R_0}, \quad \hat{u}_m = \frac{u_m}{\mu} \tag{5.6}$$

where μ is the small-stretch shear modulus. Substituting these nondimensional parameters into Eq. (5.5) gives the nondimensional equations of motion

$$\left[1+\frac{2}{3}\left(\frac{R_0}{H_0}\right)^2\lambda^{-6}\right]\ddot{\lambda} - 2\eta^2\lambda^{-7}\dot{\lambda}^2 + 2\frac{\partial\hat{u}_m}{\partial\lambda} - 4\phi^2\lambda^3 = 4\chi \tag{5.7}$$

The overdot $\dot{(\ )} = \mathrm{d}(\ )/\mathrm{d}\tau$ represents nondimensional time differentiation here and in the remainder of the chapter. $\partial\hat{u}_m/\partial\lambda$ is called the material function, which is associated with the material's stiffness. The inertia terms include the derivatives of the stretch with respect to time $(\ddot{\lambda}, \dot{\lambda})$. Terms containing χ and $\phi^2\lambda^3$ are associated with the pre-stretch and electro-elastic coupling. The equilibria are determined from the equations of motion in Eq. (5.7) with vanishing time derivatives of stretch

$$\frac{\partial \hat{u}_m}{\partial \Lambda} - 2\phi^2\Lambda^3 - 2\chi = 0 \tag{5.8}$$

where Λ denotes the induced stretches under the equilibrium condition. A wide range of hyperelastic material models have been introduced to approximate the mechanical free energy density for various types of hyperelastic materials. In this regard, multiple material functions are derived from the proposed hyperelastic models. The mechanical free energy density for larger stretches depends on the invariants of the deformation tensors. For isotropic materials, the mechanical free energy density u_m is generally defined as a function of the invariants of the right Cauchy–Green deformation tensor $\mathbf{C} = \mathbf{F}^T\mathbf{F}$, where $\mathbf{F} = \partial\mathbf{x}/\partial\mathbf{X} = \Lambda\mathbf{E}_r \otimes \mathbf{E}_r + \Lambda\mathbf{E}_\theta \otimes \mathbf{E}_\theta + \Lambda^{-2}\mathbf{E}_3 \otimes \mathbf{E}_3$ is the deformation gradient. The invariants are as follows

$$\begin{aligned} I_1 &= \mathrm{tr}(\mathbf{C}) = \Lambda_1^2 + \Lambda_2^2 + \Lambda_3^2, \\ I_2 &= \frac{1}{2}\left[(\mathrm{tr}(\mathbf{C}))^2 - \mathrm{tr}(\mathbf{C}^2)\right] = \Lambda_1^2\Lambda_2^2 + \Lambda_1^2\Lambda_3^2 + \Lambda_2^2\Lambda_3^2, \\ I_3 &= \det(\mathbf{C}) = \Lambda_1^2\Lambda_2^2\Lambda_3^2 \end{aligned} \tag{5.9}$$

where $\Lambda_1 = \Lambda$, $\Lambda_2 = \Lambda$, and $\Lambda_3 = \Lambda^{-2}$ are the principal stretches, computed from the square roots of the eigenvalues of the right Cauchy-Green deformation tensor $\mathbf{C}$. For incompressible materials, the third invariant $I_3 = 1$. In this regard, two invariants I_1 and I_2 are typically employed in the material models. For compressible material material deformations of the membrane, Λ_1, Λ_2, and Λ_3 correspond to radial stretch Λ_r, circumferential stretch Λ_θ, axial stretch Λ_3. In the next section, we investigate several widely used hyperelastic models.

5.2.1 Material models

The Neo-Hookean model [74] is considered one of the simplest hyperelastic models, which is capable of capturing nonlinear deformations up to moderately large stretches. For incompressible materials, the mathematical expression of the mechanical free energy density for the Neo-Hookean model is introduced as

$$u_m = \frac{\mu}{2}\left(I_1 - 3\right) \tag{5.10}$$

where μ denotes the small-stretch shear modulus. The second invariant I_2 is excluded from the energy density proposed for the Neo-Hookean model. The Neo-Hookean material function is obtained by substituting Eq. (5.10) into $\partial \hat{u}_m / \partial \Lambda$

$$\frac{\partial \hat{u}_m}{\partial \Lambda} = 2\left(\Lambda - \Lambda^{-5}\right) \tag{5.11}$$

where Λ is used to represent the first radial stretch Λ_r.

The mechanical free energy density function in the Mooney-Rivlin model [75] is defined as a linear combination of two invariants, I_1 and I_2 as follows

$$u_m = C_1\left(I_1 - 3\right) + C_2\left(I_2 - 3\right) \tag{5.12}$$

Satisfying the condition of consistent small stretch shear modulus involves $C_1 + C_2 = \mu/2$. Using two terms allows this model to capture nonlinearities in both uniaxial and biaxial loading more effectively, providing an accurate approximation for small to moderate stretches. Substituting Eq. (5.12) into $\partial \hat{u}_m / \partial \Lambda$ gives

$$\frac{\partial \hat{u}_m}{\partial \Lambda} = 2\xi_1\left(\Lambda - \Lambda^{-5}\right) + 2\xi_2\left(\Lambda^3 - \Lambda^{-3}\right) \tag{5.13}$$

where ξ_1 and ξ_2 are dimensionless parameters with the condition $\xi_1 + \xi_2 = 1/2$.

The Gent-Thomas model was proposed in 1958 by A. N. Gent and A. G. Thomas [189] following the Mooney-Rivlin model, whose mechanical energy density is a linear function of the first invariant I_1 and a logarithmic function of the second invariant I_2 as follows

$$u_m = C_1 (I_1 - 3) + C_2 \ln\left(\frac{I_2}{3}\right) \tag{5.14}$$

Differentiating the energy density with respect to the stretch under the small shear consistency $2C_1 + 2C_2/3 = \mu$ or $2\xi_1 + 2\xi_2/3 = 1$ yields the material function as

$$\frac{\partial \hat{u}_m}{\partial \Lambda} = 4\left(\Lambda - \Lambda^{-5}\right) + 4\xi_2 \frac{\Lambda^3 - \Lambda^{-3}}{\Lambda^4 - 2\Lambda^{-2}} \tag{5.15}$$

The Yeoh hyperelastic model is introduced to capture nonlinear strain-stiffening stretches in uniaxial tensions. The mechanical free energy density of the Yeoh model [188] is defined as a polynomial function of only the first invariant I_1, given by

$$u_m = \sum_{i=1}^{N} C_i (I_1 - 3)^i \tag{5.16}$$

For small shear modulus consistency, $C_1 = \mu/2$. The material function for the Yeoh model is obtained as

$$\frac{\partial \hat{u}_m}{\partial \Lambda} = 2\sum_{i=1}^{N} i\xi_i \left(2\Lambda^2 - \Lambda^{-4} - 3\right)^{i-1} \left(\Lambda - \Lambda^{-5}\right) \tag{5.17}$$

where $\xi_1 = 1/2$.

To capture the nonlinear elastic behavior of large stretches in materials such as rubber, soft polymers, and biological tissues, the Ogden hyperelastic model was developed by Raymond Ogden [78] in 1972. The mechanical free energy density in the Ogden model is defined in terms of the principal stretches as follows

$$u_m = \sum_{i=1}^{N} \frac{2\mu_i}{\alpha_i} \left(\Lambda_1^{\alpha_i} + \Lambda_2^{\alpha_i} + \Lambda_3^{\alpha_i} - 3 \right) \tag{5.18}$$

The consistent small stretch shear modulus entails $\sum_{i=1}^{N} \mu_i \alpha_i = \mu$. The material function for the Ogden hyperelastic model is given by

$$\frac{\partial \hat{u}_m}{\partial \Lambda} = \sum_{i=1}^{N} \frac{4\mu_i}{\mu} \left(\Lambda^{\alpha_i - 1} - \Lambda^{-2\alpha_i - 1} \right) \tag{5.19}$$

The Gent hyperelastic model [79] is developed to capture strain-stiffening effects by incorporating the limiting stretch parameter J_m. The mechanical free energy density for the Gent model is

$$u_m = \frac{\mu J_m}{2} \ln \left(1 - \frac{I_1 - 3}{J_m} \right) \tag{5.20}$$

An accurate approximation is achieved in this model with just two parameters, the shear modulus μ and the limiting stretch parameter J_m.

The material function for the Gent hyperelastic model is derived as

$$\frac{\partial \hat{u}_m}{\partial \Lambda} = 2 \frac{\Lambda - \Lambda^{-5}}{1 - \frac{2\Lambda^2 - \Lambda^{-4} - 3}{J_m}} \tag{5.21}$$

To improve flexibility in fitting experimental data and capture the biaxial and shear deformations, the Gent-Gent hyperelastic model was developed by Pucci and Saccomandi [190] as an extension of the classic Gent model. It incorporates both the first and second invariants I_1 and I_2 in the mechanical free energy density function, given by

$$u_m = \frac{C_1 J_m}{2} \ln \left(1 - \frac{I_1 - 3}{J_m} \right) + C_2 \ln \left(\frac{I_2}{3} \right) \tag{5.22}$$

The material function with the small shear consistency requirement $C_1 + 2C_2/3 = \mu$ ($\xi_1 + 2\xi_2/3 = 1$) is also derived in the same way as

$$\frac{\partial \hat{u}_m}{\partial \Lambda} = 2\xi_1 \frac{\Lambda - \Lambda^{-5}}{1 - \frac{2\Lambda^2 - \Lambda^{-4} - 3}{J_m}} + 4\xi_2 \frac{\Lambda^3 - \Lambda^{-3}}{\Lambda^4 - 2\Lambda^{-2}} \tag{5.23}$$

The Lopez-Pamies model [80] is another advanced model to capture nonlinear strain-stiffening deformations with reliable precision using only the first invariant I_1. The mechanical free energy density for this model is

$$u_m = \sum_{i=1}^{N} \frac{3^{1-\alpha_i}}{2\alpha_i} \mu_i \left(I_1^{\alpha_i} - 3^{\alpha_i} \right) \tag{5.24}$$

The material function for the Lopez-Pamies model satisfying the constraint $\sum_{i=1}^{N} \mu_i = \mu$ is

$$\frac{\partial \hat{u}_m}{\partial \Lambda} = 2 \sum_{i=1}^{N} 3^{1-\alpha_i} \frac{\mu_k}{\mu} \left(2\Lambda^2 - \Lambda^{-4} \right)^{\alpha_i - 1} \left(\Lambda - \Lambda^{-5} \right) \tag{5.25}$$

5.3 Data-Fitting

The application of hyperelastic models involves determining the model parameters by fitting their predicted deformation response curve to the experimental data. The data-fitting depends on the characteristics of the data and the selected model. Hence, the size and distribution of the data across different stretch magnitudes determine the model parameters and the resulting stiffness–stretch curve. The Least Squares method is employed in this study to compute the parameters through the data-fitting process. In this regard, the equilibrium equation is deemed equal to a small-value residual Res as follows

$$\frac{\partial \hat{u}_m}{\partial \Lambda} - 2\phi^2 \Lambda^3 - 2\chi = \text{Res} \tag{5.26}$$

The parameters are determined by numerically minimizing the sum of squared residuals across all data points $\sum_1^n (\text{Res})^2$, where n denotes the number of data points.

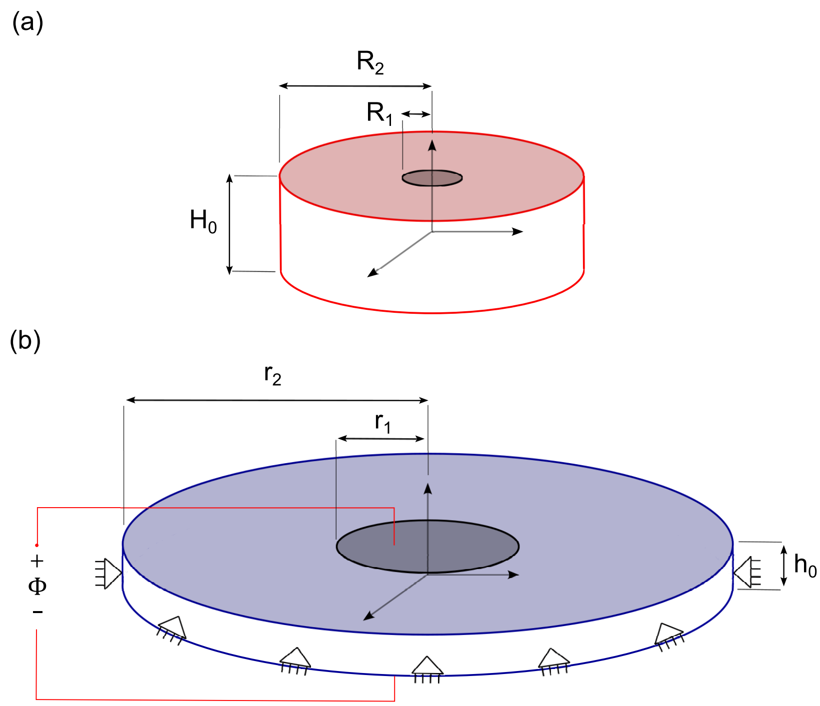

Figure 5.2: Schematic of a circular dielectric elastomer membrane, consisting of active (grayed) and passive (shaded) regions. The membrane is shown in its (a) undeformed and (b) deformed configurations. R_1 and R_2 are radii of the active and passive regions

5.4 Hybrid actuator model

In the hybrid model, the pre-stretch traction is applied through an intermediate inactive body, stretched and fixed at a predefined stretch value on a circular fixture. In this regard, the membrane is divided into active and passive regions, shown in Fig. 5.2. The schematics of the hybrid actuator before and after pre-stretching are shown in Figs. 5.2 (a) and (b), respectively. The electric potential is only applied on the smaller circular region at the center of the membrane, called the active region. In other words, the passive region is not exposed to an electric potential. The radii of this region in undeformed and deformed conditions are R_1 and r_1. The radii of the entire membrane in undeformed and deformed conditions are R_2 and r_2.

5.5 Finite Element simulation

Finite element analysis is employed in this section to numerically solve the coupled electro-mechanical equations with high accuracy. The finite element method can be applied to complex nonlinear equations, geometries, and boundary conditions, and also allows for the investigation of local behaviors.

5.5.1 Electromechanical governing equations

In the finite element analysis, the governing equations are defined in continuum formulations. In this regard, the mechanical equilibrium equation is

$$\boldsymbol{\nabla} \cdot (\boldsymbol{\sigma}_{\text{mech}} + \boldsymbol{\sigma}_{\text{elec}}) + \mathbf{f}_v = \mathbf{0} \tag{5.27}$$

where $\boldsymbol{\sigma}_{\text{mech}}$ and $\boldsymbol{\sigma}_{\text{elec}}$ are mechanical and Maxwell (electric) spatial Cauchy stresses tensor, respectively, and $\mathbf{f}_v$ is the mechanical body force per unit mass. $\boldsymbol{\nabla} = \mathbf{E}_r \frac{\partial}{\partial r} + \mathbf{E}_\theta \frac{1}{r} \frac{\partial}{\partial \theta} + \mathbf{E}_3 \frac{\partial}{\partial z}$ is a vector differential operator in cylindrical coordinates. The dot product $(\cdot)$ of the vector differential operator and the stress tensor $\boldsymbol{\nabla} \cdot \boldsymbol{\sigma}$ represents the divergence of the stress tensor $\boldsymbol{\sigma}$. The mechanical Cauchy stress tensor can be expressed as a function of the deformation gradient $\mathbf{F}$ and Lagrangian Green strain $\mathbf{e}$ as follows

$$\boldsymbol{\sigma}_{\text{mech}} = \frac{1}{J} \mathbf{F} \frac{\partial u_m}{\partial \mathbf{e}} \mathbf{F}^T \tag{5.28}$$

$J = \det(\mathbf{F})$ is the elastic volume ratio $J = \det(\mathbf{F})$ and the Lagrangian Green strain $\mathbf{e} = \frac{1}{2}(\mathbf{C} - \mathbf{I})$.

For compressible materials, the strain energy density function u_m is split into isochoric u_{iso} and volumetric u_{vol} parts as

$$u_m = u_{iso}(\mathbf{C}) + u_{vol}(J) \tag{5.29}$$

The isochoric term u_{iso}, which is discussed earlier, is a function of the Cauchy-Green deformation tensor $\mathbf{C}$. The volumetric term in a hyperelastic material represents the portion of strain energy that arises solely from volume changes (dilatation). The quadratic volumetric strain energy density, defined as a function of the elastic volume ratio J is

$$u_{vol}(J) = \frac{\kappa}{2}(J-1)^2 \tag{5.30}$$

The volumetric term vanishes when $J = 1$ in incompressible materials. The spatial Maxwell stress tensor as a function of the electric field $\mathbf{E}$ is

$$\boldsymbol{\sigma}_{\text{elect}} = \varepsilon \mathbf{E} \otimes \mathbf{E} - \frac{1}{2}\varepsilon (\mathbf{E} \cdot \mathbf{E}) \mathbf{I} \tag{5.31}$$

where $\mathbf{I}$ is the identity tensor. The electric field equation from Gauss's Law is

$$\boldsymbol{\nabla} \cdot \mathbf{D} = \rho_v \tag{5.32}$$

where ρ_v is the free charge density. Combining the electric displacement $\mathbf{D} = \varepsilon \mathbf{E}$ and field $\mathbf{E} = -\boldsymbol{\nabla}\Phi$ with Eq. (5.32) yields the electric governing equation

$$\boldsymbol{\nabla} \cdot (\varepsilon \boldsymbol{\nabla}\Phi) = -\rho_v \tag{5.33}$$

The stretch and electric field are calculated numerically by solving the coupled electric and mechanical governing equations (5.33) and (5.27) for a given set of boundary conditions and applied electric potentials. Stretch tensors are determined from the calculated deformations. The simulation results also illustrate the distribution of the electric field.

(a) (b)

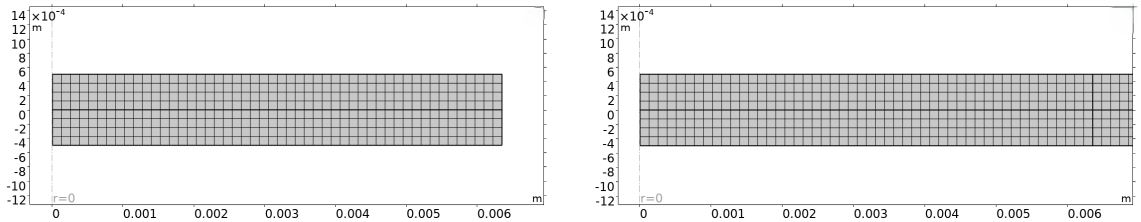

Figure 5.3: The finite element meshes used in the analysis of the circular dielectric elastomer membrane for (a) the single active membrane model and (b) the hybrid active-passive membrane model. Active region, interface, and the boundary of the passive region are shown in (b).

5.5.2 Geometry and mesh structure

The width of the undeformed membrane $H_0 = 1$ mm. Regardless of the pre-stretch magnitudes, the radius of the active region in the membrane after pre-stretch is R = 12.7 mm (0.5 in). The outer radius of the passive region is 60.96 mm (2.4 in). The radius of the undeformed membrane can be determined from the relation R/Λ_0. For example, for the pre-stretch $\Lambda_0 = 2$, the radius of the undeformed membrane is $12.7/2 = 6.35$ mm (0.25 in). For the pre-stretch $\Lambda_0 = 1.2$, the radius of the undeformed membrane is $12.7/1.2 = 10.58$ mm (0.4167 in). Due to the membrane's axisymmetry, the simulation can be conducted using a two-dimensional axisymmetric model. This only requires modeling the cross-section defined by the membrane's radius and thickness. The radial centerline of the membrane is constrained to have no displacement at all points along the axial axis X_3. The mesh distributions for both the single active and hybrid models are shown in Fig. 5.3. There are six elements through the membrane's thickness. The number of elements in each dimension for both models is determined to produce square elements. Thus, the length of each side of the elements is roughly 0.125 mm. In the hybrid case, the total radius of the membrane after pre-stretching is 4.8 in, with 0.5 in assigned to the active region. The size of the active region remains the same in both the single active and hybrid models.

5.5.3 Material properties

A highly-stretchable acrylic elastomer VHB 4910 with density $\rho = 590\ \text{kg/m}^3$ is selected for this simulation. The Gent hyperelastic material model with the small-stretch shear modulus $\mu = 16.92$ kPa and the limiting stretch $J = 138.8$ for this elastomer is used from Ref. [83]. A pre-stretch is produced by a constant radial tensile load P, evenly applied on the circumferential surface of the membrane. The value of the mechanical load is determined from the analytical model in Eq. (5.8) using the Gent mechanical model in Eq. (5.21). It has been demonstrated that this approach accurately produces the specified amount of pre-stretch in the finite element model. As an example, the radial loads are determined $P = 0.541$ N for pre-stretch $\Lambda_0 = 1.2$ and $P = 1.379$ N for pre-stretch $\Lambda_0 = 2$.

The relative dielectric permittivity of the dielectric membrane for VHB 4910 is $\varepsilon_r = 4.14$, which is assumed to be almost independent of deformations [83]. Many dielectric elastomers, such as VHB materials, show insignificant changes in ε_r under moderate stretches. The vacuum permittivity is $\varepsilon_0 = 8.854 \times 10^{-12}$ F/m. The electric potential Φ is applied to the upper circular surface, and the bottom surface is electrically grounded. A wide range of potentials is analyzed to get a complete understanding of the large stretch equilibrium behavior.

5.6 Analytical modeling results

Obtaining the analytical results for a given membrane elastomer involves determining the parameters of the hyperelastic material function. The selection of the appropriate material model depends on the material properties of the selected elastomer and the operating conditions. The corresponding material parameters specific to each model are determined using data-fitting or optimization techniques.

5.6.1 Equilibrium stretch results

The equilibrium solutions are calculated numerically from Eq. (5.8) for a given material model and its corresponding material parameters. The curve of the equilibrium stretch computed for varying applied electric potentials differs with changes in the chosen material model and specified parameters. The Gent hyperelastic model effectively captures the strain-stiffening of VHB elastomers under large deformations using only two parameters [191]. Hence, this model is used as a benchmark for comparing the properties of other hyperelastic models analyzed in this work.

Figure 5.4 presents the equilibrium stretch using the Gent hyperelastic model [79] for varying electric potentials, along with the corresponding values of the material function versus stretch for pre-stretch $\Lambda_0 = 1.283$ under tensile load $\chi = 1$. Fig. 5.4 (a) shows how the electric potential induces the stretches under the equilibrium condition. Only one equilibrium occurs at potentials ϕ lower than 0.224 and higher than 0.369, whereas three equilibria exist around the medium range potentials ϕ from 0.224 to 0.369. The higher and lower extremums ($\phi = 0.369$ and $\phi = 0.224$) are called snap-through and snap-back voltages, respectively. In this example, when the potential ϕ in the first equilibrium exceeds the snap-through voltage $\phi = 0.369$, the stretch response undergoes a sudden jump to a much larger value at the third equilibrium. Conversely, when the potential ϕ in the third equilibrium falls below the snap-back voltage $\phi = 0.224$, the stretch response returns to the first equilibrium. This phenomenon is called snap-through. Within this voltage range, three equilibrium solutions are observed, of which the first and third are stable, while the second is unstable. Figure 5.4 (b) shows the strain-stiffening behavior of the material function computed from Eq. (5.21) corresponding to the induced stretches. As seen in this figure, the slope of the hyperelastic material function versus stretch, representing the material stiffness, increases exponentially with stretch.

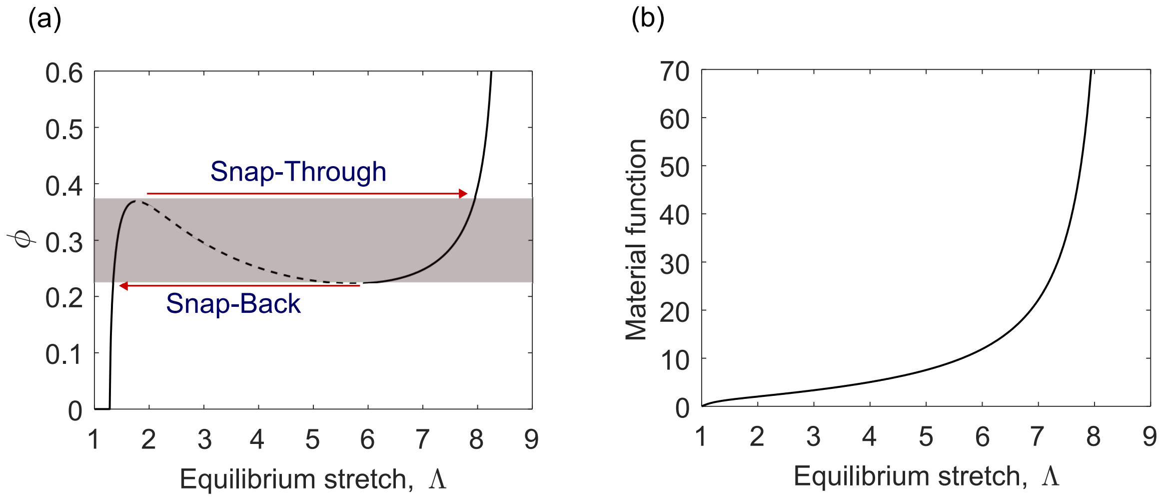

Figure 5.4: Stretches induced by a range of applied electric potential for pre-stretch tension $\chi = 1$. (a) The equilibrium stretches, where solid (dashed) lines denote stable (unstable) equilibria, for varying applied electric potential. (b) The material function corresponding to the induced stretches. The shaded region represents the electric potential domain with three equilibria.

Some of the models introduced earlier in this chapter are fitted to a sample of data points to evaluate their ability to capture the nonlinear strain-stiffening behavior of hyperelastic materials. Since the Gent model provides a valid approximation for VHB materials, we use it as a benchmark for evaluating the performance of other models in our study.

Figure 5.5 shows the voltage-stretch behavior predicted from five hyperelastic models. The red circles are from the Gent model shown in Fig. 5.4 for $\chi = 1$. The data points have nearly equal spacing and cover a majority of the stretch bandwidths from $\lambda = 0.224$ to 0.369. Even data points from larger stretches, exceeding 700%, are included to examine each model's ability to predict the strain-stiffening stretches. The approximated curves are computed numerically by minimizing the residual value Res in Eqs. (5.26) through the Least-Squares method for a given data-set. The numerical optimization (minimization) process requires initial guesses for the parameters to be determined in each hyperelastic model, including shear-related coefficients and exponents. The optimized parameters calculated for a smaller number of terms can serve as initial guesses for optimization with a larger number of terms. For example, the optimization results for a two-term model can be used as initial guesses for the first two terms of a three-term model. Higher-order terms typically govern the larger stretches, whereas lower-order terms mostly influence the small and moderate stretches. The shear-related coefficients generally decrease as the power of their corresponding exponents increases. In the Yeoh model, as an example, knowing that the first coefficient $\mu_1 = 0.5$, the guesses for the second and third coefficients should be $\mu_2 = 10^{-3}$ and $\mu_3 = 10^{-6}$. The optimal solutions obtained from the data-fitting process depend on the initial guesses and data characteristics. The inclusion of large and limiting stretches significantly impacts the optimal solutions.

Figure 5.5 (a) shows fitted curves for Neo-Hookean, Mooney-Rivlin, and Yeoh models. As expected, Neo-Hookean and Mooney-Rivlin models are only able to capture small stretches. The Mooney-Rivlin model accurately predicts the snap-through voltage $\Phi = 0.369$, while the snap-through voltage approximated by the Neo-Hookean model ($\Phi = 0.359$) is less accurate. Both models fail to predict the snap-back voltages. However, a four-term Yeoh model demonstrates a close fit to the entire data set. Even a four-term Yeoh model captures both the snap-through and snap-back voltages with adequate precision. The predicted snap-through voltage is $\Phi = 0.364$, while the snap-back stretch is underestimated by about 0.5 compared with the reference value. Figure 5.5 (b) shows fitted curves for the three-term Ogden and Lopez-Pamies models. It can be seen that only three terms are sufficient for these two models to capture a wide range of datasets, including both the snap-through and snap-back voltages. Adding extra terms evidently equips the series-based model with greater flexibility to fit data sets. It should be noted that these three terms involve six determining parameters, which offer greater flexibility than a three-term model with three parameters.

Figure 5.6 shows data-fitting for various numbers of terms of the Yeoh model. In this case, the upper limit of the last data point is extended to the limiting stretches over 800%. The approximation of a wide range of data sets, including the limiting stretches, requires high flexibility. As seen in this figure, four and seven terms of the Yeoh model are not enough to accurately capture the entire data set. Results for a twelve-term Yeoh model, on the other hand, are able to accurately predict the voltage-stretch behavior even at large stretches where strain-stiffening occurs. Increasing the number of terms enhances the potential of models to accurately capture the entire data set, including larger stretches. However, the likelihood of convergence in numerical optimizations decreases as the number of terms increases. The inclusion of larger and the limiting stretches reduces the chance of convergence. The selection of the hyperelastic model that is more appropriate for the specified data set can improve the convergence robustness.

Results obtained through the numerical optimization are non-unique, and multiple sets of optimal parameters may exist. A set of optimal parameters for a given number of terms may achieve a more accurate approximation for small to medium-range stretches, whereas the other may perform better at larger and limiting stretches. In addition to strain-stiffening stretches, accurate prediction of the snap-through and snap-back voltages is of importance. Therefore, evaluating the performance of hyperelastic models across different stretch values for a given material can help achieve a more accurate approximation.

Data-fitting for the two Ogden and Lopez-Pamies models with three and four terms is shown in Fig. 5.7. The Ogden model with three and four terms, shown in Fig. 5.7 (a), provides an accurate fit to the data, including some limiting stretches. Similarly, an accurate fit to this data set is seen for the Lopez-Pamies model shown in Fig. 5.7 (b). It can be

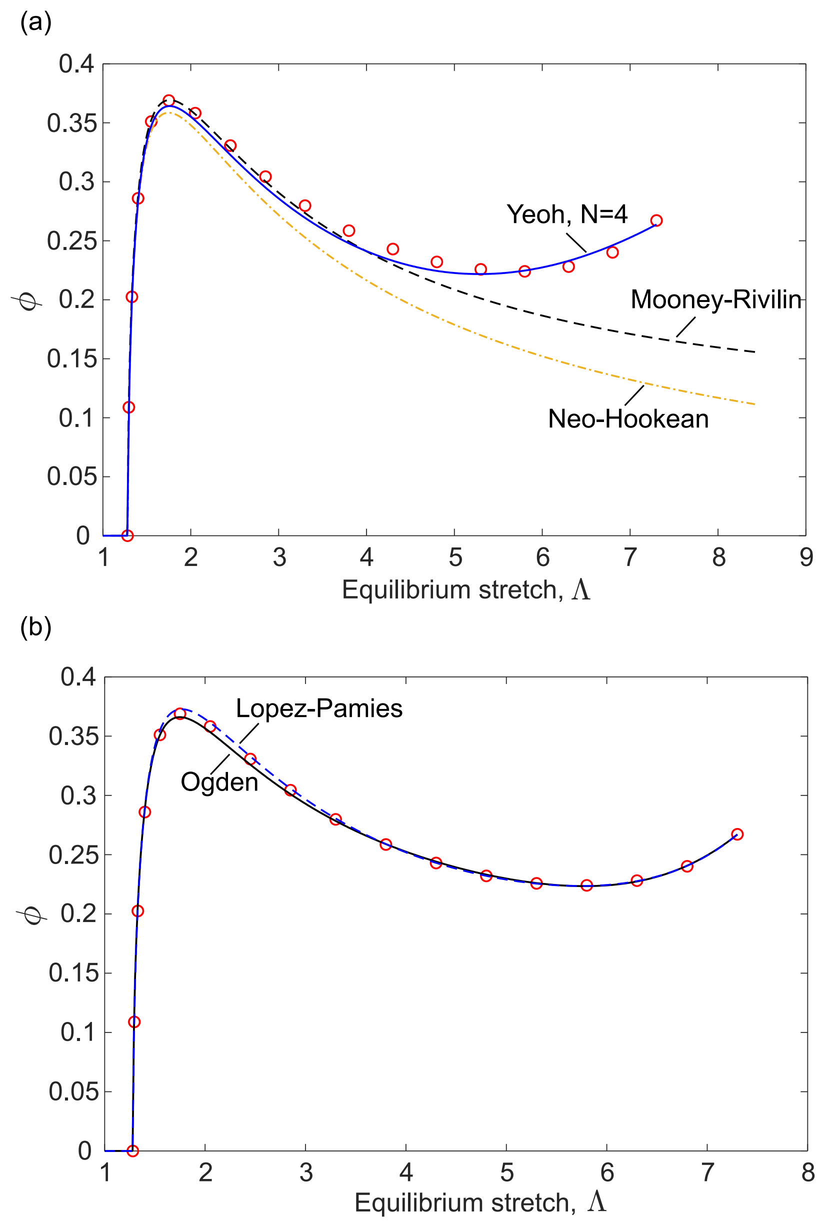

Figure 5.5: Stretch response versus varying electric potentials approximated for the specified data points using a number of hyperelastic models. (a) Neo-Hookean, Mooney-Rivlin, and a four-term Yeoh model. (b) Ogden and Lopez-Pamies models with three terms. The red circles denote the data points extracted from the membrane responses under pre-stretch tension $\chi = 1$ computed using the Gent model.

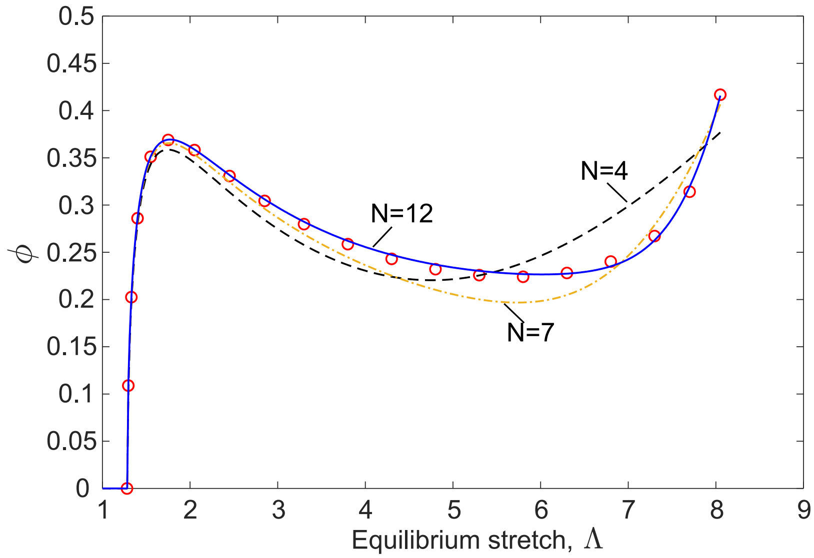

Figure 5.6: Stretch response versus varying electric potentials approximated for the specified data points using the Yeoh model with different number of terms.The red circles denote the data points extracted from a membrane responses under pre-stretch tension $\chi = 1$ computed using the Gent model.

observed that increasing the number of terms from three to four improves the precision of the approximation. Much of this accuracy should be attributed to the use of two parameters in each term, a coefficient and an exponent, rather than one.

5.7 Finite Element simulation results

Finite element analysis in COMSOL Multiphysics is employed in this section to solve the coupled electromechanical equations of the pre-stretched membrane subjected to an applied electric potential. Because of the non-linearities in the soft elastomers under large deformations, achieving convergence in this simulation is quite challenging. To smooth the process of convergence, an appropriate nonlinear solver as well as initial values for the stretches and electric potentials throughout the membrane body are required. As explained earlier, the elements are modeled as nearly squares, which effectively visualizes their deformations in each dimension. The difference between the two sides of the deformed

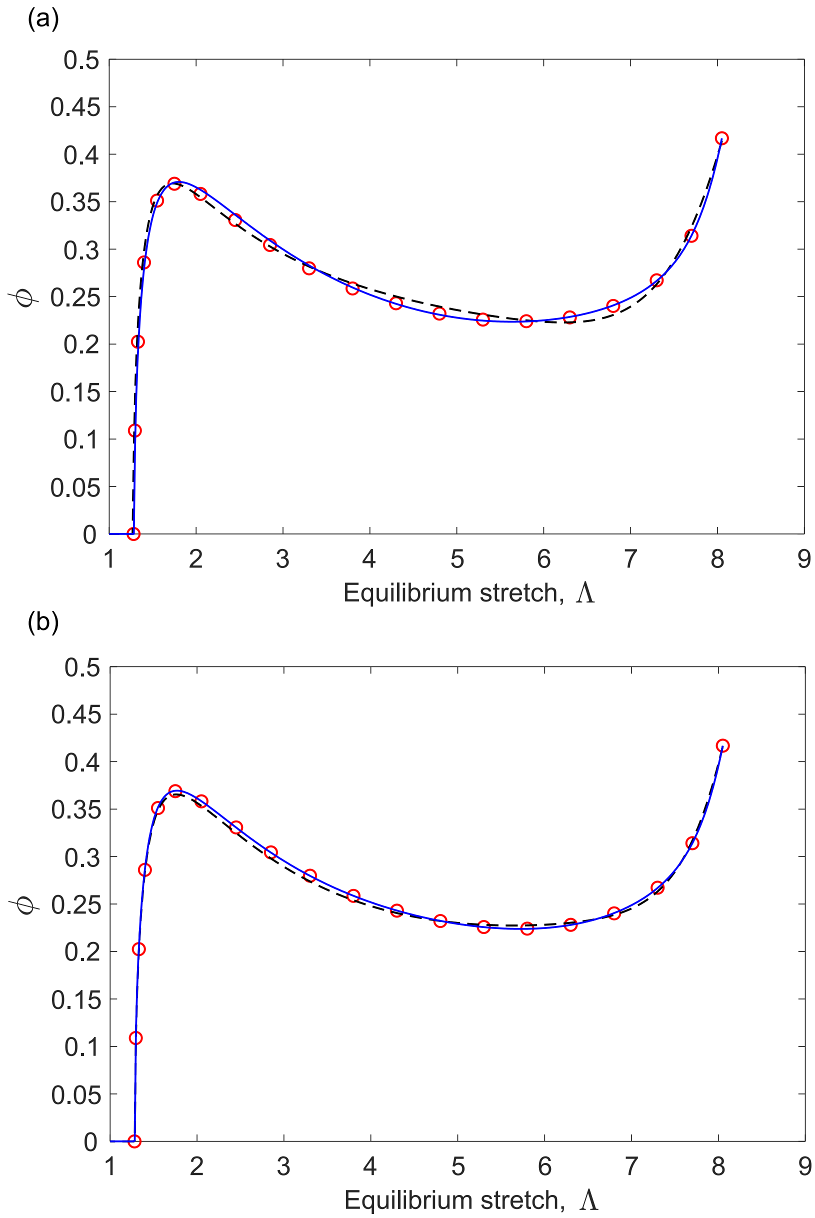

Figure 5.7: Stretch response versus varying electric potentials approximated for the specified data points using (a) the Ogden model and (b) the Lopez-Pamies model. The dashed black and solid blue lines represent the three-term and four-term models, respectively. Red circles denote the data points extracted from a membrane response under pre-stretch tension $\chi = 1$ computed using the Gent model.

quadrilateral element illustrates how much deformation occurs in each direction. Given the uniform distribution of the pre-stretch over the thickness of the membrane, discretizations with six elements along the axial direction are sufficient. Because the membrane is very thin, the selected radial discretizations yield accurate and reliable results. Nevertheless, for a given finite element mesh, the convergence of the solution is realized when reducing the size of the elements does not change the results. In this case, reducing the element size by half in both dimensions does not change the results.

For more robust convergence, the fully coupled solver is employed in this study, which solves the mechanical and electric equations simultaneously. Convergence is achieved when the residual norm of the equations falls below the predefined relative tolerance, set here as 10^{-6}. The nonlinear system of equations is solved through an iterative procedure based on the Newton–Raphson method, given by

$$\mathbf{x}_{i+1} = \mathbf{x}_i + \alpha \mathbf{J}(\mathbf{x}_i)^{-1} \mathbf{Res}(\mathbf{x}_i) \tag{5.34}$$

where $\mathbf{x_i}$ denotes the solution vector in the iteration i. **Res** and **J** are the residual vector and the Jacobian matrix of the governing equations, consisting of Eqs. (5.27) and (5.33). α, known as the damping or relaxation factor, is responsible for controlling the size of each Newton-Raphson update step. The damping factor α varies between 0 and 1. Convergence is slower but more stable for smaller values of α, while it is faster but less stable for larger values of α. The damping factor is automatically updated by the software at each iteration.

The solution of nonlinear equations depends on the initial guesses, which should be sufficiently close to the desired solution to ensure convergence. Since more than one solution may exist for a specific range of applied electric potentials, the initial values direct the solver to the intended solution. In the case shown in Figs. 5.4, three solutions exist for the electric potentials between 0.224 and 0.369. Given that the magnitude of the electric potential is considered a constant input, the initial value for this parameter should match the specified input value. For small stretches, the initial value should match the pre-stretch value. For larger stretches, on the other hand, the stretch value should be guessed. Hence, the solutions corresponding to larger stretches can only be obtained through a trial-and-error approach, using the initial guesses closer to the target result. If the solver fails to converge to the desired solutions within the specified tolerance, the initial values must be adjusted. The solution validity can be confirmed by repeating the process with new initial values slightly perturbed from the previous ones. Divergence of the solver across a range of initial stretch values for a specified electric potential implies the absence of a feasible solution for the specified values.

For the example in Fig. 5.4 (a), the first equilibrium can be computed using the pre-stretch values $\Lambda_0 = 1.283$ as the initial guess for the electric potential less than 0.365. For larger electric potentials (0.224 to 0.369), the initial values can be updated by solutions from a smaller one. Typically, the solver diverges, and no solutions can be obtained for small initial values of stretches when the electric potential surpasses the snap-through voltage. Thus, the snap-through voltage can be identified by incrementally increasing the applied electric potential until the solver diverges. Solutions for larger electric potentials (larger than 0.365) in Figs. 5.4 (a) can be obtained using very large initial stretch values, e.g., larger than 750%. In the same manner, the snap-back voltage can be determined by gradually decreasing the voltages from the third equilibrium.

5.7.1 Simulation results for the single active membrane

In this section, the membrane is considered incompressible to compare the results with the analytical solutions. Weakly compressible conditions are also studied to investigate the impacts of compressibility on stretch.

Figure 5.8 shows the stretch contours for the first equilibrium in the membrane consisting of a single active region under pre-stretch $\Lambda_0 = 2$ at $\Phi = 4.6$ kV. The pre-stretch tensile load $P = 1.379$ N ($\chi = 2.043$) is computed from Eq. (5.8) analytical modeling for the pre-stretch $\Lambda_0 = 2$. Figs. 5.8 (a) and (b) display the cross-section and top views of the radial stretch. Figs. 5.8 (c) and (d) display the cross-section and top views of the axial stretch. The black circle in top views represents the boundaries of the undeformed membrane. No variations in all stretches across the membrane radial centerline and the thickness are seen in these figures. In the single active membrane, the magnitude of the circumferential stretch is exactly equal to the radial stretch throughout the membrane body. The axial stretch calculated from the relation $\Lambda_{zz} = 1/(\Lambda_{rr}\Lambda_{\theta\theta}) = 0.13516$, which agrees with the value from the finite element simulation, 0.13515.

Figure 5.9 compares the stretches calculated by the analytical modeling and finite element simulations for varying electric potentials. Figure 5.9 (a) presents the equilibrium electric potential-stretch diagram for pre-stretch $\Lambda_0 = 1.2$ produced by the radial force $P = 0.541$ N ($\chi = 0.801$). The equilibrium voltage-stretch diagram for pre-stretch $\Lambda_0 = 2$ produced by the radial force $P = 0.541$ N ($\chi = 2.043$) is shown in Fig. 5.9 (b). Convergence is achieved for the given number of elements because the reduction in the size of elements does not lead to any changes in the values of the results. Good agreement is observed between the results calculated by analytical modeling and the finite element simulations.

For a nearly compressible membrane ($\kappa = 100\ \mu$) in Fig. 5.9, large stretches (above 500%) deviate noticeably from those of an incompressible material. The deviations in small and moderate stretches are trivial. The main reason is the use of the incompressible assumption in the analytical modeling. Under no electric field, a small deviation is seen in the weak-compressible membrane with the bulk modulus $\kappa = 100\ \mu$. Increasing the bulk modulus makes the membrane less compressible, which exhibits more agreement with the

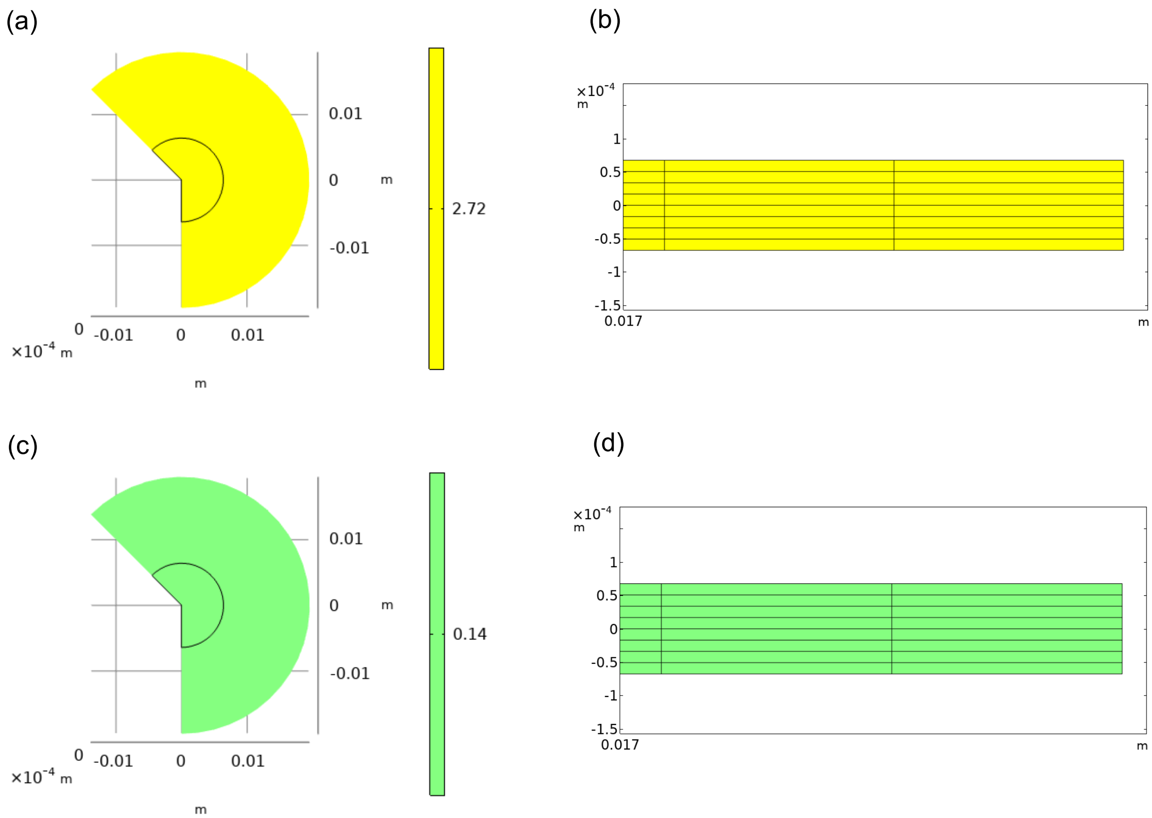

Figure 5.8: Finite element calculations of the stretch at pre-stretch $\Lambda_0 = 2$ and the electric potential $\Phi = 4.6$ kV shown from (a, c) the top view and (b, d) the cross-section view. The radial and axial stretches are shown in (a,b) and (c,e), respectively.

analytical modeling. The impacts of compressibility on the snap-through and snap-back voltages are not meaningful. The limiting stretch is larger in compressible membranes. It also experiences larger stretches under smaller values of electric potentials.

In the case with pre-stretch $\Lambda_0 = 1.2$, the finite element simulation is unable to converge to any solution for a large portion of the unstable, moderate stretch equilibrium. For the incompressible membrane, no convergence is achieved for the entire second equilibrium.

Fig. 5.10 shows the stretch contours for the second and third equilibria in the membrane under pre-stretch $\Lambda_0 = 2$ at $\Phi = 4.6$ kV. An increase in radial stretch is seen in both top and cross-section views in Figs. 5.10 (a). Stretches are uniform throughout the entire body. Similar to the first equilibrium, the circumferential stretch is exactly equal to the radial stretch, and the axial stretch is equal to the inverse of the radial stretch squared.

5.7.2 Simulation results for the hybrid active-passive membrane

Square elements are also used for the hybrid active-passive membrane model, like in the previous case. Finite element simulations allow for investigating the variations in all types of stretches across the radial centerline and the thickness in both active and passive regions. To evaluate the validity of our results, we compare these results with the experimental results conducted by Professor Lowe's team at the University of Dayton. They studied the equilibrium stretch of a hybrid membrane under a fixed pre-stretch, shown in Fig. 5.11, for a varying electric potential, applied on the electrodes covering a confined central region. Under electric activation, the active region expands radially, but contracts in thickness. As the boundary of the hybrid membrane is fixed, no displacement occurs at the outer boundary of the passive region. Thus, the passive region shrinks radially, accompanied by an increase in thickness. The simulation results are compared with the experimental test results and the analytical solution for the single active membrane.

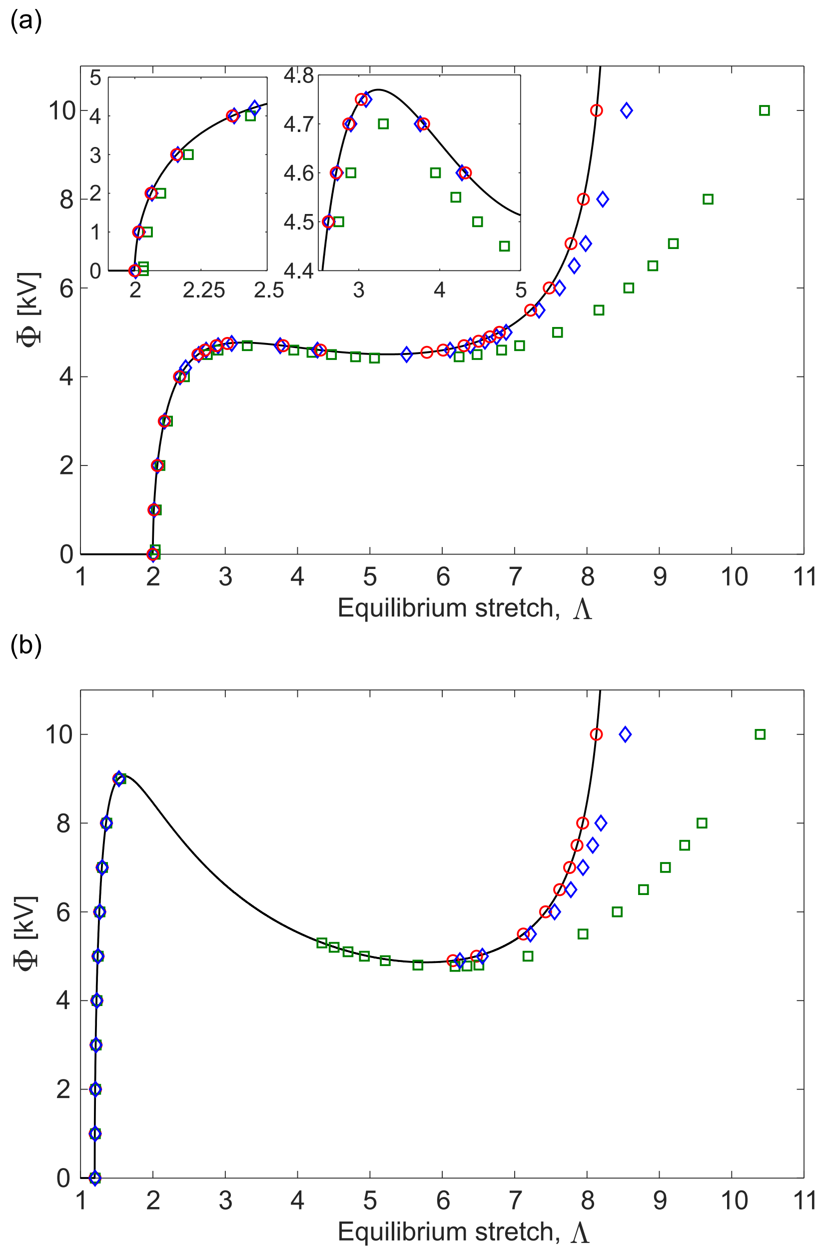

Figure 5.9: Electric potential-stretch diagram calculated by analytical modeling and the FEA simulations. (a) Pre-stretch $P = 0.541$ N, $\Lambda_0 = 1.2$. (b) $P = 1.379$ N, $\Lambda_0 = 2$. The black lines are the analytical solution. The red circles denote the simulation results for an incompressible membrane. The green squares and the blue diamonds denote nearly compressible membranes with the bulk modulus $\kappa = 100\ \mu$ and $\kappa = 1000\ \mu$, respectively.

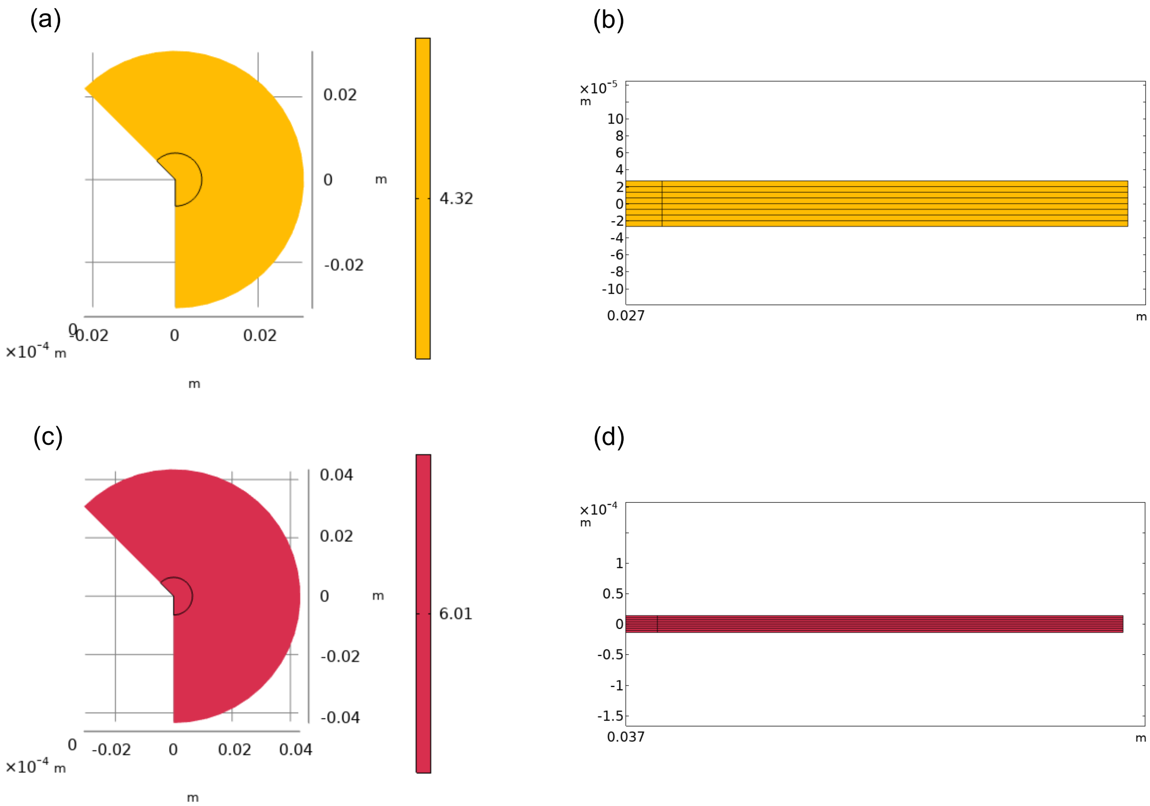

Figure 5.10: Finite element calculations of the stretch at pre-stretch $\Lambda_0 = 2$ and the electric potential $\Phi = 4.6$ kV shown from (a, c) the top view and (b, d) the cross-section view. The second and third equilibria are shown in (a,b) and (c,e), respectively.

(a)

(b)

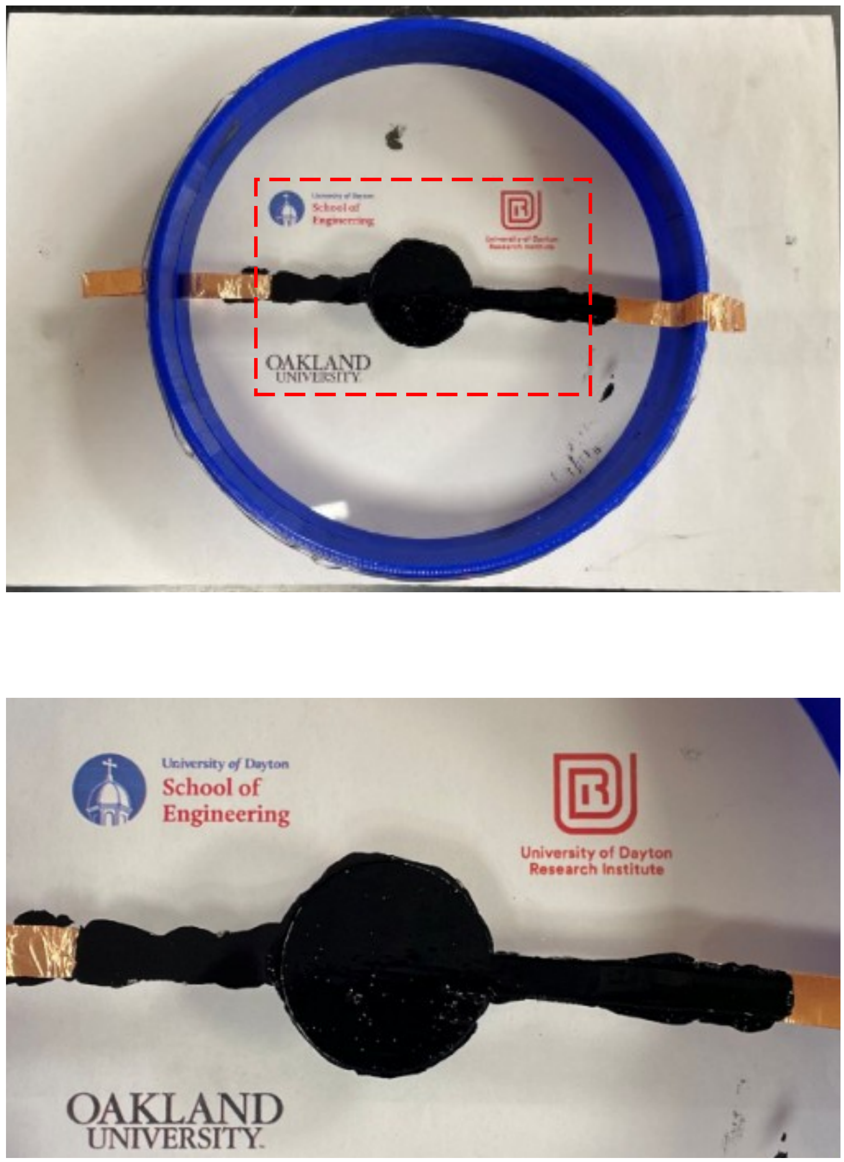

Figure 5.11: (a) Pictures of the experimental set. (b) The region shown in the dashed red box in (a).

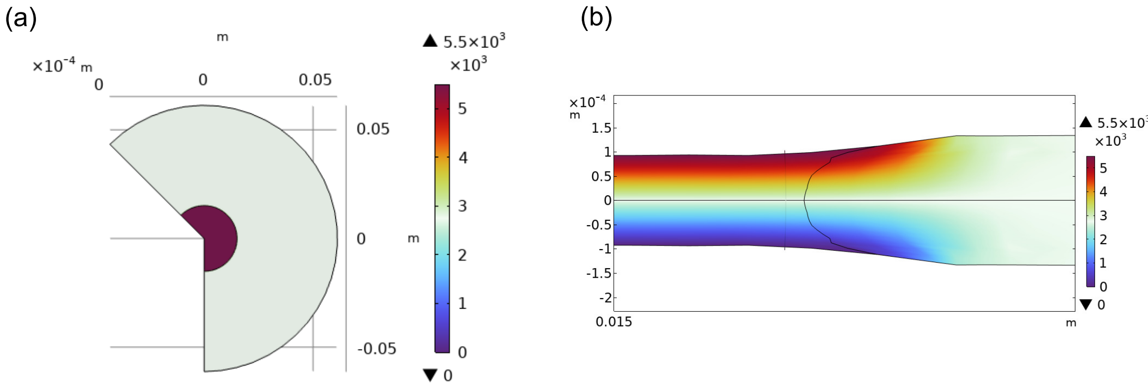

Figure 5.12: Finite element calculations of the electric field at pre-stretch $\Lambda_0 = 2$ and the electric potential $\Phi = 5.5$ kV shown from (a) the top view and (b) the cross-section view.

The distribution of the electric field is illustrated in Fig. 5.12. Frontal and cross-section views are shown in Figs. 5.12 (a) and (b), respectively. The electric potential is uniformly distributed throughout the entire active region. Within the active region, the electric field is distributed uniformly along the radial and axial directions. The electric field also penetrates the interface and influences a small portion of the passive region. Most of the passive region remains unaffected by the electric field.

Figure. 5.13 shows the equilibrium stretch contours for the hybrid membrane with active and passive regions under pre-stretch $\Lambda_0 = 2$ at $\Phi = 5.5$ kV. Figure. 5.8 (a) and (b) display the cross-section and top views of the radial stretch. Figure. 5.8 (c) and (d) show the cross-section and top views of the circumferential stretch. Figure. 5.8 (e) and (f) display the cross-section and top views of the cross-section views show the interface region. The black circles in the top views represent the boundaries of the undeformed active and passive regions. In the active region, no meaningful variations in the stretches are observed. The interface between the two regions is not a straight line, but a curve inclined toward the passive region. Sharp changes in the stretches occur around the interface between the active and passive regions in both the radial and axial directions. The radial stretch Λ_{rr} is about

2.2 inside the active region, but drops to less than 2 in the passive region just after passing the interface. Some extreme local gradients in stretches are seen around the interface region, which lie close to the upper and lower surfaces. Near the centerline across the interface curve, the radial and axial stretches are around 2 and 0.25, respectively. At the upper surface across the interface curve, the radial and axial stretches rise to 2.8 and 0.8, respectively. These changes are less noticeable for the circumferential stretch. Moving away from the interface area toward the passive region, variations in the stretches become smaller. The membrane in the active region undergoes a greater reduction in thickness than in the passive region due to the Maxwell stress tensor.

Figure 5.14 shows the variations in the stretch along the radial centerline in the hybrid membrane subjected to a range of applied electric potentials for pre-stretches Λ_0 1.2 and 2. Variations in radial and circumferential stretches along the radial centerline for pre-stretches 2 and 1.2 are shown in Figs. 5.14 (a) and (c), respectively. Within the active region, no meaningful variations in stretches along the radial centerline occur. The stretches increase with the growing applied electric potential in the active region. Moving out of the active region around the interface, the magnitude of the radial stretch undergoes a significant local drop. The radial stretch Λ_{rr} drops from 1.65 (2.90) to 0.82 (1.15) for $\Lambda_0 = 1.2$ (2) and electric potential $\Phi = 12.5$ (6.5) kV. The magnitude of this drop grows with increasing values of the applied potential. Moving away from the interface, the stretches increase radially across the passive region. At the final point, the radial stretches are a bit smaller than the pre-stretch value. The radial stretch Λ_{rr} rises from 0.82 (1.15) to 1.15 (1.91) under pre-stretch $\Lambda_0 = 1.2$ (2) and electric potential $\Phi = 12.5$ (6.5) kV. As there is a constraint for the total radial deformations of the membrane, increasing the applied electric potential reduces the stretches in the passive region. Inside the active region, the radial stretch Λ_{rr} rises from 1.22 (2.14) to 1.65 (2.90) when the electric potential Φ increases from 5 (4) kV

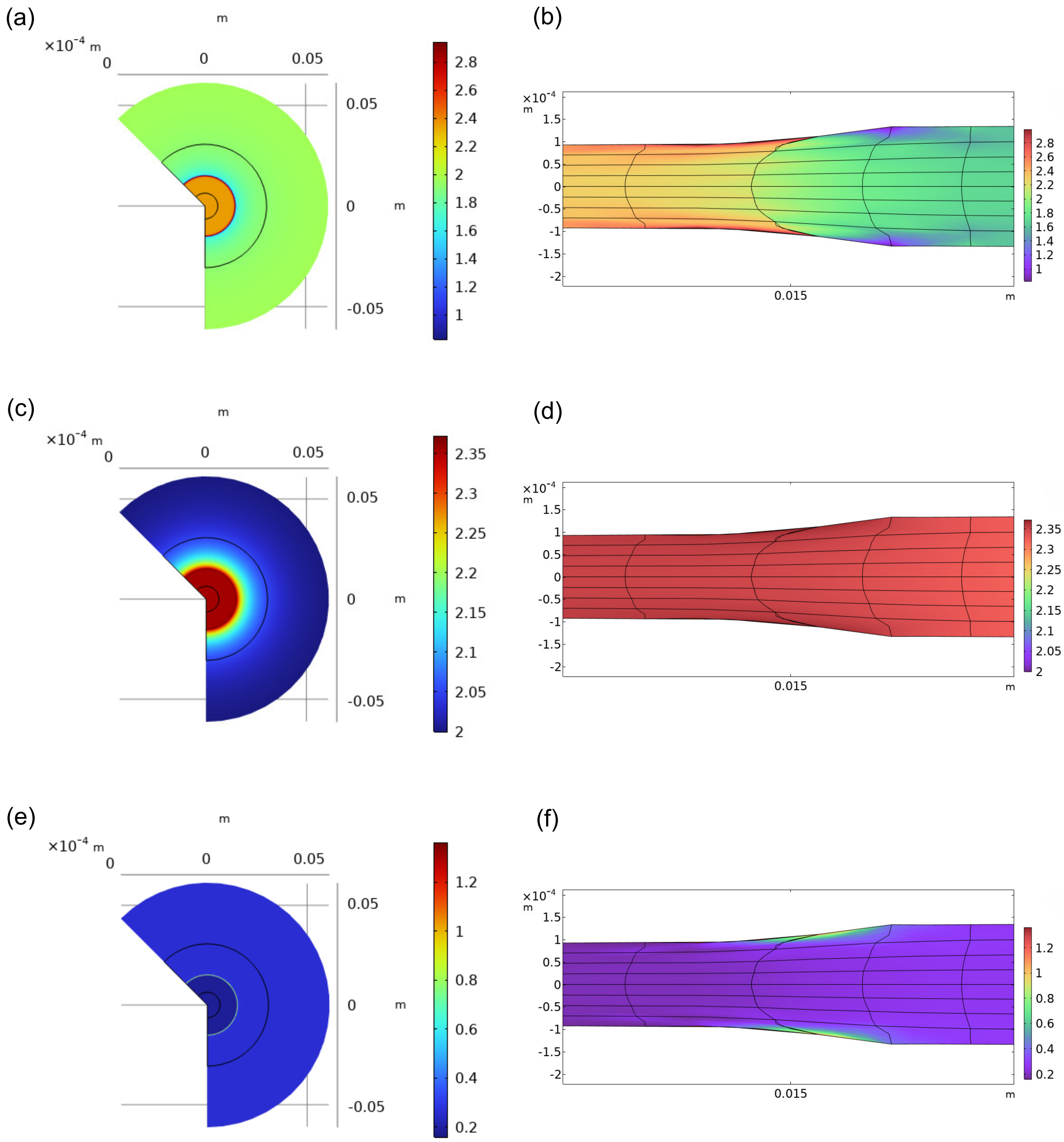

Figure 5.13: Finite element calculations of the stretch at pre-stretch $\Lambda_0 = 2$ and the electric potential $\Phi = 5.5$ kV shown from (a, c, e) the top view and (b, d, f) the cross-section view. The radial, circumferential, and axial stretches are shown in (a,b), (c,e), and (e,f), respectively.

to 12.5 (6) kV for pre-stretch $\Lambda_0 = 1.2$ (2). In other words, this reduction makes up for the growing stretches in the active region.

The magnitude of the circumferential $\Lambda_{\theta\theta}$ stretch, shown in Figs. 5.14 (a) and (c), equals the radial stretch Λ_{rr} inside the active region. However, it experiences a smoother decrease after the interface than the radial stretch, which continues until the end of the passive region. It nearly equals the pre-stretch value $\Lambda_0 = 1.2$ (2) at the final edge of the passive regions. Inside the active region, the compression of the axial stretch decreases with increasing electric potential, from 0.65 (0.22) to 0.37 (0.12) for pre-stretch $\Lambda_0 = 1.2$ (2) and electric potential $\Phi = 12.5$ (6.5) kV.

The variations in the axial stretches along the radial centerline for pre-stretches 2 and 1.2 are shown in Figs. 5.14 (b) and (d), respectively. The compression of the axial stretch Λ_{zz} undergoes a substantial drop near the interface, from 0.36 (0.12) to 0.76 (0.31) for pre-stretch $\Lambda_0 = 1.2$ (2) and electric potential $\Phi = 12.5$ (6.5) kV. After passing through the interface, it may slightly decrease to a steady value, which persists until the end of the passive region. The magnitude of the compression of the axial stretch within the passive region decreases slightly with increasing voltages. It rises from 0.66 (0.25) to 0.72 (0.26) when the electric potential Φ increases from 5 (4) kV to 12 (6.5) kV for pre-stretch $\Lambda_0 = 1.2$ (2).

Comparing results in Figs. 5.14 (a) and (c) with those in Figs. 5.14 (b) and (d) indicate that the distribution of stretches across the membrane for varying electric potentials under pre-stretches Λ_0 1.2 and 2 looks very similar. Hence, the variation in the pre-stretch does not meaningfully change the stretch distribution across the membrane for specified electric potentials.

Figure 5.15 shows the variations in the stretch across thickness at various radii in the active and passive regions. Figures 5.15 (a), (b), and (c) show the variations in the radial, circumferential, and axial stretches across the thickness at various radial sections. Radial

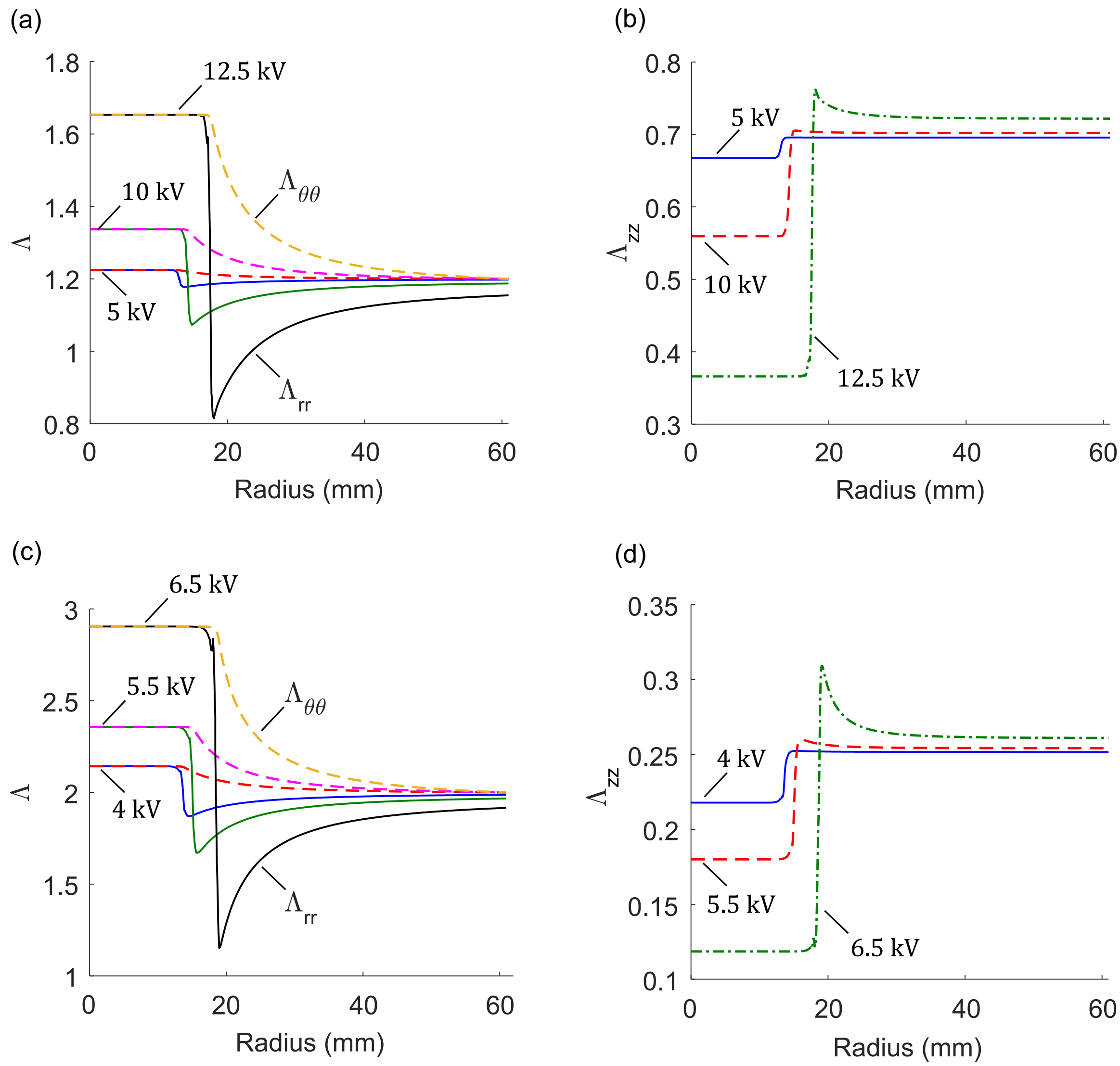

Figure 5.14: Finite element calculation of stretches for varying undeformed radial position in the hybrid membrane model. (a, c) The radial and circumferential stretches and (b, d) axial stretches. The pre-stretch $\Lambda_0 = 1.2$ and $\Lambda_0 = 2$ are shown in (a, b) and (c, d), respectively.

positions shown in these figures are based on the undeformed body. Sections at $R = 1$ mm and $R = 5$ mm are located inside the active region, which are selected to be close to the center and boundary of the active region. $R = 7$ mm and $R = 30$ mm are located inside the passive region, which are selected to be close to two boundary sides of the passive region. Figures 5.15 (d) shows the variations in the stretches across the interface curve. No meaningful changes are observed across the membrane thickness in both active and passive regions away from the interface area. As discussed earlier, the stretches remain constant throughout the active region. The variations in the radial and axial stretches over the interface curve are meaningful. Radial and axial stretches are larger near the upper and lower surfaces in the interface region. Variations in the circumferential stretch are negligible.

Figure 5.16 compares the stretches for a range of applied electric potentials determined using various methodologies, including analytical modeling, finite element simulations, and experimental measurements. Results obtained for pre-stretches $\Lambda_0 = 1.2$ and 2 are presented in Figs. 5.16 (a) and (b), respectively. The stretches calculated by finite element simulations are displayed by the blue diamonds for the incompressible membrane and the red squares for the compressible membrane with the bulk modulus $\kappa = 100\ \mu$. The results obtained through the experimental tests are shown by the green circles. The analytical solutions for the single active membrane are also presented for comparison. As the analytical solution for the hybrid models problem cannot be easily obtained, the stretch effects are replaced with a constant force.

In the finite element simulations, no convergence is achieved for stretches larger than 1.65 (2.87) under pre-stretch Λ_0 1.2 (2). The maximum electric potentials Φ and stretches Λ under the pre-stretch $\Lambda_0 = 1.2$ shown in Fig. 5.16 (a) are 19.5 kV and 1.45 for the experimental tests and 12.5 kV and 1.65 for finite element simulations. Under pre-stretch $\Lambda_0 = 2$ in Fig. 5.16 (b), the maximum electric potentials Φ and stretches Λ are 9.25 kV

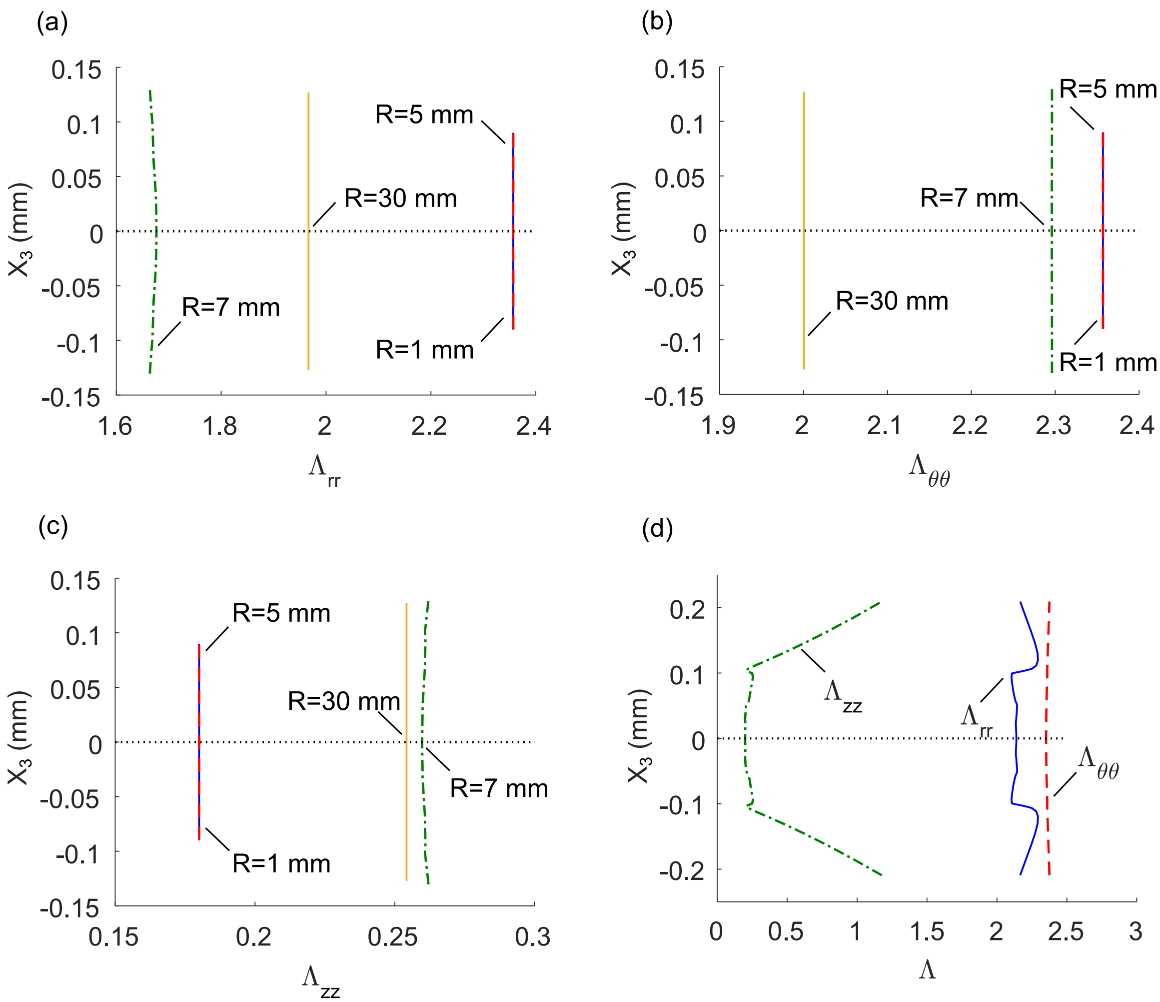

Figure 5.15: Finite element calculations of stretches across the thickness at different radii in the active and passive regions of the hybrid membrane model at $\Lambda_0 = 2$ and $\Phi = 5.5$ kV. The stretches for (a) the radial, (b) circumferential, and (c) axial axes. (d) All stretches across the interface curve.

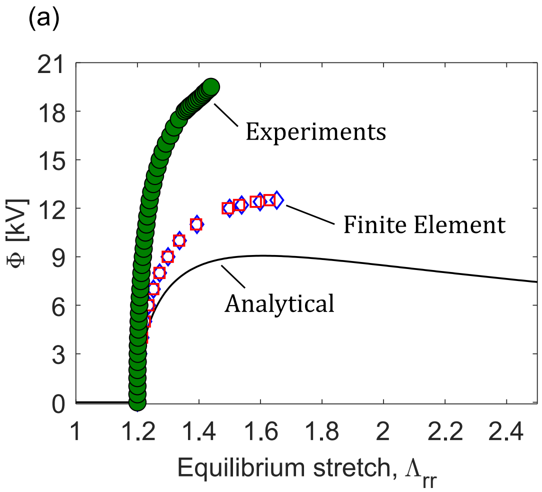

Figure 5.16: The stretch responses obtained through analytical modeling, the finite element simulations over a range of electric potentials at (a) Pre-stretch $\Lambda_0 = 1.2$ and (b) Pre-stretch $\Lambda_0 = 2$. The solid line and the green circles denote analytical modeling and the experimental results, respectively. The blue diamonds and the red squares denote the finite element results for the incompressible and compressible ($\kappa = 100\ \mu$) membrane.

and 2.7 for the experimental tests and 6.5 kV and 2.87 for finite element simulations. The maximum applied electric potential is higher for smaller pre-stretch values. The smaller stretches observed in the experimental results compared to those in the simulations may be the effects of the decreasing relative permittivity and some defects in the electro-mechanical coupling.

The applied tension on the active membrane in the analytical modeling is considered constant. In practice, however, the reactive tension caused by the pre-stretch decreases as the stretch of the passive region is reduced. A large portion of the disagreement between the analytical solutions and the simulation results arises from this reduction in the applied force.

5.8 Conclusion

The equilibrium response of a pre-stretched circular dielectric elastomer membrane is analyzed using analytical modeling and finite element simulations. The pre-stretch load is applied using two models, named the single active membrane and the hybrid membrane. In the single active membrane, a constant radial load is exerted evenly on the outer surface of the membrane subjected to varying electric potentials across the thickness. In the hybrid model, as a more practical model, the pre-stretch load is applied via a passive region extending from the active area and fixed at the outer boundary with a constant stretch magnitude.

The equilibrium stretch is investigated throughout the membrane for varying electric potentials. In the single active model with an incompressible material assumption, the finite element simulation results and the analytical solutions are in complete agreement. However, finite element simulations fail to achieve convergence for the unstable (second) equilibrium with smaller pre-stretches. As the compressibility of the membrane increases, the induced stretches at a given electric potential increase.

The simulation results for the hybrid models demonstrate that the stretches remain constant throughout the active region. Passing through the interface between the active and passive regions, the radial stretch drops sharply to a value below the pre-stretch magnitude. Then it rises smoothly to pre-stretch magnitude when approaching the outer boundary of the passive region. The circumferential stretch, on the other hand, gradually decreases across the passive region, reaching the pre-stretch magnitude at its outer boundary. Moreover, the compression of the axial stretch drops below the square of the pre-stretch value at the interface and then increases gradually to the ultimate magnitude. Given the thinness of the membrane, stretch variations are negligible except at the interface. Across the interface, the stretches increase as one moves away from the centerline. In the hybrid model, no convergence is achieved by the finite element simulation for stretches above the extremum point. Hence, only one equilibrium was calculated using this method. Discrepancies were observed in the results from the finite element simulation, experiments, and analytical modeling. The source of this disagreement in the analytical modeling originates from the reduction of the exerted force as the initial stretches in the passive region decrease. The deviation of the experimental results may be attributed to the decreasing relative permittivity and incomplete electro-mechanical coupling.

The capacity of several widely used hyperelastic formulations to fit a specified data set using the least-squares method is evaluated. Series-based formulations exhibit a higher capacity to approximate specified data sets. An increased number of terms can yield higher accuracy in data-fitting at the expense of a lower chance of convergence in the optimization process. Moreover, models with two determining parameters per term can achieve more accurate data-fitting for a smaller number of terms.

CHAPTER SIX

CONCLUSION

6.1 High-speed vibration and stability of cantilevered beams

The dynamics of a cantilevered beam with a rigid body attached at its free end that spins about its longitudinal axis is modeled and studied in this work. The formulation incorporates the effects of shear deformations and rotary inertia. The resulting hybrid discrete-continuous model is cast into the extended operator form and discretized with the help of Galerkin's method and orthogonal polynomial basis functions. The system of equations is solved numerically for two models, referred to as symmetric and asymmetric. A closed-form solution is also presented for the symmetric system to validate the numerical results calculated through the Galerkin method and also create a foundation for developing the basis functions application to more complex systems. Finite element simulations are conducted to evaluate the analytical modeling results.

Symmetric systems are characterized by identical inertia and stiffness properties in the two bending directions. The eigenvalues of these systems are degenerate at zero speed but split into two groups. One decreases with the rotation speed and possesses forward orbits, aligned with the direction of rotation. The other one increases with the speed and corresponds to backward orbits, opposed to the direction of rotation. As the rotation speed varies, forward- and backward-orbit eigenvalues cross one another without modal interaction. In the symmetric systems, eigenvalues are purely imaginary and stable with circular orbits except for the critical speeds, where the eigenvalues vanish. The contribution of shear deformations becomes more pronounced with growing speed in forward-orbit modes, despite a decrease in their natural frequencies. For backward-orbit modes, in contrast, the contribution of shear deformations declines with increasing speed.

Asymmetric systems are identified by non-identical inertia and stiffness properties in the two bending directions, which makes the eigenvalues distinct at zero speed and the orbits elliptic elsewhere. Similar to the symmetric system, the eigenvalues of forward-orbit modes decrease, while those of backward-orbit modes increase as the speed increases. However, the eigenvalues of opposite orbit types do not cross when approaching each other, but rather veer away. This phenomenon is called veering interaction, where both forward- and backward-orbit modes couple. As a result of this modal coupling, a blend of the interacting modes emerges in the resulting mode shape, with both forward and backward orbits simultaneously present in different regions of the beam span. Sharp local changes in shear strain energy of the interacting modes within the veering region represent one of the effects of this modal coupling. In the asymmetric systems, the interaction of eigenvalues of opposite orbit modes at higher speeds, where the forward mode is of higher order than the backward mode, engenders flutter instabilities. Marked local changes in shear strain energy are also observed just before and after the flutter bandwidth due to the modal interactions. Veering interaction and flutter instabilities are the characteristics of asymmetry in systems' stiffness and inertia with noticeable shear deformation effects. The effects of variations in various parameters of the beam and rigid body on the instability of the spinning system are investigated in detail. Under a stronger asymmetry, more than one divergence instability may simultaneously arise in more than one eigenvalue at the same speed. This atypical instability is formed by the conversion of a flutter instability into a divergence instability. The bandwidth of the unstable regions caused by beam asymmetry can be offset or reduced by rigid body asymmetry when it is aligned in the direction perpendicular to that of the beam.

Closed-form solutions are also presented for a rotating beam-rigid body with symmetric geometry using a complex-valued form of equations. This complex form is derived by combining the variables along the perpendicular axes into a single complex-value variable. Numerical solutions of these relations yield the natural frequencies and corresponding mode shapes and critical speeds for arbitrary mode numbers. The results of the closed-form solution show an excellent agreement with those obtained via the Galerkin method. Speed variations cause meaningful changes to the mode shapes, which are more significant in higher modes and for a larger rigid body. Mode shapes obtained from the closed-form solution can be used The mode shapes derived from closed-form solutions can serve as effective basis functions for addressing more complicated problems with stronger nonlinear properties.

The modal properties and natural frequencies of a spinning cantilever beam carrying a tip rigid body are also analyzed using the finite element method. Natural frequencies are calculated for varying rotation speeds in the inertial coordinate system. These results are transformed into the co-rotational coordinate system and compared with the analytical modeling results. Both groups of results are in relatively close agreement, which diminishes with increasing mode number and rotational speed. For each bending mode, the Campbell diagram presents a pair of critical speeds close to the one computed by analytical modeling. Even the transformed results are unable to illustrate the veering interactions and flutter instabilities, where orbits do not remain homogeneous along the beam span. Apart from the bending modes, the axial and torsional modes are also modeled in the finite element simulations. Both axial and torsional modes remain unique across varying rotation speeds, although their natural frequencies undergo small changes.

6.2 Circular dielectric elastomer membrane actuators

A study is conducted on the performance of several well-known hyperelastic models in approximating a given set of data from a hyperelastic material's stretch using the least-squares method. Incorporating the series expansions into the hyperelastic formulations enables them to effectively capture the strain-stiffening behaviors of elastomers. A larger number of terms and the determining parameters can improve the accuracy of data-fitting, but simultaneously diminish the convergence potential.

The equilibrium stretch of two models of circular dielectric elastomer membrane actuators under a pre-stretch load is studied. The radial pre-stretching load is applied directly to the membrane in the first model but exerted indirectly on the membrane in the second model via a pre-stretched passive region. An electric potential applied across the membrane thickness between the upper and lower surfaces induces radial expansion.

The closed-form solution for the equilibrium response of the single active membrane is derived analytically. The equilibrium stretch is also calculated numerically employing finite element simulations. For an incompressible membrane, a close agreement is observed between the analytical solution and the simulation results. Stretches are uniformly distributed throughout the whole body. However, convergence cannot be realized in the finite element simulation for a large portion of the second equilibrium. Increasing compressibility results in larger stretches under a given electric potential.

In the hybrid membrane, no variations are observed in the stretches computed by finite element simulations throughout the active region. However, sharp changes in the radial and axial stretches occur around the interface separating the two regions. In the passive region, all stretches only undergo slight variations along the radial axis. The finite element simulation displays the increasing hyperelastic stretch in the active region with varying electric potentials, but fails to converge for larger stretches. The analytical solution for the single active region does not match the simulation results due to the assumption of a constant external force applied by the passive region. This force is expected to decrease as the passive region shrinks. The experimental results used for comparison also show smaller stretches, which is possibly due to the decreasing relative permittivity and the deficient electro-mechanical coupling.

6.3 Future work

- In this work, the natural frequencies, modal properties, and instabilities of a spinning Timoshenko cantilever beam carrying a rigid tip body are accurately calculated for varying speeds using theoretical approaches. Conducting some experimental tests is needed in future studies to improve the validity of the theoretical results. The experimental results can provide deeper insight into the modal coupling, veering interactions, and also instabilities, which are often difficult to predict accurately through theoretical modeling due to simplifying assumptions.

- A closed-form analytical solution for the spinning Timoshenko beam with symmetric cross-sectional geometry is presented in this study. The mode shapes derived in this solution are shown to undergo noticeable changes with varying speeds, which limits their effectiveness as basis functions for approximating the dynamics of more complex systems. Hence, a refinement to the closed-form solution is recommended to improve their applications as basis functions in weighted residual techniques, and as elastic modes in Component Mode Synthesis (CMS).

- The natural frequencies and modal properties of the spinning system are computed using finite element simulations for a range of rotation speeds. The natural frequencies, determined in the fixed (inertial) coordinate system, are transformed into the co-rotational coordinate system for comparison with the results obtained using the Galerkin method. However, the transformation process is challenging for the veering regions and flutter instabilities due to the simultaneous presence of both forward and backward orbits along the beam span. A proposed approach for better comparisons is to perform finite element simulations in the co-rotational coordinate.

- One of the primary applications of high-speed spinning systems is to function as gyroscopic resonator-based energy harvesters, which convert vibrational and rotational energy into electrical power. The gyroscopic coupling enables the harvester to capture energy from multi-axis dynamics, rather than being limited to linear motions. The findings of this study can be extended to the development of higher-efficiency gyroscopic resonator-based energy harvesters in future research.

- The analytical solution for the equilibrium response of the single active model of dielectric elastomer membrane actuators demonstrates close agreement with the finite element simulation results. However, formulating an experiment for this model encounters challenges because of difficulties in applying a constant, uniform tensile load. In this regard, it is recommended to design a practical experiment for this model, which can validate the theoretical results and enhance understanding of the actual dielectric electro-active interactions.

- The disagreement between the analytical solution for the single active model and the finite element simulation results for the hybrid model is meaningful. Hence, a derivation of an analytical solution for the hybrid model is recommended to strengthen confidence in the finite element simulation results.

- In this study, the equilibrium stretch of circular dielectric elastomer membrane actuators is investigated. Further studies are required to examine the nonlinear dynamics behaviors of these dielectric actuators and the impacts of various hyperelastic models.

APPENDIX A

COEFFICIENTS OF ORTHOGONAL POLYNOMIALS

A set of polynomial functions $\phi_i = \sum_{n=1}^{N} b_{ij} x^j$ were constructed using the Gram-Schmidt procedure [192]. N represents the number of polynomial functions used in the calculations. These functions were selected to have vanishing displacements at $x_3 = 0$ to satisfy the geometric boundary conditions for the beam. No other constraints were imposed. The coefficients of the polynomial expansion in normalized form were

$$\phi_1 = \sqrt{3}x \tag{7.1a}$$

$$\phi_2 = 4\sqrt{5}\left(-\frac{3}{4}x + x^2\right) \tag{7.1b}$$

$$\phi_3 = 15\sqrt{7}\left(\frac{2}{5}x - \frac{4}{3}x^2 + x^3\right) \tag{7.1c}$$

$$\phi_4 = 168\left(-\frac{2}{28}x + \frac{15}{14}x^2 - \frac{15}{8}x^3 + x^4\right) \tag{7.1d}$$

$$\phi_5 = 210\sqrt{11}\left(\frac{1}{14}x - \frac{2}{3}x^2 + 2x^3 - \frac{12}{5}x^4 + x^5\right) \tag{7.1e}$$

$$\phi_6 = 792\sqrt{13}\left(-\frac{7}{264}x + \frac{35}{99}x^2 - \frac{35}{22}x^3 + \frac{35}{11}x^4 - \frac{35}{12}x^5 + x^6\right) \tag{7.1f}$$

$$\phi_7 = 3003\sqrt{15}\left(\frac{4}{429}x - \frac{24}{143}x^2 + \frac{150}{143}x^3 - \frac{40}{13}x^4 + \frac{60}{13}x^5 - \frac{24}{7}x^6 + x^7\right) \tag{7.1g}$$

$$\begin{aligned}\phi_8 = 11440\sqrt{17}\Bigg(&-\frac{94}{29871}x + \frac{1168}{15907}x^2 - \frac{4178}{6897}x^3 + \frac{22697}{9367}x^4 - \frac{211780}{40339}x^5 + \frac{63}{10}x^6 \\ &- \frac{63}{16}x^7 + x^8\Bigg)\end{aligned} \tag{7.1h}$$

$$\begin{aligned}\phi_9 = 6\sqrt{336855929}\Bigg(&\frac{14}{13625}x - \frac{267}{8857}x^2 + \frac{170}{537}x^3 - \frac{1001}{608}x^4 + \frac{2358}{491}x^5 - \frac{2997}{364}x^6 \\ &+ \frac{1301}{158}x^7 - \frac{1751}{394}x^8 + x^9\Bigg)\end{aligned} \tag{7.1i}$$

$$\phi_{10} = \sqrt{543367450297}\left(-\frac{13}{32416}x + \frac{44}{3151}x^2 - \frac{408}{2315}x^3 + \frac{3444}{3071}x^4 - \frac{1651}{402}x^5 + \frac{1121}{122}x^6 - \frac{5196}{407}x^7 + \frac{4440}{413}x^8 - \frac{4125}{821}x^9 + x^{10}\right) \quad (7.1j)$$

$$\phi_{11} = \sqrt{1122188615}\left(-\frac{74}{8641}x + \frac{72}{241}x^2 - \frac{2347}{622}x^3 + \frac{2903}{121}x^4 - \frac{3943}{45}x^5 + \frac{15205}{78}x^6 - \frac{28945}{108}x^7 + \frac{10395}{47}x^8 - \frac{20848}{211}x^9 + \frac{2372}{141}x^{10} + x^{11}\right) \quad (7.1k)$$

$$\phi_{12} = \sqrt{120116909}\left(-\frac{83}{3257}x + \frac{927}{1043}x^2 - \frac{1805}{161}x^3 + \frac{5333}{75}x^4 - \frac{29485}{114}x^5 + \frac{15439}{27}x^6 - \frac{30370}{39}x^7 + \frac{23430}{37}x^8 - \frac{16310}{59}x^9 + \frac{20266}{441}x^{10} + \frac{1897}{1846}x^{11} + x^{12}\right) \quad (7.1l)$$

$$\phi_{13} = \sqrt{31203233}\left(-\frac{176}{3629}x + \frac{566}{335}x^2 - \frac{6146}{289}x^3 + \frac{76893}{572}x^4 - \frac{53523}{110}x^5 + \frac{13888}{13}x^6 - \frac{69155}{48}x^7 + \frac{10399}{9}x^8 - \frac{37088}{75}x^9 + \frac{5372}{67}x^{10} + \frac{1558}{901}x^{11} + \frac{455}{1317}x^{12} + x^{13}\right) \quad (7.1m)$$

$$\phi_{14} = 3\sqrt{1610915}\left(-\frac{112}{1641}x + \frac{1139}{480}x^2 - \frac{2590}{87}x^3 + \frac{11237}{60}x^4 - \frac{18855}{28}x^5 + \frac{48349}{33}x^6 - \frac{91720}{47}x^7 + \frac{75378}{49}x^8 - \frac{124631}{194}x^9 + \frac{9953}{99}x^{10} + \frac{2819}{1376}x^{11} + \frac{2489}{6751}x^{12} + \frac{495}{5297}x^{13} + x^{14}\right) \quad (7.1n)$$

$$\phi_{15} = 2\sqrt{3131745}\left(-\frac{293}{4305}x + \frac{337}{143}x^2 - \frac{5641}{192}x^3 + \frac{4946}{27}x^4 - \frac{38387}{59}x^5 + \frac{37588}{27}x^6 - \frac{19934}{11}x^7 + \frac{17976}{13}x^8 - \frac{32451}{59}x^9 + \frac{42310}{533}x^{10} + \frac{1201}{866}x^{11} + \frac{720}{4331}x^{12} - \frac{155}{7653}x^{13} - \frac{253}{2562}x^{14} + x^{15}\right) \quad (7.1o)$$

$$\phi_{16} = \sqrt{50651493}\Big(-\frac{101}{4420}x + \frac{1541}{1997}x^2 - \frac{6699}{724}x^3 + \frac{7354}{135}x^4 - \frac{6403}{36}x^5 + \frac{17754}{53}x^6$$
$$-\frac{41729}{118}x^7 + \frac{12705}{71}x^8 - \frac{11969}{804}x^9 - \frac{3347}{267}x^{10} + \frac{1183}{1536}x^{11} - \frac{405}{1247}x^{12} - \frac{299}{1348}x^{13} - \frac{237}{1051}x^{14}$$
$$-\frac{409}{945}x^{15} + x^{16}\Big) \quad (7.1p)$$

$$\phi_{17} = \sqrt{4794901}\Big(\frac{77}{739}x - \frac{13960}{3881}x^2 + \frac{2901}{65}x^3 - \frac{10225}{37}x^4 + \frac{360611}{371}x^5 - \frac{30772}{15}x^6$$
$$+\frac{34041}{13}x^7 - \frac{56271}{29}x^8 + \frac{3681}{5}x^9 - \frac{28482}{293}x^{10} - \frac{494}{363}x^{11} - \frac{81}{3833}x^{12} + \frac{143}{882}x^{13} + \frac{1732}{6465}x^{14}$$
$$+\frac{519}{809}x^{15} - \frac{338}{107}x^{16} + x^{17}\Big) \quad (7.1q)$$

$$\phi_{18} = \sqrt{641847}\Big(\frac{297}{989}x - \frac{1695}{163}x^2 + \frac{8295}{64}x^3 - \frac{86413}{107}x^4 + \frac{97411}{34}x^5 - \frac{238621}{39}x^6$$
$$+\frac{158807}{20}x^7 - \frac{54274}{9}x^8 + \frac{7145}{3}x^9 - \frac{39817}{117}x^{10} - \frac{1305}{227}x^{11} - \frac{1238}{1907}x^{12} + \frac{419}{3129}x^{13} + \frac{360}{761}x^{14}$$
$$+\frac{1908}{1441}x^{15} - \frac{2645}{379}x^{16} + \frac{995}{1224}x^{17} + x^{18}\Big) \quad (7.1r)$$

$$\phi_{19} = \sqrt{173919}\Big(\frac{568}{963}x - \frac{4683}{229}x^2 + \frac{19151}{75}x^3 - \frac{118031}{74}x^4 + \frac{22709}{4}x^5 - \frac{36535}{3}x^6$$
$$+\frac{159017}{10}x^7 - \frac{207127}{17}x^8 + \frac{165885}{34}x^9 - \frac{5721}{8}x^{10} - \frac{5080}{393}x^{11} - \frac{668}{385}x^{12} + \frac{47}{30439}x^{13}$$
$$+\frac{1179}{1699}x^{14} + \frac{2353}{1076}x^{15} - \frac{7782}{647}x^{16} + \frac{3080}{2151}x^{17} + \frac{361}{993}x^{18} + x^{19}\Big) \quad (7.1s)$$

$$\phi_{20} = \sqrt{\frac{314421}{5}}\Big(\frac{2759}{2779}x - \frac{14019}{407}x^2 + \frac{37454}{87}x^3 - \frac{113089}{42}x^4 + \frac{201605}{21}x^5 - \frac{639841}{31}x^6$$
$$+\frac{162199}{6}x^7 - \frac{104018}{5}x^8 + \frac{117421}{14}x^9 - \frac{58490}{47}x^{10} - \frac{7217}{313}x^{11} - \frac{3089}{929}x^{12} - \frac{1414}{6197}x^{13}$$
$$+\frac{1361}{1418}x^{14} + \frac{222}{67}x^{15} - \frac{11344}{605}x^{16} + \frac{4764}{2105}x^{17} + \frac{391}{675}x^{18} + \frac{381}{1579}x^{19} + x^{20}\Big) \quad (7.1t)$$

$$\phi_{21} = \sqrt{\frac{314421}{5}}\Big(\frac{3535}{2316}x - \frac{2331}{44}x^2 + \frac{21863}{33}x^3 - \frac{111965}{27}x^4 + 14800x^5 - 31861x^6 + \frac{125411}{3}x^7 - \frac{129005}{4}x^8 + 13053x^9 - \frac{27305}{14}x^{10} - \frac{2528}{69}x^{11} - \frac{2347}{428}x^{12} - \frac{1409}{2500}x^{13} + \frac{1764}{1375}x^{14} + \frac{789}{166}x^{15} - \frac{5295}{193}x^{16} + \frac{752}{225}x^{17} + \frac{1984}{2307}x^{18} + \frac{610}{1697}x^{19} + \frac{700}{3811}x^{20} + x^{21}\Big) \tag{7.1u}$$

$$\phi_{22} = \sqrt{\frac{143809}{11}}\Big(\frac{721}{327}x - \frac{1531}{20}x^2 + \frac{177168}{185}x^3 - \frac{29986}{5}x^4 + \frac{149922}{7}x^5 - \frac{738319}{16}x^6 + \frac{121225}{2}x^7 - 46836x^8 + \frac{133016}{7}x^9 - \frac{19963}{7}x^{10} - \frac{28152}{521}x^{11} - \frac{6806}{823}x^{12} - \frac{4865}{4796}x^{13} + \frac{727}{435}x^{14} + \frac{229}{35}x^{15} - \frac{3716}{97}x^{16} + \frac{3119}{664}x^{17} + \frac{3461}{2853}x^{18} + \frac{586}{1153}x^{19} + \frac{257}{988}x^{20} + \frac{1311}{8761}x^{21} + x^{22}\Big) \tag{7.1v}$$

$$\phi_{23} = 2\sqrt{\frac{79646}{23}}\Big(\frac{1736}{571}x - \frac{7179}{68}x^2 + \frac{27743}{21}x^3 - \frac{66207}{8}x^4 + \frac{88703}{3}x^5 - \frac{191221}{3}x^6 + \frac{335147}{4}x^7 - \frac{335147}{4}x^8 + \frac{184368}{7}x^9 - \frac{43611}{11}x^{10} - \frac{16017}{212}x^{11} - \frac{2194}{187}x^{12} - \frac{4265}{2684}x^{13} + \frac{1873}{879}x^{14} + \frac{2605}{299}x^{15} - \frac{5310}{103}x^{16} + \frac{2153}{339}x^{17} + \frac{916}{557}x^{18} + \frac{902}{1307}x^{19} + \frac{494}{1397}x^{20} + \frac{431}{2117}x^{21} + \frac{461}{3633}x^{22} + x^{23}\Big) \tag{7.1w}$$

$$\phi_{24} = \frac{\sqrt{31519}}{2\sqrt{2}}\Big(\frac{4749}{1175}x - \frac{6878}{49}x^2 + \frac{36893}{21}x^3 - \frac{165119}{15}x^4 + \frac{314723}{8}x^5 - \frac{169681}{2}x^6 + \frac{223161}{2}x^7 - 86374x^8 + \frac{175707}{5}x^9 - \frac{58310}{11}x^{10} - \frac{6897}{68}x^{11} - \frac{6062}{381}x^{12} - \frac{647}{282}x^{13} + \frac{1573}{590}x^{14} + \frac{2065}{183}x^{15} - \frac{6798}{101}x^{16} + \frac{4019}{483}x^{17} + \frac{503}{233}x^{18} + \frac{810}{893}x^{19} + \frac{1001}{2152}x^{20} + \frac{455}{1698}x^{21} + \frac{199}{1191}x^{22} + \frac{311}{2815}x^{23} + x^{24}\Big) \tag{7.1x}$$

$$\phi_{25} = \sqrt{\frac{11877}{5}}\left(\frac{725}{139}x - \frac{8877}{49}x^2 + \frac{54425}{24}x^3 - \frac{99481}{7}x^4 + \frac{355604}{7}x^5 - \frac{219171}{2}x^6 \right.$$
$$+ \frac{432535}{3}x^7 - 111667x^8 + \frac{363759}{8}x^9 - \frac{13739}{2}x^{10} - \frac{6196}{47}x^{11} - \frac{2604}{125}x^{12} - \frac{2831}{903}x^{13}$$
$$+ \frac{3054}{931}x^{14} + \frac{5667}{397}x^{15} - \frac{6768}{79}x^{16} + \frac{977}{92}x^{17} + \frac{1868}{677}x^{18} + \frac{1729}{1490}x^{19} + \frac{1357}{2279}x^{20} + \frac{756}{2203}x^{21}$$
$$\left. + \frac{259}{1210}x^{22} + \frac{47}{332}x^{23} + \frac{635}{6479}x^{24} + x^{25}\right) \quad (7.1y)$$

APPENDIX B

MATRIX ELEMENTS FOR ORTHOGONAL POLYNOMIALS

The elements of the mass (Eq. (2.20a)), gyroscopic (Eq. (2.21a)), stiffness (Eq. (2.22a)), and centripetal (Eq. (2.23a)) matrices when orthogonal polynomials are used as basis functions ψ_{1k}, ϕ_{2l}, ψ_{1m}, and ψ_{2n} are

$$[\mathbf{M}_{11}]_{pk} = \sum_{i=1}^{N_1}\sum_{j=1}^{N_1}\left(\frac{1}{i+j+1}+\eta\right)c_{pi}c_{kj}, \quad p,k=1,2,\ldots,N_1 \tag{8.1a}$$

$$[\mathbf{M}_{22}]_{ql} = \sum_{i=1}^{N_2}\sum_{j=1}^{N_2}\left(\frac{1}{i+j+1}+\eta\right)c_{qi}c_{lj}, \quad q,l=1,2,\ldots,N_2 \tag{8.1b}$$

$$[\mathbf{M}_{33}]_{rm} = \sum_{i=1}^{M_1}\sum_{j=1}^{M_1}\left(\frac{\alpha\mu}{i+j+1}+\nu_{11}+\hat{d}^2\eta\right)c_{ri}c_{mj}, \quad r,m=1,2,\ldots,M_1 \tag{8.1c}$$

$$[\mathbf{M}_{44}]_{sn} = \sum_{i=1}^{M_2}\sum_{j=1}^{M_2}\left(\frac{\mu}{i+j+1}+\nu_{22}+\hat{d}^2\eta\right)c_{si}c_{nj}, \quad s,n=1,2,\ldots,M_2 \tag{8.1d}$$

$$[\mathbf{M}_{14}] = \overline{[\mathbf{M}_{41}]} = \hat{d}\eta\sum_{i=1}^{N_1}\sum_{j=1}^{N_1}c_{pi}c_{nj} \quad p(n)=1,2,\ldots,N_1(M_2) \tag{8.1e}$$

$$[\mathbf{M}_{23}] = \overline{[\mathbf{M}_{32}]} = -\hat{d}\eta\sum_{i=1}^{N_1}\sum_{j=1}^{N_1}c_{qi}c_{mj} \quad q(m)=1,2,\ldots,N_2(M_1) \tag{8.1f}$$

$$[\mathbf{G}_{12}] = -\overline{[\mathbf{G}_{21}]} = -2\sum_{i=1}^{N_1}\sum_{j=1}^{N_1}\left(\frac{1}{i+j+1}+\eta\right)c_{pi}c_{lj}, \quad p(l)=1,2,\ldots,N_1(N_2) \tag{8.2a}$$

$$[\mathbf{G}_{13}] = -\overline{[\mathbf{G}_{31}]} = -2\hat{d}\eta\sum_{i=1}^{N_1}\sum_{j=1}^{N_1}c_{pi}c_{mj}, \quad p(m)=1,2,\ldots,N_1(M_1) \tag{8.2b}$$

$$[\mathbf{G}_{24}] = -\overline{[\mathbf{G}_{42}]} = 2\hat{d}\eta\sum_{i=1}^{N_1}\sum_{j=1}^{N_1}c_{qi}c_{nj}, \quad q(n)=1,2,\ldots,N_2(M_2) \tag{8.2c}$$

$$[\mathbf{G}_{34}] = -\overline{[\mathbf{G}_{43}]} = 2\sum_{i=1}^{M_2}\sum_{j=1}^{M_2}\left(\nu_{33}-\nu_{11}-\nu_{22}-\hat{d}^2\eta\right)c_{ri}c_{nj}, \quad s(n)=1,2,\ldots,M_1(M_2) \tag{8.2d}$$

$$[\mathbf{K}_{11}] = k_{13}\kappa \sum_{i=1}^{N_1}\sum_{j=1}^{N_1} \frac{ijc_{pi}c_{kj}}{i+j-1}, \quad p,k = 1,2,\ldots,N_1 \tag{8.3a}$$

$$[\mathbf{K}_{22}] = k_{23}\kappa \sum_{i=1}^{N_2}\sum_{j=1}^{N_2} \frac{ijc_{qi}c_{lj}}{i+j-1}, \quad q,l = 1,2,\ldots,N_2 \tag{8.3b}$$

$$[\mathbf{K}_{33}] = \sum_{i=1}^{M_1}\sum_{j=1}^{M_1} \left(\frac{k_{23}\kappa}{i+j+1} + \frac{\alpha ij}{i+j-1}\right) c_{ri}c_{mj}, \quad r,m = 1,2,\ldots,M_1 \tag{8.3c}$$

$$[\mathbf{K}_{44}] = \sum_{i=1}^{M_1}\sum_{j=1}^{M_1} \left(\frac{k_{13}\kappa}{i+j+1} + \frac{ij}{i+j-1}\right) c_{si}c_{nj}, \quad s,n = 1,2,\ldots,M_2 \tag{8.3d}$$

$$[\mathbf{K}_{14}] = \overline{[\mathbf{K}_{41}]} = k_{13}\kappa \sum_{i=1}^{N_1}\sum_{j=1}^{N_1} \frac{ic_{pi}c_{nj}}{i+j} \quad p(n) = 1,2,\ldots,N_1(M_2) \tag{8.3e}$$

$$[\mathbf{K}_{23}] = \overline{[\mathbf{K}_{32}]} = k_{23}\kappa\beta \sum_{i=1}^{N_2}\sum_{j=1}^{N_2} \frac{ic_{qi}c_{mj}}{i+j} \quad q(m) = 1,2,\ldots,N_2(M_1) \tag{8.3f}$$

$$[\mathbf{C}_{11}] = \sum_{i=1}^{N_1}\sum_{j=1}^{N_1} \left(\frac{1}{i+j+1} + \eta\right) c_{pi}c_{kj}, \quad p,k = 1,2,\ldots,N_1 \tag{8.4a}$$

$$[\mathbf{C}_{11}] = \sum_{i=1}^{N_2}\sum_{j=1}^{N_2} \left(\frac{1}{i+j+1} + \eta\right) c_{qi}c_{lj}, \quad q,l = 1,2,\ldots,N_2 \tag{8.4b}$$

$$[\mathbf{C}_{33}] = -\sum_{i=1}^{M_1}\sum_{j=1}^{M_1} \left(\frac{\alpha\mu}{i+j+1} + \nu_{22} - \nu_{33} + \hat{d}^2\eta\right) c_{ri}c_{mj}, \quad r,m = 1,2,\ldots,M_1 \tag{8.4c}$$

$$[\mathbf{C}_{44}] = -\sum_{i=1}^{M_2}\sum_{j=1}^{M_2} \left(\frac{\mu}{i+j+1} + \nu_{11} - \nu_{33} + \hat{d}^2\eta\right) c_{si}c_{nj}, \quad s,n = 1,2,\ldots,M_2 \tag{8.4d}$$

$$[\mathbf{C}_{14}] = \overline{[\mathbf{C}_{41}]} = \hat{d}\eta \sum_{i=1}^{N_1}\sum_{j=1}^{N_1} c_{pi}c_{nj} \quad p(n) = 1,2,\ldots,N_1(M_2) \tag{8.4e}$$

$$[\mathbf{C}_{23}] = \overline{[\mathbf{C}_{32}]} = -\hat{d}\eta \sum_{i=1}^{N_1} \sum_{j=1}^{N_1} c_{qi} c_{mj} \quad q(m) = 1, 2, \ldots, N_2(M_1) \tag{8.4f}$$

REFERENCES

[1] K. Skiba, "Designing and FEM simulation of the helicopter rotor and hub," *IOP Conference Series: Materials Science and Engineering*, vol. 710, p. 012003, Dec. 2019.

[2] Z. Zhang, Z. Yin, T. Han, and A. C. C. Tan, "Fracture analysis of wind turbine main shaft," *Engineering Failure Analysis*, vol. 34, pp. 129–139, Dec. 2013.

[3] A. Von Moll, A. R. Behbahani, G. C. Fralick, J. D. Wrbanek, and G. W. Hunter, "A Review of Exhaust Gas Temperature Sensing Techniques for Modern Turbine Engine Controls," in *50th AIAA/ASME/SAE/ASEE Joint Propulsion Conference*, AIAA Propulsion and Energy Forum, American Institute of Aeronautics and Astronautics, July 2014.

[4] M. Ghommem and A. Abdelkefi, "Nonlinear analysis of rotating nanocrystalline silicon microbeams for microgyroscope applications," *Microsystem Technologies*, vol. 23, pp. 5931–5946, Dec. 2017.

[5] H. F. Bauer, "Vibration of a rotating uniform beam, part I: Orientation in the axis of rotation," *Journal of Sound and Vibration*, vol. 72, pp. 177–189, Sept. 1980.

[6] R. E. D. Bishop, "The Vibration of Rotating Shafts," *Journal of Mechanical Engineering Science*, vol. 1, pp. 50–65, June 1959.

[7] J. H. Dunmore, "Flexural vibrations of rotating shafts. F. M. Dimentberg. Butterworths, London, 1961. 243 pp. Diagrams. 60s.," *The Aeronautical Journal*, vol. 66, pp. 135–135, Feb. 1962.

[8] T. R. Kane, "An Addition to the Theory of Whirling," *Journal of Applied Mechanics*, vol. 28, pp. 383–386, Sept. 1961.

[9] P. Frank Pai, X. Qian, and X. Du, "Modeling and dynamic characteristics of spinning Rayleigh beams," *International Journal of Mechanical Sciences*, vol. 68, pp. 291–303, Mar. 2013.

[10] C. W. Lee, R. Katz, A. G. Ulsoy, and R. A. Scott, "Modal analysis of a distributed parameter rotating shaft," *Journal of Sound and Vibration*, vol. 122, pp. 119–130, Apr. 1988.

[11] C. W. Lee and Y. G. Jei, "Modal analysis of continuous rotor-bearing systems," *Journal of Sound and Vibration*, vol. 126, pp. 345–361, Oct. 1988.

[12] G. J. Sheu and S. M. Yang, “Dynamic analysis of a spinning Rayleigh beam,” *International Journal of Mechanical Sciences*, vol. 47, pp. 157–169, Feb. 2005.

[13] S.-T. Choi, J.-D. Wu, and Y.-T. Chou, “Dynamic Analysis of a Spinning Timoshenko Beam by the Differential Quadrature Method,” *AIAA Journal*, vol. 38, no. 5, pp. 851–856, 2000.

[14] R. P. S. Han and J. W. Z. Zu, “Modal analysis of rotating shafts: A body-fixed axis formulation approach,” *Journal of Sound and Vibration*, vol. 156, pp. 1–16, July 1992.

[15] R. Katz, C. W. Lee, A. G. Ulsoy, and R. A. Scott, “The dynamic response of a rotating shaft subject to a moving load,” *Journal of Sound and Vibration*, vol. 122, pp. 131–148, Apr. 1988.

[16] N. Popplewell and D. Chang, “Free vibrations of a stepped, spinning Timoshenko beam,” *Journal of Sound and Vibration*, vol. 203, pp. 717–722, June 1997.

[17] J. W.-Z. Zu and R. P. S. Han, “Natural Frequencies and Normal Modes of a Spinning Timoshenko Beam With General Boundary Conditions,” *Journal of Applied Mechanics*, vol. 59, pp. S197–S204, June 1992.

[18] J. W.-Z. Zu and R. P. S. Han, “Dynamic Response of a Spinning Timoshenko Beam With General Boundary Conditions and Subjected to a Moving Load,” *Journal of Applied Mechanics*, vol. 61, pp. 152–160, Mar. 1994.

[19] P. A. A. Laura, J. L. Pombo, and E. A. Susemihl, “A note on the vibrations of a clamped-free beam with a mass at the free end,” *Journal of Sound and Vibration*, vol. 37, pp. 161–168, Nov. 1974.

[20] R. E. Rossi and P. A. A. Laura, “Vibrations of a timoshenko beam clamped at one end and carrying a finite mass at the other,” *Applied Acoustics*, vol. 30, pp. 293–301, Jan. 1990.

[21] P. A. A. Laura, M. J. Maurizi, and J. L. Pombo, “A note on the dynamic analysis of an elastically restrained-free beam with a mass at the free end,” *Journal of Sound and Vibration*, vol. 41, pp. 397–405, Aug. 1975.

[22] C. A. Rossit and P. A. A. Laura, “Transverse, normal modes of vibration of a cantilever Timoshenko beam with a mass elastically mounted at the free end,” *The Journal of the Acoustical Society of America*, vol. 110, pp. 2837–2840, Dec. 2001.

[23] M. Swaminadham and A. Michael, “A note on frequencies of a beam with a heavy tip mass,” *Journal of Sound and Vibration*, vol. 66, pp. 144–147, Sept. 1979.

[24] N. G. Stephen, "Vibration of a cantilevered beam carrying a tip heavy body by Dunkerley's method," *Journal of Sound and Vibration*, vol. 70, pp. 463–465, June 1980.

[25] M. W. D. White and G. R. Heppler, "Vibration Modes and Frequencies of Timoshenko Beams With Attached Rigid Bodies," *Journal of Applied Mechanics*, vol. 62, pp. 193–199, Mar. 1995.

[26] W. Shi, Z. B. Shen, X. L. Peng, and X. F. Li, "Frequency equation and resonant frequencies of free–free Timoshenko beams with unequal end masses," *International Journal of Mechanical Sciences*, vol. 115-116, pp. 406–415, Sept. 2016.

[27] C.-C. Wu, "Free vibration analysis of a free-free Timoshenko beam carrying multiple concentrated elements with effect of rigid-body motions considered," *Journal of Sound and Vibration*, vol. 445, pp. 204–227, Apr. 2019.

[28] B. Rama Bhat and H. Wagner, "Natural frequencies of a uniform cantilever with a tip mass slender in the axial direction," *Journal of Sound and Vibration*, vol. 45, pp. 304–307, Mar. 1976.

[29] R. L. Eshleman and R. A. Eubanks, "On the Critical Speeds of a Continuous Shaft-Disk System," *Journal of Engineering for Industry*, vol. 89, pp. 645–652, Nov. 1967.

[30] T. K, A. H, and N. H, "Whirling analysis of axial-loaded multi-step Timoshenko rotor carrying concentrated masses," vol. 9, pp. 138–156, Jan. 2017.

[31] H. Afshari, K. Torabi, and A. Jafarzadeh Jazi, "Exact closed form solution for whirling analysis of Timoshenko rotors with multiple concentrated masses," *Mechanics Based Design of Structures and Machines*, vol. 50, pp. 969–992, Mar. 2022.

[32] C. Kandouci, "Whirling analysis of stepped timoshenko shaft carrying several rigid disks / Ch. Kandouci," *Journal of Mechanical Engineering (JMechE)*, vol. 19, pp. 97–124, Apr. 2022.

[33] J.-S. Wu, F.-T. Lin, and H.-J. Shaw, "Analytical Solution for Whirling Speeds and Mode Shapes of a Distributed-Mass Shaft With Arbitrary Rigid Disks," *Journal of Applied Mechanics*, vol. 81, Sept. 2013.

[34] J.-S. Wu and T.-F. Hsu, "An efficient approach for whirling speeds and mode shapes of uniform and nonuniform Timoshenko shafts mounted by arbitrary rigid disks," *Engineering Reports*, vol. 2, no. 7, p. e12183, 2020.

[35] N. Khader, "Stability of asymmetric rotors with asymmetric flexible disks," *Journal of Vibration and Control*, vol. 28, pp. 1846–1860, July 2022.

[36] J. Oh, A. Palazzolo, and L. Hu, "Stability of Non-Axisymmetric Rotor and Bearing Systems Modeled With Three-Dimensional-Solid Finite Elements," *Journal of Vibration and Acoustics*, vol. 142, Nov. 2019.

[37] L.-W. Chen and D.-M. Ku, "Dynamic Stability of a Cantilever Shaft-Disk System," *Journal of Vibration and Acoustics*, vol. 114, pp. 326–329, July 1992.

[38] C. W. Lee and J. S. Yun, "Dynamic analysis of flexible rotors subjected to torque and force," *Journal of Sound and Vibration*, vol. 192, pp. 439–452, May 1996.

[39] M. A. Aouadi and F. Lakrad, "On mathematical modelling of linear flexural vibrations of spinning Rayleigh beams," *Journal of Sound and Vibration*, vol. 430, pp. 17–35, Sept. 2018.

[40] G. Genta, "Whirling of unsymmetrical rotors: A finite element approach based on complex co-ordinates," *Journal of Sound and Vibration*, vol. 124, pp. 27–53, July 1988.

[41] F. Oncescu, A. A. Lakis, and G. Ostiguy, "Investigation of the stability and steady state response of asymmetric rotors, using finite element formulation," *Journal of Sound and Vibration*, vol. 245, pp. 303–328, Aug. 2001.

[42] D. Ardayfio and D. A. Frohrib, "Vibration of an Asymmetrically Mounted Rotor With Gyroscopic Effects," *Journal of Engineering for Industry*, vol. 98, pp. 327–331, Feb. 1976.

[43] R. Ganesan, "Effects of bearing and shaft asymmetries on the instability of rotors operating at near-critical speeds," *Mechanism and Machine Theory*, vol. 35, pp. 737–752, May 2000.

[44] R. Srinath, A. Sarkar, and A. S. Sekhar, "Instability of asymmetric shaft system," *Journal of Sound and Vibration*, vol. 362, pp. 276–291, Feb. 2016.

[45] N. Khader and M. N. Magableh, "Stability of general asymmetric-anisotropic rotors subject to harmonic follower force, 2023."

[46] Y. G. Jei and C. W. Lee, "Modal Characteristics Of Asymmetrical Rotor-bearing Systems," *Journal of Sound and Vibration*, vol. 162, pp. 209–229, Apr. 1993.

[47] W. Sun, F. Liu, Z. Ma, C. Li, and J. Zhou, "Soft mobile robots driven by foldable dielectric elastomer actuators," *Journal of Applied Physics*, vol. 120, p. 084901, Aug. 2016.

[48] G.-Y. Gu, J. Zhu, L.-M. Zhu, and X. Zhu, "A survey on dielectric elastomer actuators for soft robots," *Bioinspiration & Biomimetics*, vol. 12, p. 011003, Jan. 2017.

[49] U. Gupta, L. Qin, Y. Wang, H. Godaba, and J. Zhu, "Soft robots based on dielectric elastomer actuators: a review," *Smart Materials and Structures*, vol. 28, p. 103002, Sept. 2019.

[50] J.-H. Youn, S. M. Jeong, G. Hwang, H. Kim, K. Hyeon, J. Park, and K.-U. Kyung, "Dielectric Elastomer Actuator for Soft Robotics Applications and Challenges," *Applied Sciences*, vol. 10, p. 640, Jan. 2020.

[51] Y. Guo, L. Liu, Y. Liu, and J. Leng, "Review of Dielectric Elastomer Actuators and Their Applications in Soft Robots," *Advanced Intelligent Systems*, vol. 3, no. 10, p. 2000282, 2021.

[52] Y. Guo, Q. Qin, Z. Han, R. Plamthottam, M. Possinger, and Q. Pei, "Dielectric elastomer artificial muscle materials advancement and soft robotic applications," *SmartMat*, vol. 4, no. 4, p. e1203, 2023.

[53] X. Dou, Z. Chen, F. Ren, L. He, J. Chen, L.-J. Yin, Y. Luo, Z.-M. Dang, and J. Mao, "Dielectric Elastomer Network with Large Side Groups Achieves Large Electroactive Deformation for Soft Robotic Grippers," *Advanced Functional Materials*, vol. 34, no. 44, p. 2407049, 2024.

[54] Q. Zhang, W. Yu, J. Zhao, C. Meng, and S. Guo, "A Review of the Applications and Challenges of Dielectric Elastomer Actuators in Soft Robotics," *Machines*, vol. 13, p. 101, Feb. 2025.

[55] A. O'Halloran, F. O'Malley, and P. McHugh, "A review on dielectric elastomer actuators, technology, applications, and challenges," *Journal of Applied Physics*, vol. 104, p. 071101, Oct. 2008.

[56] R. Sarban, R. W. Jones, B. R. Mace, and E. Rustighi, "A tubular dielectric elastomer actuator: Fabrication, characterization and active vibration isolation," *Mechanical Systems and Signal Processing*, vol. 25, pp. 2879–2891, Nov. 2011.

[57] L. J. Romasanta, M. A. Lopez-Manchado, and R. Verdejo, "Increasing the performance of dielectric elastomer actuators: A review from the materials perspective," *Progress in Polymer Science*, vol. 51, pp. 188–211, Dec. 2015.

[58] H. Zhang, Y. Wang, H. Godaba, B. C. Khoo, Z. Zhang, and J. Zhu, "Harnessing Dielectric Breakdown of Dielectric Elastomer to Achieve Large Actuation," *Journal of Applied Mechanics*, vol. 84, Oct. 2017.

[59] L. Qin, J. Cao, Y. Tang, and J. Zhu, "Soft Freestanding Planar Artificial Muscle Based on Dielectric Elastomer Actuator," *Journal of Applied Mechanics*, vol. 85, Mar. 2018.

[60] I. Kajiwara, S. Kitabatake, N. Hosoya, and S. Maeda, "Design of dielectric elastomer actuators for vibration control at high frequencies," *International Journal of Mechanical Sciences*, vol. 157-158, pp. 849–857, July 2019.

[61] C. Zhang, W. Wei, H. Sun, and Q. Zhu, "Study on the properties of different dielectric elastomers applying to actuators," *Sensors and Actuators A: Physical*, vol. 329, p. 112806, Oct. 2021.

[62] C. Jean-Mistral, S. Basrour, and J.-J. Chaillout, "Modelling of dielectric polymers for energy scavenging applications," *Smart Materials and Structures*, vol. 19, p. 105006, Aug. 2010.

[63] S. J. A. Koh, C. Keplinger, T. Li, S. Bauer, and Z. Suo, "Dielectric Elastomer Generators: How Much Energy Can Be Converted?," *IEEE/ASME Transactions on Mechatronics*, vol. 16, pp. 33–41, Feb. 2011. Conference Name: IEEE/ASME Transactions on Mechatronics.

[64] J. Huang, S. Shian, Z. Suo, and D. R. Clarke, "Maximizing the Energy Density of Dielectric Elastomer Generators Using Equi-Biaxial Loading," *Advanced Functional Materials*, vol. 23, no. 40, pp. 5056–5061, 2013.

[65] R. Vertechy, G. P. Papini Rosati, and M. Fontana, "Reduced Model and Application of Inflating Circular Diaphragm Dielectric Elastomer Generators for Wave Energy Harvesting," *Journal of Vibration and Acoustics*, vol. 137, Feb. 2015.

[66] G. Moretti, S. Rosset, R. Vertechy, I. Anderson, and M. Fontana, "A Review of Dielectric Elastomer Generator Systems," *Advanced Intelligent Systems*, vol. 2, no. 10, p. 2000125, 2020.

[67] G. Moretti, M. Santos Herran, D. Forehand, M. Alves, H. Jeffrey, R. Vertechy, and M. Fontana, "Advances in the development of dielectric elastomer generators for wave energy conversion," *Renewable and Sustainable Energy Reviews*, vol. 117, p. 109430, Jan. 2020.

[68] K. V. S. Gurjar, A. S. Sadangi, A. Kumar, D. Ahmad, K. Patra, I. Collins, M. Hossain, R. M. Ajaj, and Y. Zweiri, "Dielectric Elastomer Generators: Recent Advances in Materials, Electronic Circuits, and Prototype Developments," *Advanced Energy and Sustainability Research*, vol. 6, no. 1, p. 2400221, 2025.

[69] S. C. B. Mannsfeld, B. C.-K. Tee, R. M. Stoltenberg, C. V. H.-H. Chen, S. Barman, B. V. O. Muir, A. N. Sokolov, C. Reese, and Z. Bao, "Highly sensitive flexible pressure sensors with microstructured rubber dielectric layers," *Nature Materials*, vol. 9, pp. 859–864, Oct. 2010.

[70] A. Girard, J.-P. L. Bigué, B. M. O'Brien, T. A. Gisby, I. A. Anderson, and J.-S. Plante, "Soft Two-Degree-of-Freedom Dielectric Elastomer Position Sensor Exhibiting Linear Behavior," *IEEE/ASME Transactions on Mechatronics*, vol. 20, pp. 105–114, Feb. 2015. Conference Name: IEEE/ASME Transactions on Mechatronics.

[71] D. Xu, S. Michel, T. McKay, B. O'Brien, T. Gisby, and I. Anderson, "Sensing frequency design for capacitance feedback of dielectric elastomers," *Sensors and Actuators A: Physical*, vol. 232, pp. 195–201, Aug. 2015.

[72] R. Kanno, S. Watanabe, K. Shimizu, and J. Shintake, "Self-Sensing McKibben Artificial Muscles Embedded With Dielectric Elastomer Sensor," *IEEE Robotics and Automation Letters*, vol. 6, pp. 6274–6280, Oct. 2021. Conference Name: IEEE Robotics and Automation Letters.

[73] Y. Zhu and A. Tairych, "Using a flexible substrate to enhance the sensitivity of dielectric elastomer force sensors," *Sensors and Actuators A: Physical*, vol. 332, p. 113167, Dec. 2021.

[74] L. R. G. Treloar, "The elasticity of a network of long-chain molecules—II," *Transactions of the Faraday Society*, vol. 39, pp. 241–246, Jan. 1943.

[75] M. Mooney, "A Theory of Large Elastic Deformation," *Journal of Applied Physics*, vol. 11, pp. 582–592, Sept. 1940.

[76] R. S. Rivlin and E. K. Rideal, "Large elastic deformations of isotropic materials IV. further developments of the general theory," *Philosophical Transactions of the Royal Society of London. Series A, Mathematical and Physical Sciences*, vol. 241, no. 835, pp. 379–397, 1948.

[77] E. M. Arruda and M. C. Boyce, "A three-dimensional constitutive model for the large stretch behavior of rubber elastic materials," *Journal of the Mechanics and Physics of Solids*, vol. 41, pp. 389–412, Feb. 1993.

[78] R. W. Ogden and R. Hill, "Large deformation isotropic elasticity – on the correlation of theory and experiment for incompressible rubberlike solids," *Proceedings of the Royal Society of London. A. Mathematical and Physical Sciences*, vol. 326, no. 1567, pp. 565–584, 1972.

[79] A. N. Gent, "A New Constitutive Relation for Rubber," *Rubber Chemistry and Technology*, vol. 69, pp. 59–61, Mar. 1996.

[80] O. Lopez-Pamies, "A new I1 based hyperelastic model for rubber elastic materials," *Comptes Rendus Mécanique*, vol. 338, pp. 3–11, Jan. 2010.

[81] M. Wissler and E. Mazza, “Mechanical behavior of an acrylic elastomer used in dielectric elastomer actuators,” *Sensors and Actuators A: Physical*, vol. 134, pp. 494–504, Mar. 2007.

[82] L. An, F. Wang, S. Cheng, T. Lu, and T. J. Wang, “Experimental investigation of the electromechanical phase transition in a dielectric elastomer tube,” *Smart Materials and Structures*, vol. 24, p. 035006, Feb. 2015.

[83] Y. Chen, L. Agostini, G. Moretti, M. Fontana, and R. Vertechy, “Dielectric elastomer materials for large-strain actuation and energy harvesting: a comparison between styrenic rubber, natural rubber and acrylic elastomer,” *Smart Materials and Structures*, vol. 28, p. 114001, Oct. 2019.

[84] R. Pelrine, R. Kornbluh, and G. Kofod, “High-Strain Actuator Materials Based on Dielectric Elastomers,” *Advanced Materials*, vol. 12, no. 16, pp. 1223–1225, 2000.

[85] R. W. Ogden, G. Saccomandi, and I. Sgura, “Fitting hyperelastic models to experimental data,” *Computational Mechanics*, vol. 34, pp. 484–502, Nov. 2004.

[86] C. O. Horgan and G. Saccomandi, “A description of arterial wall mechanics using limiting chain extensibility constitutive models,” *Biomechanics and Modeling in Mechanobiology*, vol. 1, pp. 251–266, Apr. 2003.

[87] M. Mehnert, M. Hossain, and P. Steinmann, “A complete thermo–electro–viscoelastic characterization of dielectric elastomers, Part I: Experimental investigations,” *Journal of the Mechanics and Physics of Solids*, vol. 157, p. 104603, Dec. 2021.

[88] M. Mehnert, M. Hossain, and P. Steinmann, “A complete thermo-electro-viscoelastic characterization of dielectric elastomers, Part II: Continuum modeling approach,” *Journal of the Mechanics and Physics of Solids*, vol. 157, p. 104625, Dec. 2021.

[89] S. K. Behera, D. Kumar, and S. Sarangi, “Modeling of electro–viscoelastic dielectric elastomer: A continuum mechanics approach,” *European Journal of Mechanics - A/Solids*, vol. 90, p. 104369, Nov. 2021.

[90] P. Ma, K. Chen, and G. Kang, “Electro-mechanically coupled pure-shear cyclic deformation of dielectric elastomers at different temperatures: Experiments and constitutive model,” *European Journal of Mechanics - A/Solids*, vol. 112, p. 105637, July 2025.

[91] R. Pelrine, R. Kornbluh, Q. Pei, and J. Joseph, “High-Speed Electrically Actuated Elastomers with Strain Greater Than 100%,” *Science*, vol. 287, pp. 836–839, Feb. 2000.

[92] M. Wissler and E. Mazza, “Electromechanical coupling in dielectric elastomer actuators,” *Sensors and Actuators A: Physical*, vol. 138, pp. 384–393, Aug. 2007.

[93] M. Wissler and E. Mazza, “Modeling of a pre-strained circular actuator made of dielectric elastomers,” *Sensors and Actuators A: Physical*, vol. 120, pp. 184–192, Apr. 2005.

[94] H. Liang, B. Du, Y. Zhao, S. Li, X. Zhang, and X. Chen, “Highly efficient inverse lumped modeling for the pre-strained circular dielectric elastomer,” *International Journal of Mechanical Sciences*, vol. 279, p. 109524, Oct. 2024.

[95] J. W. Fox and N. C. Goulbourne, “Electric field-induced surface transformations and experimental dynamic characteristics of dielectric elastomer membranes,” *Journal of the Mechanics and Physics of Solids*, vol. 57, pp. 1417–1435, Aug. 2009.

[96] J. Zhu, S. Cai, and Z. Suo, “Nonlinear oscillation of a dielectric elastomer balloon,” *Polymer International*, vol. 59, no. 3, pp. 378–383, 2010.

[97] H. Yong, X. He, and Y. Zhou, “Dynamics of a thick-walled dielectric elastomer spherical shell,” *International Journal of Engineering Science*, vol. 49, pp. 792–800, Aug. 2011.

[98] F. Liu and J. Zhou, “Shooting and Arc-Length Continuation Method for Periodic Solution and Bifurcation of Nonlinear Oscillation of Viscoelastic Dielectric Elastomers,” *Journal of Applied Mechanics*, vol. 85, Nov. 2017.

[99] J. Sheng, H. Chen, B. Li, and Y. Wang, “Nonlinear dynamic characteristics of a dielectric elastomer membrane undergoing in-plane deformation,” *Smart Materials and Structures*, vol. 23, p. 045010, Feb. 2014.

[100] J. Zhang, J. Zhao, H. Chen, and D. Li, “Dynamic analyses of viscoelastic dielectric elastomers incorporating viscous damping effect,” *Smart Materials and Structures*, vol. 26, p. 015010, Dec. 2016.

[101] N. Arora, P. Kumar, and M. M. Joglekar, “A Modulated Voltage Waveform for Enhancing the Travel Range of Dielectric Elastomer Actuators,” *Journal of Applied Mechanics*, vol. 85, Aug. 2018.

[102] F. Wang, T. Lu, and T. J. Wang, “Nonlinear vibration of dielectric elastomer incorporating strain stiffening,” *International Journal of Solids and Structures*, vol. 87, pp. 70–80, June 2016.

[103] C. G. Cooley and R. L. Lowe, “In-plane nonlinear vibration of circular dielectric elastomer membranes with extreme stretchability,” *European Journal of Mechanics - A/Solids*, vol. 96, p. 104660, Nov. 2022.

[104] C. G. Cooley and R. L. Lowe, "Unusual nonlinear frequency response in circular dielectric elastomer membranes excited by fluctuating through-thickness voltages," *Mechanics Research Communications*, vol. 124, p. 103928, Sept. 2022.

[105] A. Alibakhshi and H. Heidari, "Analytical approximation solutions of a dielectric elastomer balloon using the multiple scales method," *European Journal of Mechanics - A/Solids*, vol. 74, pp. 485–496, Mar. 2019.

[106] D. Tang, C. W. Lim, L. Hong, J. Jiang, and S. K. Lai, "Dynamic Response and Stability Analysis with Newton Harmonic Balance Method for Nonlinear Oscillating Dielectric Elastomer Balloons," *International Journal of Structural Stability and Dynamics*, vol. 18, p. 1850152, Dec. 2018.

[107] C. G. Cooley and R. L. Lowe, "Nonlinear vibration of dielectric elastomer membranes with axial inertia effects," *International Journal of Mechanical Sciences*, vol. 248, p. 108205, June 2023.

[108] B.-X. Xu, R. Mueller, A. Theis, M. Klassen, and D. Gross, "Dynamic analysis of dielectric elastomer actuators," *Applied Physics Letters*, vol. 100, p. 112903, Mar. 2012.

[109] M. M. Joglekar, "An Energy-Based Approach to Extract the Dynamic Instability Parameters of Dielectric Elastomer Actuators," *Journal of Applied Mechanics*, vol. 81, July 2014.

[110] A. K. Sharma, S. Bajpayee, D. M. Joglekar, and M. M. Joglekar, "Dynamic instability of dielectric elastomer actuators subjected to unequal biaxial prestress," *Smart Materials and Structures*, vol. 26, p. 115019, Oct. 2017. Publisher: IOP Publishing.

[111] Z. Wang, B. He, Y. Zhou, R. Shen, and G. Li, "Effects of pre-stretch on the oscillation and stability of dielectric elastomers," *International Journal of Mechanical Sciences*, vol. 185, p. 105879, Nov. 2020.

[112] Y. Kagawa, N. Wakatsuki, T. Tsuchiya, and Y. Terada, "A tubular piezoelectric vibrator gyroscope," *IEEE Sensors Journal*, vol. 6, pp. 325–330, Apr. 2006. Conference Name: IEEE Sensors Journal.

[113] M. Esmaeili, N. Jalili, and M. Durali, "Dynamic modeling and performance evaluation of a vibrating beam microgyroscope under general support motion," *Journal of Sound and Vibration*, vol. 301, pp. 146–164, Mar. 2007.

[114] V. Bhadbhade, N. Jalili, and S. Nima Mahmoodi, "A novel piezoelectrically actuated flexural/torsional vibrating beam gyroscope," *Journal of Sound and Vibration*, vol. 311, pp. 1305–1324, Apr. 2008.

[115] M. Mojahedi, M. T. Ahmadian, and K. Firoozbakhsh, “The influence of the intermolecular surface forces on the static deflection and pull-in instability of the micro/nano cantilever gyroscopes,” *Composites Part B: Engineering*, vol. 56, pp. 336–343, Jan. 2014.

[116] A. H. Nayfeh, E. M. Abdel-Rahman, and M. Ghommem, “A novel differential frequency micro-gyroscope,” *Journal of Vibration and Control*, vol. 21, pp. 872–882, Apr. 2015.

[117] S. A. M. Lajimi, G. R. Heppler, and E. M. Abdel-Rahman, “A mechanical–thermal noise analysis of a nonlinear microgyroscope,” *Mechanical Systems and Signal Processing*, vol. 83, pp. 163–175, Jan. 2017.

[118] S. A. M. Lajimi, G. R. Heppler, and E. M. Abdel-Rahman, “Primary resonance of a beam-rigid body microgyroscope,” *International Journal of Non-Linear Mechanics*, vol. 77, pp. 364–375, Dec. 2015.

[119] W. Li, X.-D. Yang, W. Zhang, Y. Ren, and T. Yang, “Free Vibrations and Energy Transfer Analysis of the Vibrating Piezoelectric Gyroscope Based on the Linear and Nonlinear Decoupling Methods,” *Journal of Vibration and Acoustics*, vol. 141, May 2019.

[120] M. Rasekh and S. E. Khadem, “Design and performance analysis of a nanogyroscope based on electrostatic actuation and capacitive sensing,” *Journal of Sound and Vibration*, vol. 332, pp. 6155–6168, Nov. 2013.

[121] M. H. Ghayesh, H. Farokhi, and G. Alici, “Size-dependent performance of microgyroscopes,” *International Journal of Engineering Science*, vol. 100, pp. 99–111, Mar. 2016.

[122] H. M. Ouakad, “Nonlinear structural behavior of a size-dependent MEMS gyroscope assuming a non-trivial shaped proof mass,” *Microsystem Technologies*, vol. 26, pp. 573–582, Feb. 2020.

[123] K. Larkin, M. Ghommem, and A. Abdelkefi, “Significance of size dependent and material structure coupling on the characteristics and performance of nanocrystalline micro/nano gyroscopes,” *Physica E: Low-dimensional Systems and Nanostructures*, vol. 99, pp. 169–181, May 2018.

[124] M. Serrano, K. Larkin, M. Ghommem, S. Tretiak, and A. Abdelkefi, “Broadband piezoelectric energy harvesting microgyroscopes: Design and nonlinear analysis,” *European Journal of Mechanics - A/Solids*, vol. 98, p. 104888, Mar. 2023.

[125] W. Li, Y.-N. Bai, J.-H. Yang, Y. Sun, and H.-Y. Chen, "Intermolecular forces and surface stress residual effects on the size-dependent performance analysis of nanocrystalline micro/nano gyroscopes," *European Journal of Mechanics - A/Solids*, vol. 105, p. 105236, May 2024.

[126] J. R. Banerjee, "Development of an exact dynamic stiffness matrix for free vibration analysis of a twisted Timoshenko beam," *Journal of Sound and Vibration*, vol. 270, pp. 379–401, Feb. 2004.

[127] Y.-G. Jei and C.-W. Lee, "Does Curve Veering Occur in the Eigenvalue Problem of Rotors?," *Journal of Vibration and Acoustics*, vol. 114, pp. 32–36, Jan. 1992.

[128] W. H. Liu and D. S. Liu, "Natural frequencies of a restrained Timoshenko beam with a tip body at its free end," *Journal of Sound and Vibration*, vol. 128, pp. 167–173, Jan. 1989.

[129] P. A. A. Laura and R. H. Gutierrez, "Vibrations of an elastically restrained cantilever beam of varying cross section with tip mass of finite length," *Journal of Sound and Vibration*, vol. 108, pp. 123–131, July 1986.

[130] C. W. S. To, "Vibration of a cantilever beam with a base excitation and tip mass," *Journal of Sound and Vibration*, vol. 83, pp. 445–460, Aug. 1982.

[131] K. T. Andrews and M. Shillor, "Vibrations of a beam with a damping tip body," *Mathematical and Computer Modelling*, vol. 35, pp. 1033–1042, May 2002.

[132] J. C. Bruch and T. P. Mitchell, "Vibrations of a mass-loaded clamped-free Timoshenko beam," *Journal of Sound and Vibration*, vol. 114, pp. 341–345, Apr. 1987.

[133] H. D. Nelson, "A Finite Rotating Shaft Element Using Timoshenko Beam Theory," *Journal of Mechanical Design*, vol. 102, pp. 793–803, Oct. 1980.

[134] K. E. Rouch and J. S. Kao, "A tapered beam finite element for rotor dynamics analysis," *Journal of Sound and Vibration*, vol. 66, pp. 119–140, Sept. 1979.

[135] L. M. Greenhill, W. B. Bickford, and H. D. Nelson, "A Conical Beam Finite Element for Rotor Dynamics Analysis," *Journal of Vibration, Acoustics, Stress, and Reliability in Design*, vol. 107, pp. 421–430, Oct. 1985.

[136] S. L. Edney, C. H. J. Fox, and E. J. Williams, "Tapered Timoshenko finite elements for rotor dynamics analysis," *Journal of Sound and Vibration*, vol. 137, pp. 463–481, Mar. 1990.

[137] O. S. Jun and J. O. Kim, "Free bending vibration of a multi-step rotor," *Journal of Sound and Vibration*, vol. 224, pp. 625–642, July 1999.

[138] S. D. Yu and W. L. Cleghorn, "Free Vibration of a Spinning Stepped Timoshenko Beam," *Journal of Applied Mechanics*, vol. 67, pp. 839–841, Apr. 2000.

[139] A. Mereles and K. L. Cavalca, "Modeling of Multi-stepped Rotor-bearing Systems by the Continuous Segment Method," *Applied Mathematical Modelling*, vol. 96, pp. 402–430, Aug. 2021.

[140] S. H. Mirtalaie and M. A. Hajabasi, "A New Methodology for Modeling and Free Vibrations Analysis of Rotating Shaft Based on the Timoshenko Beam Theory," *Journal of Vibration and Acoustics*, vol. 138, Jan. 2016.

[141] M. Jahangiri, M. Asghari, and E. Bagheri, "Torsional vibration induced by gyroscopic effect in the modified couple stress based micro-rotors," *European Journal of Mechanics - A/Solids*, vol. 81, p. 103907, May 2020.

[142] M. R. M. C. Da Silva, "Non-linear flexural-flexural-torsional-extensional dynamics of beams—II. Response analysis," *International Journal of Solids and Structures*, vol. 24, pp. 1235–1242, Jan. 1988.

[143] M. R. M. C. Da Silva, "Non-linear flexural-flexural-torsional-extensional dynamics of beams—I. Formulation," *International Journal of Solids and Structures*, vol. 24, pp. 1225–1234, Jan. 1988.

[144] J. R. Hutchinson, "Shear Coefficients for Timoshenko Beam Theory," *Journal of Applied Mechanics*, vol. 68, pp. 87–92, Aug. 2000.

[145] J. J. Jensen, "On the shear coefficient in Timoshenko's beam theory," *Journal of Sound and Vibration*, vol. 87, pp. 621–635, Apr. 1983.

[146] D. Ramkrishna and N. R. Amundson, "On Vibration Problems With Discretely Distributed Loads—A Rigorous Formalism," *ASME Journal of Applied Mechanics*, vol. 41, pp. 1106–1112, Dec. 1974.

[147] B. Friedman, *Principles and Techniques of Applied Mathematics*. Jan. 1990.

[148] C. D. Mote, Jr., "Moving-load stability of a circular plate on a floating central collar," *The Journal of the Acoustical Society of America*, vol. 61, pp. 439–447, Feb. 1977.

[149] R. G. Parker, "Analytical Vibration of Spinning, Elastic Disk-Spindle Systems," *ASME Journal of Applied Mechanics*, vol. 66, pp. 218–224, Mar. 1999.

[150] R. G. Parker and P. J. Sathe, "Free Vibration and Stability of a Spinning Disk-Spindle System," *Journal of Vibration and Acoustics*, vol. 121, pp. 391–396, July 1999.

[151] R. S. Beikmann, N. C. Perkins, and A. G. Ulsoy, "Nonlinear Coupled Vibration Response of Serpentine Belt Drive Systems," *Journal of Vibration and Acoustics*, vol. 118, pp. 567–574, Oct. 1996.

[152] L. Kong and R. G. Parker, "Coupled Belt-Pulley Vibration in Serpentine Drives With Belt Bending Stiffness," *Journal of Applied Mechanics*, vol. 71, pp. 109–119, Mar. 2004.

[153] X. Wu and R. G. Parker, "Modal Properties of Planetary Gears With an Elastic Continuum Ring Gear," *Journal of Applied Mechanics*, vol. 75, May 2008.

[154] C. Wang and R. G. Parker, "Modal properties and parametrically excited vibrations of spinning epicyclic/planetary gears with a deformable ring," *Journal of Sound and Vibration*, vol. 494, p. 115828, Mar. 2021.

[155] E. K. Ervin and J. A. Wickert, "Repetitive impact response of a beam structure subjected to harmonic base excitation," *Journal of Sound and Vibration*, vol. 307, pp. 2–19, Oct. 2007.

[156] C. G. Cooley and R. G. Parker, "Vibration of Spinning Cantilever Beams With an Attached Rigid Body Undergoing Bending-Bending-Torsional-Axial Motions," *Journal of Applied Mechanics*, vol. 81, Dec. 2013.

[157] L. Meirovitch, "A New Method of Solution of the Eigenvalue Problem for Gyroscopic Systems," *AIAA Journal*, vol. 12, no. 10, pp. 1337–1342, 1974.

[158] G. M. T. D'Eleuterio and P. C. Hughes, "Dynamics of Gyroelastic Continua," *Journal of Applied Mechanics*, vol. 51, pp. 415–422, June 1984.

[159] J. A. Wickert and C. D. Mote, Jr., "Classical Vibration Analysis of Axially Moving Continua," *Journal of Applied Mechanics*, vol. 57, pp. 738–744, Sept. 1990.

[160] A. W. Leissa, "On a curve veering aberration," *Zeitschrift für angewandte Mathematik und Physik ZAMP*, vol. 25, pp. 99–111, Jan. 1974.

[161] J. R. Kuttler and V. G. Sigillito, "On curve veering," *Journal of Sound and Vibration*, vol. 75, pp. 585–588, Apr. 1981.

[162] N. C. Perkins and C. D. Mote, "Comments on curve veering in eigenvalue problems," *Journal of Sound and Vibration*, vol. 106, pp. 451–463, May 1986.

[163] C. G. Cooley and R. G. Parker, "Vibration Properties of High-Speed Planetary Gears With Gyroscopic Effects," *Journal of Vibration and Acoustics*, vol. 134, Oct. 2012.

[164] C. Shi and R. G. Parker, “Modal structure of centrifugal pendulum vibration absorber systems with multiple cyclically symmetric groups of absorbers,” *Journal of Sound and Vibration*, vol. 332, pp. 4339–4353, Sept. 2013.

[165] C. Shi and R. G. Parker, “Vibration mode structure and simplified modelling of cyclically symmetric or rotationally periodic systems,” *Proceedings of the Royal Society A: Mathematical, Physical and Engineering Sciences*, vol. 471, p. 20140672, Jan. 2015.

[166] B. Dong and R. G. Parker, “Modal properties of cyclically symmetric systems with central components vibrating as three-dimensional rigid bodies,” *Journal of Sound and Vibration*, vol. 435, pp. 350–371, Nov. 2018.

[167] S. A. Tobias and R. N. Arnold, “The Influence of Dynamical Imperfection on the Vibration of Rotating Disks,” *Proceedings of the Institution of Mechanical Engineers*, vol. 171, pp. 669–690, June 1957.

[168] C. D. Mote, “Stability of circular plates subjected to moving loads,” *Journal of the Franklin Institute*, vol. 290, pp. 329–344, Oct. 1970.

[169] J.-S. Chen and D. B. Bogy, “Effects of Load Parameters on the Natural Frequencies and Stability of a Flexible Spinning Disk With a Stationary Load System,” *Journal of Applied Mechanics*, vol. 59, pp. S230–S235, June 1992.

[170] G. F. Carrier, “On the Vibrations of the Rotating Ring,” *Quarterly of Applied Mathematics*, vol. 3, no. 3, pp. 235–245, 1945.

[171] C. W. Bert and T. L. C. Chen, “On vibration of a thick flexible ring rotating at high speed,” *Journal of Sound and Vibration*, vol. 61, pp. 517–530, Dec. 1978.

[172] M. Endo, K. Hatamura, M. Sakata, and O. Taniguchi, “Flexural vibration of a thin rotating ring,” *Journal of Sound and Vibration*, vol. 92, pp. 261–272, Jan. 1984.

[173] W. B. Bickford and E. S. Reddy, “On the in-plane vibrations of rotating rings,” *Journal of Sound and Vibration*, vol. 101, pp. 13–22, July 1985.

[174] S. C. Huang and W. Soedel, “Effects of coriolis acceleration on the free and forced in-plane vibrations of rotating rings on elastic foundation,” *Journal of Sound and Vibration*, vol. 115, pp. 253–274, June 1987.

[175] C. G. Cooley and R. G. Parker, “Vibration of high-speed rotating rings coupled to space-fixed stiffnesses,” *Journal of Sound and Vibration*, vol. 333, pp. 2631–2648, June 2014.

[176] C. G. Cooley and R. G. Parker, “Unusual gyroscopic system eigenvalue behavior in high-speed planetary gears,” *Journal of Sound and Vibration*, vol. 332, pp. 1820–1828, Apr. 2013.

[177] M. P. Païdoussis and N. T. Issid, “Dynamic stability of pipes conveying fluid,” *Journal of Sound and Vibration*, vol. 33, pp. 267–294, Apr. 1974.

[178] D. J. Dawe, “A finite element for the vibration analysis of Timoshenko beams,” *Journal of Sound and Vibration*, vol. 60, pp. 11–20, Sept. 1978.

[179] A. Moallemi-Oreh and M. Karkon, “Finite Element Formulation for Stability and Free Vibration Analysis of Timoshenko Beam,” *Advances in Acoustics and Vibration*, vol. 2013, no. 1, p. 841215, 2013.

[180] D. L. Thomas, J. M. Wilson, and R. R. Wilson, “Timoshenko beam finite elements,” *Journal of Sound and Vibration*, vol. 31, pp. 315–330, Dec. 1973.

[181] J. Thomas and B. A. H. Abbas, “Finite element model for dynamic analysis of Timoshenko beam,” *Journal of Sound and Vibration*, vol. 41, pp. 291–299, Aug. 1975.

[182] J. Chung and H. Yoo, “Dynamic analysis of flexible rotors subjected to torque and force,” *Journal of Sound and Vibration*, vol. 249, pp. 147–164, Jan. 2002.

[183] S. Hoa, “Vibration of a rotating beam with tip mass,” *Journal of Sound and Vibration*, vol. 67, pp. 369–381, Dec. 1979.

[184] S. Rao and R. Gupta, “Finite element vibration analysis of rotating Timoshenko beams,” *Journal of Sound and Vibration*, vol. 242, pp. 103–124, Apr. 2001.

[185] D. Ahiwale, H. Madake, N. Phadtare, A. Jarande, and D. Jambhale, “Modal analysis of cracked cantilever beam using ANSYS software,” *Materials Today: Proceedings*, vol. 56, pp. 165–170, 2022.

[186] R. Fotouhi, “Dynamic analysis of very flexible beams,” *Journal of Sound and Vibration*, vol. 305, pp. 521–533, Aug. 2007.

[187] H. Karagülle, L. Malgaca, and H. F. Öktem, “Analysis of active vibration control in smart structures by ANSYS,” *Smart Materials and Structures*, vol. 13, pp. 661–667, Aug. 2004.

[188] O. H. Yeoh, “Some Forms of the Strain Energy Function for Rubber,” vol. 66, pp. 754–771, 1993.

[189] A. N. Gent and A. G. Thomas, “Forms for the stored (strain) energy function for vulcanized rubber,” *Journal of Polymer Science*, vol. 28, no. 118, pp. 625–628, 1958.

[190] E. Pucci and G. Saccomandi, “A Note on the Gent Model for Rubber-Like Materials,” vol. 75, pp. 839–852, Nov. 2002.

[191] L. Zhou, S. Wang, L. Li, and Y. Fu, “An evaluation of the Gent and Gent-Gent material models using inflation of a plane membrane,” *International Journal of Mechanical Sciences*, vol. 146-147, pp. 39–48, Oct. 2018.

[192] M. Reed and B. Simon, *Methods of Modern Mathematical Physics: Functional analysis*. 1972.